SEARCH FOR ASTROPHYSICAL TAU NEUTRINOS IN THREE YEARS OF ICECUBE DATA

by

DONGLIAN XU

DAWN R. WILLIAMS, COMMITTEE CHAIR
PATRICK A. TOALE
ANDREAS PIEPKE
NOBUCHIKA OKADA
YUPING BAO

A DISSERTATION

Submitted in partial fullfillment of the requirements
for the degree of Doctor of Philosophy
in the Department of Physics and Astronomy
in the Graduate School of
The University of Alabama

TUSCALOOSA, ALABAMA

2015

ABSTRACT

High-energy cosmic neutrinos are expected to be produced in extremely energetic astrophysical sources such as active galactic nuclei (AGNs) and gamma ray bursts (GRBs). The IceCube Neutrino Observatory has recently detected a diffuse astrophysical neutrino flux at 5.7σ significance. One of the outstanding questions regarding astrophysical neutrinos is their flavor composition. Most standard oscillation scenarios predict tau neutrinos (ν_τ) in the astrophysical flux, which have a negligible background from cosmic ray induced atmospheric neutrinos. This work reports a search for high-energy astrophysical ν_τ with the IceCube neutrino observatory. This analysis has devised a new method to search for astrophysical ν_τ in the IceCube waveforms, and it is the first ν_τ analysis in IceCube that is more sensitive to a ν_τ flux than other neutrino flavors. A total of three years of data was used, yielding a sensitivity of 5.1×10^{-8} GeV cm^{-2} s^{-1} sr^{-1} near the PeV region assuming a flux limit of $\mathrm{E}^2\Phi_\nu < 1.0 \times 10^{-8}$ GeV cm^{-2} s^{-1} sr^{-1} per neutrino flavor. Zero events were found. Differential upper limits for astrophysical ν_τ are derived in the $O(100)$ TeV to $O(10)$ PeV regime based on the zero findings.

DEDICATION

To Mom, Dad, and my fleeting Youth.

ACKNOWLEDGMENTS

This work is supported by the National Science Foundation under Grant No. 1307108.

I owe the deepest gratitude to my supervisor, Prof. Dawn Williams. Joining the University of Alabama at about the same time, we have been working on the IceCube project for more than 5 years. Prof. Williams was a constant role model by being an excellent and fully dedicated scientist. She is generous, kind, and always available for me and her other students. Her thorough knowledge of the IceCube detector and great ability to grasp information, has helped tremendously during my research and dissertation writing. Over the years, her sense of optimism and bravery has been nothing but inspiring. In particular, her willingness to sacrifice weekends and holidays to help with my dissertation writing/editing was admirable. I feel honored to have Prof. Williams as my PhD supervisor and could not have asked more of her.

I am also grateful to Prof. Patrick Toale, who was a great help during my PhD study. In addition to serving on both my preliminary exam and dissertation defense committees, Prof. Toale has provided invaluable insights and guidelines for my research. His deep understanding of fundamental concepts, along with extraordinary capability to explain them, have been a substantial resource. If my focus ever weakened when struggling with obstacles, he was quick with encouragement to motivate me through it.

My committee has been great and they deserve much appreciation. Many thanks go to Prof. Williams, Prof. Toale, Prof. Andreas Piepke, Prof. Nobuchika Okada and Prof. Yuping Bao. Their willingness to be on my committee without hesitance was encouraging. Their time and effort spent proofreading the dissertation with care, as well as raising challenging questions that help me better understand my topic, are deeply appreciated.

Many colleagues from the IceCube collaboration have been great helpers and supporters to me. I would like to thank my analysis reviewers: Prof. Shigeru Yoshida at Chiba University in Japan and Prof. Lutz Köpke at University of Mainz in Germany. They have carefully scrutinized

my analysis methods and provided invaluable insights to further strengthen my analysis. It was encouraging that Prof. Albrecht Karle at the University of Wisconsin-Madison and Prof. Doug Cowen at the Pennsylvania State University were expressing their interest and support in my work along the way. They also agreed later to be references for me. I owe my gratitude to them. Many other colleagues and friends from the IceCube collaboration benefited me both in research and in life: Dr. Jakob van Santen, Prof. Claudio Kopper, Prof. Joanna Kiryluk, Prof. Per Olof Hulth, Dr. Klas Hultqvist, Dr. Aya Ishihara, Dr. Chang Hyon Ha, Prof. Carlos Pérez de los Heros, Prof. Ignacio Taboada, Dr. Dmitry Chirkin, Dr. Eike Middell, Dr. Kai Schatto, Dr. Kirill Filimonov, Dr. Jan Lünemann, Volker Baum, Klaus Wiebe, Gösta Kroll, Rickard Ström, Henric Taavola, Tania Wood, Marcel Zoll, Hans Niederhausen, Dr. Arne Schönwald, Dr. Kurt Woschnagg, Prof. Darren Grant, Prof. Tyce DeYoung, Prof. Jason Koskinen, Michael Larson, James Pepper, Dr. Pavel Zarzhitsky, Dr. Tomasz Palczewski, Dr. Mike Richman, Dr. Laura Gladstone, Dr. Christopher Weaver, Dr. Nathan Whitehorn, Dr. David Boersma, Dr. Dipo Fadiran, Dr. Juan Pablo Yañez, Prof. Naoko Kurahashi Neilson, Daniel Bindig, Anna Obertacke, Anatoli Fedynitch, ... and many others. I am very grateful to them for making my PhD process both productive and enjoyable. I must also thank the Queen of IceCube - Kim Kreiger for all of the fantastic collaboration meetings and events she and her team have organized.

My friends beyond the IceCube collaboration have been nothing but great supporters over the years. Sean Marrone and his family are home to me in the United States. I thank the Marrone family for their love and great confidence in me. I have enjoyed many helpful conversations with, and benefited much from, my fellow students and friends: Dr. Zina Zhu, Dr. Nianhui Song, Dr. Yunzhe Feng, Ke Fang, Dr. Cheng Cheng, Dr. Dazhi Xu, Dr. Ru Zhu, Michael Larson, James Pepper, Dr. Aparajita Sengupta, Dr .Yuanyuan Su, Dr. Yujing Sun, Dr. Jian Yu, Lei Lv, Zhongliang Ouyang, Shaoqi Hou, Chengming Jiang, Joshua Jones, Broxton Miles, Andrew Buccilli, Nathan Papapietro and Timmy Brockett. Many of my long-time friends since childhood have encouraged me to pursue my dreams. Among them: Xiaodan Tang, Mengmei Huang, Meiyan Chen, Qin Feng, Caifu Luo and Yan Lin. I am deeply grateful for their company and nonstop support. Their warm messages have helped me through many sleepless nights. During my dissertation-writing phase,

three newly met friends, Fuyan Zhang, Yue Sun and Shuzheng Wang have kindly accommodated me in their house and prepared delicious food for me daily. I owe great gratitude to their hospitality and good will.

Finally, I would like to thank my family for their unconditional love and unfading support. I could not be more thankful for the space and freedom my parents have granted me. When told that I wanted to study astrophysics, Mom and Dad cheered for me even though Dad thought that finance might be a better idea. I only hope that I can make them proud someday.

Last but not least, to all the amazing people that I have met and am about to meet, I salute you. Live long and prosper.

CONTENTS

LIST OF TABLES

LIST OF FIGURES

Chapter 1

Introduction

In 2013, the IceCube Neutrino Observatory reported the observation of a high-energy diffuse astrophysical neutrino flux [1]. This detection has marked the dawn of high-energy neutrino astronomy. An outstanding question regarding the diffuse flux is the neutrino flavor composition. The astrophysical neutrinos observed by IceCube are consistent with equal fractions of all neutrino flavors at Earth's surface: $\nu_e : \nu_\mu : \nu_\tau = 1 : 1 : 1$.

The identification of tau neutrinos in the IceCube signal is of particular interest with respect to the flavor composition. Tau neutrinos (ν_τ) are not expected to be produced in significant amounts at the astrophysical sources, therefore detection of high-energy ν_τ at Earth will shed light on flavor change in astrophysical neutrinos, because tau neutrinos are only expected in the flux as a result of flavor change. At energies lower than 1 PeV, ν_τ in IceCube are indistinguishable from the ν_e charged current (CC) events and neutral current (NC) events of all flavors. However, at energies above 1 PeV, the tau neutrino might be detected by the distinctive "double bang" signature [2]. The double bang is a double deposition of energy in IceCube: the first from the high-energy ν_τ CC interaction, and the second from the τ lepton decaying electronically or hadronically. Note that the τ lepton has mass of m_τ = 1776.82 MeV/c^2 and a mean lifetime of $t = 2.91 \times 10^{-13}$ s. Hence, ct = 87.11 μm and the τ decay length can be calculated as $l_\tau = \gamma ct = \frac{E}{m_\tau c^2} \cdot ct$. Therefore, a 1 PeV τ will travel 50 m on average before decaying, which is approximately the length necessary for the two bangs to be resolved by IceCube. At energies between $\sim$ 100 TeV and 1 PeV, the two depositions

of energy might manifest themselves as a double pulse in individual IceCube sensors. At least $\sim$ 10 m in τ length is required to resolve the double pulse signature, which lowers ν_τ CC detection energy threshold to $\sim$ 200 TeV. In my dissertation, I describe a search for tau neutrinos in IceCube using the double pulse signature. This is the first dedicated neutrino search which is more sensitive to tau neutrinos than to any other flavor.

This dissertation begins with an overview of neutrino physics in Chapter 2, which includes neutrino interactions in the Standard Model, neutrino oscillation phenomena and neutrino sources. In Chapter 3, I discuss neutrino astronomy. High-energy neutrinos are expected to be produced at acceleration sites for high-energy cosmic rays. Chapter 3 will begin with the discovery, energy spectra and acceleration mechanism for cosmic rays. Production of astrophysical neutrinos will be covered following the discussion of cosmic rays, and then I discuss the major background to the observation of astrophysical neutrinos: the cosmic ray induced atmospheric neutrinos. Finally, I summarize existing experiments to search for astrophysical neutrinos. Chapter 4 introduces the world's largest astrophysical neutrino telescope to date: the IceCube Neutrino Observatory. The overall detector design, data acquisition and detector calibration will be covered. Chapter 5 discusses the major physics processes in IceCube, which encompass the neutrino-nucleon deep inelastic scattering (DIS) process, the neutrino-induced secondary particle interactions in ice and their corresponding signatures in IceCube. I describe the simulation of high-energy neutrinos, cosmic ray induced atmospheric neutrinos and muons; the propagation of neutrinos, charged particles and photons through the ice and response from the detector. I then describe the relevant event reconstruction algorithms. In the last section of Chapter 5, I summarize recent results from IceCube which motivate this work. In Chapter 6, I will describe my search for astrophysical tau neutrinos via identification of the double pulse signature in IceCube. Firstly, I introduce the double pulse waveform characteristics and a python based algorithm to quickly identify the double pulse signature. Then I describe the double pulse event selection, signal and background event rate estimation and cut efficiency. Lastly, I show the sensitivity of this analysis to a ν_τ flux. In Chapter 7, I will discuss the results from this analysis upon unblinding which found zero events, based on which

generic differential upper limits on astrophysical ν_τ fluxes are derived. Major sources of systematic error associated with this analysis are also summarized in Chapter 7. Chapter 8 will conclude this work and discuss the outlook for future astrophysical ν_τ searches in IceCube.

Chapter 2

Neutrinos: An Overview

This chapter begins with a brief introduction to the Standard Model of particle physics, then the history of neutrino physics is summarized. In Section 3, the neutrino interaction through the weak force within the Standard Model is briefly discussed, followed by the neutrino oscillation and flavor changing phenomena in vacuum and matter in Section 4. Finally, the various sources of neutrinos are summarized in Section 5.

2.1 The Standard Model

Over the past century, physicists have made many exciting discoveries leading to the insight of the fundamental structure of matter: that is, everything in the universe is made from a few basic building blocks - the elementary particles. The Standard Model (SM) was developed in the early 1960s to describe three out of the four fundamental interactions of elementary particles. It is a set of theories that encapsulate the physical constants and fundamental interaction laws of those elementary particles which can be categorized into matter particles and force carriers [3, 4]. The three interactions include electromagnetic, weak and strong interactions. Gravitational interaction is not treated in the Standard Model.

The matter particles (fermions) consist of two sub-categories of particles, the quarks and leptons. Quarks have fractional charges, and do not exist individually in nature. Quarks always come

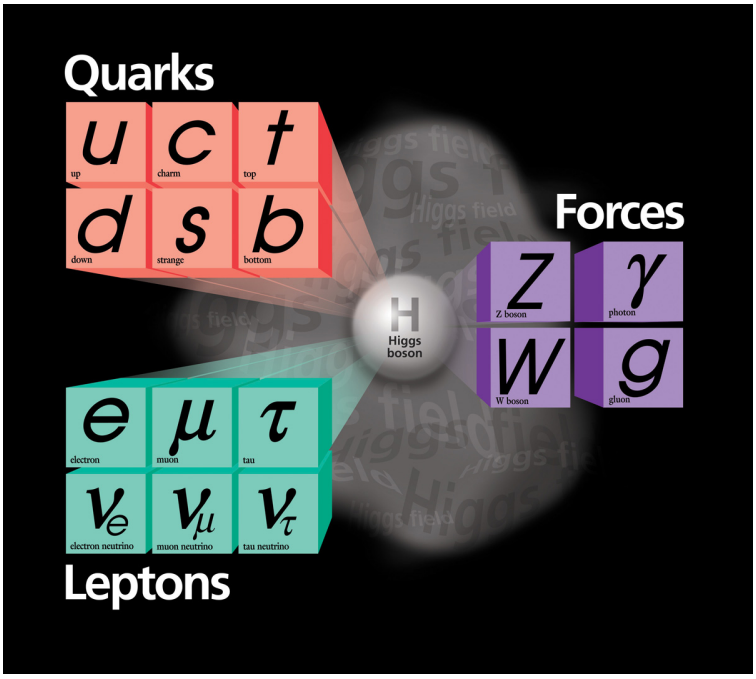

Figure 2.1: Standard Model particles. Figure is taken from [5].

together and form particles (hadrons) with integer charge such as baryons (particles made of three quarks) and mesons (particles made of a quark and an antiquark). There are six quarks grouped in three generations, with the up and down quarks being the first generation, followed by the charm and strange quarks, then the top and bottom quarks. For example, a proton is made of two up quarks with charge of $+\frac{2}{3} \times 2$ and one down quark with charge of $-\frac{1}{3}$, while a neutron is made of one up quark with charge of $+\frac{2}{3}$ and two down quarks with charge of $-\frac{1}{3} \times 2$. So a proton has net charge of +1, whereas a neutron has net charge of 0. There are also six leptons grouped in three generations: the electron and the electron neutrino make the first generation, followed by the muon and muon neutrino, then the tau and tau neutrino. Unlike quarks, electron, muon and tau leptons have integer charges of +1 or -1, whereas the neutrinos are chargeless. The first generations of quarks and leptons are the lightest.

The force carriers (bosons) encompass the gluon that mediates the strong interaction, the $W^{\pm}$ and Z^0 bosons that mediate the weak interaction, the photon that mediates the electromagnetic interactions, and the Higgs boson that gives mass to all the elementary particles. Figure 2.1 summarizes the elementary particles of the Standard Model. Neutrinos are thought to be massless

in the original Standard Model. However, neutrino oscillation experiments indicate that at least two of the three types of neutrinos have non-zero mass. To date, the absolute mass of individual neutrinos are not yet measured.

2.2 Discovery of the Neutrino

The idea of a chargeless and massless particle was first postulated by Wolfgang Pauli in 1930 to explain the then-observed non-conservation of energy and momentum from beta decay: $n^0 \rightarrow p^+ + e^- + \bar{\nu}_e$ [6]. Pauli initially called this particle the 'neutron', but later in 1933, in his beta decay theory, Enrico Fermi renamed it to *neutrino* , which in Italian means 'little neutral one' [7]. This renaming resolved the confusion between Pauli's 'neutron' and another much heavier neutral particle discovered in 1932 by James Chadwick, who also named his discovery 'neutron', as it is still known today [8].

Neutrinos are chargeless, almost massless and weakly interacting. Therefore, neutrinos are extremely hard to detect directly. This hypothesized little neutral particle was undetected for more than two decades. In 1942, Kan Chang Wang first proposed using beta-capture to detect neutrinos [9]. In his short paper published in *Physical Review* on October 13, 1941, he wrote:

"When a β^+-radioactive atom captures a K electron instead of emitting a positron, the recoil energy and momentum of the resulting atom will depend *solely* upon the emitted neutrino, the effect of the extra-nuclear electron being negligible. It would then be relatively simple to find the mass and energy of the emitted neutrino, by measuring the recoil energy and momentum of the resulting atom *alone*."

Tentative identification of neutrinos was achieved in 1953 by an experiment carried out in Hanford by F. Reines and C. L. Cowan Jr. under the auspices of the US Atomic Energy Commission [10]. The confirmation of detection was announced on July 20, 1956 in an issue of *Science* by Cowan *et al.*. In what is now known as the *Cowan-Reines neutrino experiment*, an electron antineutrino coming from nuclear reactor beta decay is captured by a proton and produces a neutron and a positron, $\bar{\nu}_e + p^+ \rightarrow n^0 + e^+$. The neutron captured by the appropriate nucleus would release

one photon (γ), while the positron would quickly annihilate with ambient electrons and would release two γ's. The detection was achieved as described in [11]: "The reaction products were detected as a delayed pulse pair; the first pulse being due to the slowing down and annihilation of the positron and the second to capture of the moderated neutron in cadmium dissolved in the scintillator." The neutrino that participates in β decays and detected in the *Cowan-Reines neutrino experiment* is an electron antineutrino, which accompanies the production of an e^- in the weak interactions.

The first lepton identified is the electron (symbol e^-). The electron has been known indirectly since the ancient Greeks [12]. However, it was not identified as a particle until 1897, by J.J.Thomson and his colleagues. Thomson and his team measured the charge to mass ratio of the electron, $\frac{e}{m}$, to be independent of the source, and the mass of the electron to be about one thousandth of that of the hydrogen ion [13].

Another lepton – the muon (symbol μ), which is in many ways similar to the electron except for being heavier and unstable, was first discovered in 1936 by Carl D. Anderson and Seth Neddermeyer at Caltech from their cosmic radiation studies [14]. Similar to the pairing between an electron and an electron neutrino, it was hypothesized in the 1940's that there is another type of neutrino that accompanies the muon, the muon neutrino. In 1962, Leon M. Lederman, Melvin Schwartz and Jack Steinberger first observed interactions of the muon neutrino. Their discovery was published in *Physical Review Letters* and won them the 1988 Nobel Prize for physics [15].

In 1975, another electron or muon-like particle was first observed in Stanford Linear Accelerator Center (SLAC) [17]. This third lepton is about 17 times heavier than the muon, and it was named the tau lepton (symbol τ). The Standard Model predicts that the tau lepton has an associated neutrino, the tau neutrino. The experiment, Direct Observation of NU Tau (DONUT), was built at FermiLab with the goal of direct detection of tau neutrinos. Protons were accelerated by the Tevatron to 800 GeV and then incident on a high density tungsten target (beam dump) to produce charmed mesons, which decay promptly and produce neutrinos. In particular, the D_s mesons would decay and produce ν_τ. In the experiment, nuclear emulsion targets were used to record the traces of neutrino interactions. At GeV energies, a τ lepton coming out from a ν_τ charged current

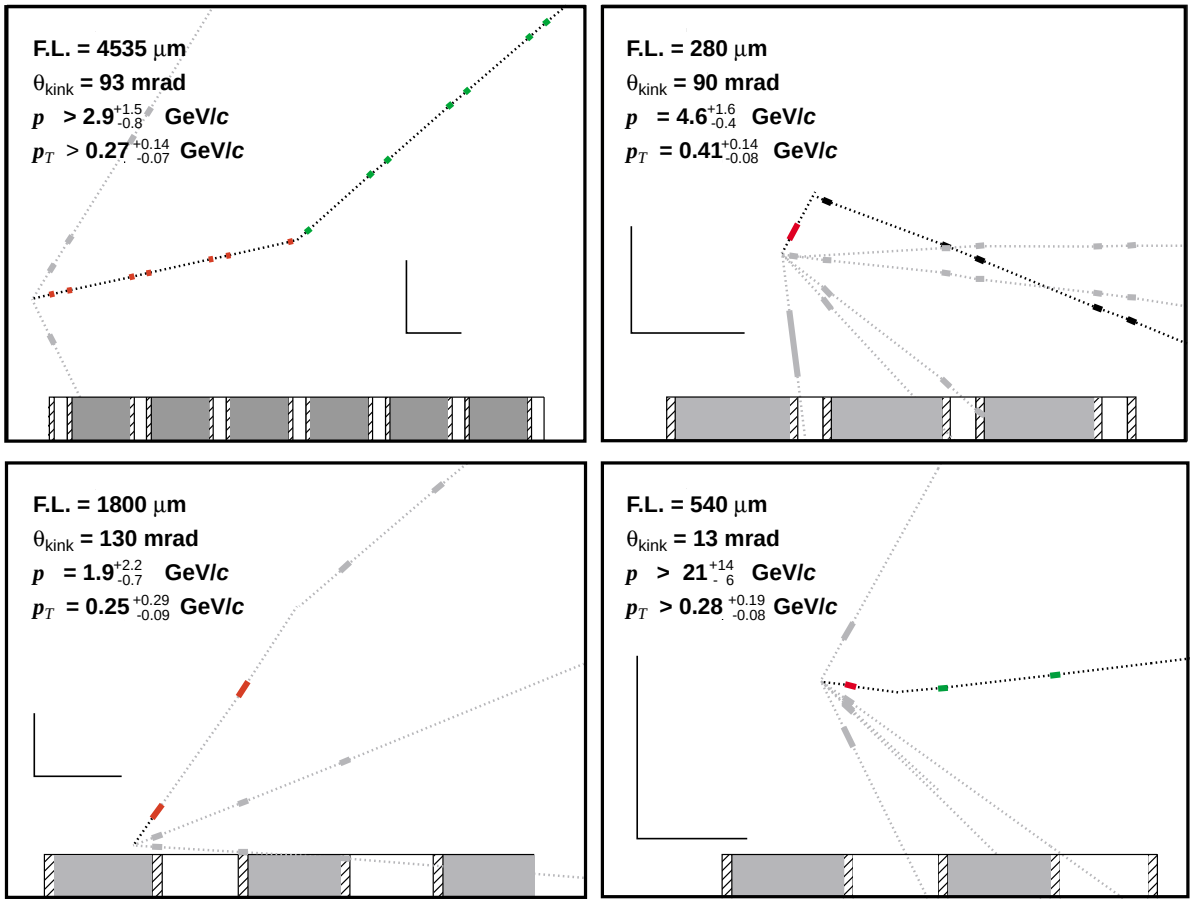

Figure 2.2: Event topologies of ν_τ CC interaction candidates from DONUT. The emulsion target design is shown by the bar at the bottom of each event figure: shading indicates steel, cross-hatching indicates emulsion and unshaded indicates plastic base. Neutrinos are incident from the left, and mostly interact in the steel. The perpendicular lines on each figure give the scales of that figure, with the vertical line representing 0.1mm and horizontal representing 1.0mm. Physical parameters plotted on top left corner of each figure are: F.L. – distance from the kink to the primary vertex, θ_{kink} – angle of kink at the τ decay vertex, p – estimated daughter momentum, and p_T – estimated decay transverse momentum. This figure is taken from [16].

(CC) interaction vertex would decay shortly, making a τ track of millimeter length. About 86% of the time, the decay of a τ lepton produces only one charged daughter [18]. This signature of a τ lepton appearing in the nuclear emulsion films is a track and a kink which indicates a decay that comes with a big transverse momentum. DONUT detected 4 ν_τ candidates with 0.34 estimated background events from their data collected from April to September 1997. This was the first direct observation of ν_τ interactions, Figure 2.2 shows the event topologies of the 4 ν_τ interaction

candidates [16]. Based on these findings, an upper limit on the ν_τ magnetic moment is derived to be $3.9 \times 10^{-7}\mu_B$, where $\mu_B = \frac{e\hbar}{2m_e}$ is the Bohr Magneton [19].

2.3 Neutrinos within the Standard Model

Neutrinos are produced in weak force interactions. The weak force is the force of nuclear transmutation – changing elements from one type to another. All quarks and leptons (fermions) undergo weak interactions. An example of weak interaction is radioactive decay. Unlike the strong force binding nuclei together, the electromagnetic force binding atoms together, and gravity binding massive objects together, the weak force does not have a binding effect. The unique feature of weak interaction is particle type (flavor) change. For example, a neutron decaying into a proton plus an electron and an electron antineutrino involves one of the two *down* quarks in the neutron changing flavor to an *up* quark. The weak force is a short-range force ($\sim 10^{-18}$ m). It is also the weakest among the three (strong, electromagnetic and weak) forces, typically several orders of magnitude lower than the strong force. This is why it gains the name "weak" force. Being the weakest in strength, the weak force also reacts most slowly among the three. The weak interaction occurs on a time scale of $\sim 10^{-8}$ s, while electromagnetic and strong interactions occur on the time scales of 10^{-16} s and 10^{-23} s respectively. When a particle undergoes interactions mediated by the charged $W^{\pm}$ bosons, it is called a charged current (CC) interaction; when mediated by a Z boson, it is called a neutral current (NC) interaction.

The weak force was united with the electromagnetic force under a framework called electroweak theory (EWT), and the weak interaction is the only interaction that does not conserve parity [20]. In the Standard Model, neutrinos are massless and left-handed particles. Helicity relates the intrinsic spin of a particle to its direction of motion. A right helicity particle has its spin aligned with momentum, while a left helicity particle has its spin aligned opposite to momentum. If the weak force conserves parity, a spin-1/2 particle would exist in both left and right helicity states. However, the weak force was soon found to violate parity maximally because it only acts

on the left-handed states of quarks and leptons, regardless of their masses [21]. This maximal parity violation is not unique to neutrinos. Therefore, neutrinos could in principle have a small mass under this scheme.

2.4 Neutrino Oscillations

2.4.1 Neutrino Oscillations in Vacuum

The first compelling evidence for neutrino oscillation was from Super-Kamiokande [22]. The possibility of neutrino-antineutrino flavor transitions was first postulated by Bruno Pontecorvo in 1957 [23, 24]. Formulation of neutrino oscillation was first established by Maki, Nakagawa and Sakata in 1962 and further elaborated by Bruno Pontecorvo in 1967 [25, 24]. Maki *et al.* originally considered only two flavor (ν_e and ν_μ) mixing as only two kinds of neutrinos were known then. Neutrino oscillation can be expressed through a unitary transformation between the mass eigenstates and flavor eigenstates of neutrinos. Neutrinos are produced in flavor eigenstates, which are linear superpositions of their mass eigenstates. Hereafter the neutrino mass eigenstates are denoted as ν_j (j = 1, 2, 3) with Latin indices and flavor eigenstates as ν_α (α = e, μ, τ) with Greek indices. Two sets of eigenstates can be transformed into one another through a unitary matrix – the PMNS (Pontecorvo-Maki-Nakagawa-Sakata) matrix.

Starting from the Schrödinger equation [26],

$$i\frac{d}{dt}\psi = H\psi \tag{2.1}$$

with wave function $\psi = \psi_e|\nu_e\rangle + \psi_\mu|\nu_\mu\rangle + \psi_\tau|\nu_\tau\rangle$ or $\psi = (\psi_e, \psi_\mu, \psi_\tau)^\top$ (ψ_e, ψ_μ and ψ_τ are the coefficients denoting contributions from the corresponding flavor eigenstates), and for relativistic

neutrinos, the Hamiltonian can be approximated as

$$H = U \begin{pmatrix} E + \frac{m_1^2}{2E} & 0 & 0 \\ 0 & E + \frac{m_2^2}{2E} & 0 \\ 0 & 0 & E + \frac{m_3^2}{2E} \end{pmatrix} U^\dagger \tag{2.2}$$

where U is the PMNS matrix and E is the energy for massive neutrinos.

The flavor eigenstates $|\nu_\alpha\rangle$ can be expressed in terms of the PMNS matrix components and the mass eigenstates $|\nu_j\rangle$,

$$\begin{pmatrix} |\nu_e\rangle \\ |\nu_\mu\rangle \\ |\nu_\tau\rangle \end{pmatrix} = \begin{pmatrix} U_{e1} & U_{e2} & U_{e3} \\ U_{\mu 1} & U_{\mu 2} & U_{\mu 3} \\ U_{\tau 1} & U_{\tau 2} & U_{\tau 3} \end{pmatrix} \begin{pmatrix} |\nu_1\rangle \\ |\nu_2\rangle \\ |\nu_3\rangle \end{pmatrix} \tag{2.3}$$

Evolution of the neutrino wave function ψ is described by the scattering matrix, also known as the S-matrix [27]

$$S = e^{-iH} = U \begin{pmatrix} e^{-i(E + \frac{m_1^2}{2E})} & 0 & 0 \\ 0 & e^{-i(E + \frac{m_2^2}{2E})} & 0 \\ 0 & 0 & e^{-i(E + \frac{m_3^2}{2E})} \end{pmatrix} U^\dagger \tag{2.4}$$

The neutrino wave function at time t $\psi(t)$ can be expressed in terms of the S-matrix and the initial wave function $\psi(0)$

$$\psi(t) = S^{-1} \psi(0) S \tag{2.5}$$

The individual elements of the S-matrix are probability transition amplitudes of the initial and final states of the neutrino. Therefore, the neutrino oscillation probabilities from flavor α to flavor

β simply are [26]

$$\begin{aligned} P(\nu_\alpha \to \nu_\beta) &= |S_{\beta\alpha}|^2 \\ &= |U_{\beta j} U^*_{\alpha j} e^{-i m_j^2/2E}|^2 \end{aligned} \tag{2.6}$$

In the two flavor ν_e and ν_μ mixing scheme, the simplest PMNS matrix is a 2D rotation with rotational angle θ , i.e. the mixing angle

$$U = \begin{pmatrix} \cos\theta & \sin\theta \\ -\sin\theta & \cos\theta \end{pmatrix} \tag{2.7}$$

The $\nu_e \to \nu_\mu$ oscillation probability can be directly calculated from Equation 2.6

$$\begin{aligned} P(\nu_e \to \nu_\mu) &= |-\sin\theta\cos\theta e^{-i\frac{m_1^2 L}{2E_\nu}} + \cos\theta\sin\theta e^{-i\frac{m_2^2 L}{2E_\nu}}|^2 \\ &= \sin^2 2\theta \sin^2 \frac{\Delta m^2 L}{4E_\nu} \end{aligned} \tag{2.8}$$

Another step-by-step derivation of $\nu_e \to \nu_\mu$ oscillation probability after ν_e traversing time t and distance L is shown below following a procedure as introduced in [21]. These two procedures will give the same result.

$$\begin{pmatrix} \nu_e \\ \nu_\mu \end{pmatrix} = \begin{pmatrix} \cos\theta & \sin\theta \\ -\sin\theta & \cos\theta \end{pmatrix} \begin{pmatrix} \nu_1 \\ \nu_2 \end{pmatrix} \tag{2.9}$$

Assume ν_e is the neutrino flavor at source of production, at time t=0

$$|\nu_e(0)\rangle = \cos\theta|\nu_1\rangle + \sin\theta|\nu_2\rangle \tag{2.10}$$

At time t

$$|\nu_e(t)\rangle = \cos\theta e^{-iE_1 t}|\nu_1\rangle + \sin\theta e^{-iE_2 t}|\nu_2\rangle \tag{2.11}$$

Let $\hbar$=c=1, E_1 and E_2 can be approximated as

$$E_k = \sqrt{p^2 + m_k^2} = p\sqrt{1 + \frac{m_k^2}{p^2}} \simeq p + \frac{m_k^2}{2p} \tag{2.12}$$

Assume that the two mass eigenstates have same momentum. For relativistic neutrinos, $E_\nu \gg$m. Hence, $E_\nu \simeq$ p. Also, time t = $\frac{L}{c}$ = L. Therefore:

$$E_k \simeq E_\nu + \frac{m_k^2}{2E_\nu} \tag{2.13}$$

$$\begin{aligned} |\nu_e(t)\rangle &= \cos\theta e^{-i(E_\nu + \frac{m_1^2}{2E_\nu})L}|\nu_1\rangle + \sin\theta e^{-i(E_\nu + \frac{m_2^2}{2E_\nu})L}|\nu_2\rangle \\ &= e^{-i(E_\nu + \frac{m_1^2}{2E_\nu})L}\left[\cos\theta|\nu_1\rangle + \sin\theta|\nu_2\rangle e^{i\frac{\Delta m^2 L}{2E_\nu}}\right] \end{aligned} \tag{2.14}$$

with $\Delta m^2 = m_1^2 - m_2^2$. The ν_μ flavor eigenstate is

$$|\nu_\mu\rangle = -\sin\theta|\nu_1\rangle + \cos\theta|\nu_2\rangle \tag{2.15}$$

Using the orthonormality relation $\langle\nu_i|\nu_j\rangle = \delta_{ij}$ (i, j = 1, 2), the probability of a ν_e changing to a ν_μ after traversing distance L (in vacuum) is

$$\begin{aligned} P(\nu_e \to \nu_\mu) &= |\langle\nu_\mu|\nu_e(t)\rangle|^2 \\ &= |-\sin\theta\cos\theta + \cos\theta\sin\theta e^{i\frac{\Delta m^2 L}{2E_\nu}}|^2 \\ &= \sin^2 2\theta \sin^2\frac{\Delta m^2 L}{4E_\nu} \end{aligned} \tag{2.16}$$

Equations 2.8 and 2.16 show that the neutrino oscillation probability is maximal when $\frac{\Delta m^2 L}{2E_\nu} = n2\pi$ (n = 1, 2, 3, ...). The intrinsic mixing angle $\sin^2 2\theta$ determines the oscillation amplitude, which is maximal when $\theta = \frac{\pi}{4}$. The oscillation probability does not independently depend on L and E_ν, instead it only depends on the ratio of $\frac{L}{E_\nu}$. Therefore, a neutrino experiment with fixed baseline can only probe a small region of the neutrino energy spectrum. To study neutrinos globally, it is

essential to have experiments with various baselines to provide data points at different regions of the neutrino energy spectrum.

Neutrino oscillation with three flavor mixing is more complicated than two flavor mixing. The PMNS matrix for three flavor mixing can be parametrized to have only three mixing angles θ_{12}, θ_{13} and θ_{23}, and a complex phase term δ which is a CP violation indicator in the neutrino sector. The simplified PMNS matrix for three flavor mixing is [26]

$$\begin{aligned} U &= \begin{pmatrix} 1 & 0 & 0 \\ 0 & c_{23} & s_{23} \\ 0 & -s_{23} & c_{23} \end{pmatrix} \begin{pmatrix} c_{13} & 0 & s_{13}e^{-i\delta_{CP}} \\ 0 & 1 & 0 \\ -s_{13}e^{i\delta_{CP}} & 0 & c_{13} \end{pmatrix} \begin{pmatrix} c_{12} & s_{12} & 0 \\ -s_{12} & c_{12} & 0 \\ 0 & 0 & 1 \end{pmatrix} \\ &= \begin{pmatrix} c_{12}c_{13} & s_{12}c_{13} & s_{13}e^{-i\delta_{CP}} \\ -s_{12}c_{23} - c_{12}s_{13}s_{23}e^{i\delta_{CP}} & c_{12}c_{23} - s_{12}s_{13}s_{23}e^{i\delta_{CP}} & c_{13}s_{23} \\ s_{12}s_{23} - c_{12}s_{13}c_{23}e^{i\delta_{CP}} & -c_{12}s_{23} - s_{12}s_{13}c_{23}e^{i\delta_{CP}} & c_{12}c_{23} \end{pmatrix} \end{aligned} \tag{2.17}$$

with $c_{ij} = \cos\theta_{ij}$ and $s_{ij} = \sin\theta_{ij}$. Three flavor oscillation probabilities can be computed based on Equation 2.6.

The $\bar{\nu}_e \to \bar{\nu}_e$ disappearance channel is important in reactor neutrino oscillation experiments and the measurement of the so-called solar mixing parameters Δm^2_{12} and θ_{12}. KamLAND is the first reactor experiment to have measured the periodic $\bar{\nu}_e$ survival probabilities using the $\bar{\nu}_e$ disappearance channel [28]. A combined global fit analysis of the KamLAND results and the solar neutrino flavor conversion results from experiments such as SNO (heavy water), Kamiokande/Super-Kamiokande (water), Borexino (liquid scintillator) and others have found the solar mixing angle to be $\tan^2\theta_{12} = 0.436^{+0.029}_{-0.025}$ with significance over 5σ [29].

The third mixing angle θ_{13} was thought to be very small but non-vanishing. With $L \sim$1 km, $\langle E \rangle \sim$3 MeV, the $\bar{\nu}_e$ disappearance experiment is sensitive to $\frac{E}{L} \sim 3\times10^{-3}$ eV^2. The Double Chooz experiment is the first experiment targeting the measurement of θ_{13} using reactor $\bar{\nu}_e$ [30, 31]. Recent results reported by reactor experiments Daya Bay [32] and RENO [33] were the first to unambiguously show the third mixing angle to be $\sin^2(2\theta_{13}) \sim$0.1 with significance over 5σ.

The $\nu_\mu \to \nu_e$ channel is an important channel to explore in neutrino experiments because it is easy to make a beam of ν_μ at accelerators. The K2K [34], MINOS [35] and T2K [36] experiments are long-baseline accelerator-based neutrino experiments with near and far detectors to explore ν_μ disappearance and/or ν_e appearance channels.

Another channel using ν_μ beams is the $\nu_\mu \to \nu_\tau$ channel. Atmospheric ν_μ disappearance was first measured unambiguously by the Super-Kamiokande experiment and the atmospheric mixing angle θ_{23} was found to be maximally mixing, $\theta_{23} \simeq \frac{\pi}{4}$ [22]. The τ neutrino is the least explored among the three neutrino species, $\nu_\mu \to \nu_\tau$ is theoretically viable but not yet conclusively proved by experiments. Experiments searching for ν_τ events are usually called ν_τ appearance experiments. By 2012, the Super-Kamiokande experiment has measured the atmospheric ν_τ appearance to a significance of 3.8 σ over a non-appearance hypothesis using 15 years of collected data [37]. The OPERA[1] experiment located at Gran Sasso, Italy utilizes the ν_μ beam generated at CERN to look for ν_τ appearance after the ν_μ traverse a distance of $\sim$ 700 km from CERN to Gran Sasso. Since the first ν_τ candidate event announced by OPERA in May 2010, two more ν_τ candidate events were reported by OPERA in 2012 and 2013 respectively [38, 39, 40]. The significance over a null hypothesis based on these three ν_τ candidates is 3.5 σ [29].

2.4.2 Neutrino Flavor Changing in Matter

Neutrinos traversing matter could have their oscillation patterns modified drastically compared to vacuum as neutrinos can interact with the particles forming the matter. This effect was first treated by Wolfenstein, Mikheyev and Smirnov and often called the MSW effect [41].

The Hamiltonian for neutrinos in matter is $H_m = H_0 + H_{\text{int}}$, where H_0 is the Hamiltonian in vacuum and H_{int} describes the interaction between neutrino and matter. The scattering of ν_e, ν_μ and ν_τ on the ambient electrons, protons and neutrons in the matter due to H_{int} could change the states of the initial particles and cause coherence loss between the neutrino states (more detailed discussion in Section 2.4.3). Consider the case of $\nu_e \leftrightarrows \nu_\mu$ conversion in matter with constant density. The mass eigenstates $|\nu_1\rangle$ and $|\nu_2\rangle$ in vacuum are not eigenstates of the Hamiltonian H_m.

[1] Oscillation Project with Emulsion-tRacking Apparatus

Relations between the eigenstates $|\nu_1^m\rangle$ and $|\nu_2^m\rangle$ for H_m and $|\nu_e\rangle$ and $|\nu_\mu\rangle$ can be expressed as [29]

$$|\nu_e\rangle = |\nu_1^m\rangle \text{cos}\theta_m + |\nu_2^m\rangle \text{sin}\theta_m \tag{2.18}$$

$$|\nu_\mu\rangle = -|\nu_1^m\rangle \text{sin}\theta_m + |\nu_2^m\rangle \text{cos}\theta_m \tag{2.19}$$

where θ_m is the neutrino mixing angle in matter. Then θ_m can be written as

$$\text{sin}2\theta_m = \frac{\text{tan}2\theta}{\sqrt{(1-\frac{N_e}{N_e^{\text{res}}})^2 + \text{tan}^2 2\theta}} \tag{2.20}$$

$$\text{cos}2\theta_m = \frac{1 - N_e/N_e^{\text{res}}}{\sqrt{(1-\frac{N_e}{N_e^{\text{res}}})^2 + \text{tan}^2 2\theta}} \tag{2.21}$$

where N_e^{res} is called resonance density

$$N_e^{\text{res}} = \frac{\Delta m^2 \text{cos}2\theta}{2E\sqrt{2}G_F} \tag{2.22}$$

where Δm^2 is the mass squared difference between the two vacuum mass eigenstates, θ is the mixing angle in vacuum, E is the energy of the primary neutrino and G_F is the Fermi constant.

Therefore, the presence of matter can lead to strong enhancement of flavor change when the matter density is approaching the resonance condition as shown in Equation 2.22. For antineutrinos, the mixing angle in matter can be derived similarly by replacing N_e with $-N_e$. These formulae also hold for the case of $\nu_e \leftrightarrows \nu_\tau$ conversion. In particular, when ν_e traverse the Earth or the Sun where electron densities are high, the flavor conversion probabilities of ν_e to ν_μ or ν_τ are modified. However, for the case of $\nu_\mu \leftrightarrows \nu_\tau$ conversion in the Earth or the Sun, it is practically like vacuum [29].

2.4.3 Coherence in Neutrino Oscillations

To fully understand the phenomenon of neutrino oscillations, the localization of microscopic processes on how a neutrino is produced and detected must be scrutinized. The localization of neutrino oscillations during propagation can be modeled by a three-dimensional wave packet approach which was first proposed by Nussinov in 1976 [42]. This wave packet approach inevitably suggests the existence of a coherence length for neutrino oscillations. Neutrinos are created in their weak interaction states (flavor states), which are superpositions of mass eigenstate wave packet states. Assuming that the mass eigenstate wave packets have equal energy (or equal momentum), they will travel at different group velocities. Therefore, the neutrino flavor wavepacket which consists of the mass eigenstate wave packets will spread out or come apart during propagation. When the mass eigenstates are so spread out that no interference among them could occur, it is said that this neutrino state has lost coherence. Neutrino oscillation is only viable when coherence is sustained. However, the detection of neutrino oscillation at a detector which involves time and space integration and averaging does not necessarily require coherence [43]. For relativistic neutrinos, the equal energy and equal momentum scenario assumptions are equivalent [44]. Since neutrino masses are very small, the approximation of ultrarelativistic neutrinos in most wave packet treatments is very good [44, 45]. In 1996, Kiers, Nussinov and Weiss first pointed out that the process of detection is essential for coherence of neutrino oscillations [46]. In their paper, they addressed the effect of coherent and incoherent broadening on neutrino oscillations based on the example of ν_e production in the Sun from e^- captured on Be,

$$^7Be + e^- \rightarrow ^7 Li + \nu_e \tag{2.23}$$

They defined the ν_e coherence length L_{max} as the distance where neutrino with energy E has gone through one more oscillation than a neutrino with E+ΔE:

$$L_{max} = \frac{4\pi E^2}{(\Delta m^2)\Delta E} = L_{osc}\frac{E}{\Delta E} \tag{2.24}$$

where $L_{osc} = \frac{4\pi E_\nu}{\Delta m^2}$ is the neutrino oscillation length, and ΔE is the energy spread of the neutrino

beam. Hence, there is a maximum number of oscillations for a propagating neutrino $N_{max} = \frac{L_{max}}{L_{osc}}$. Coherent broadening is the spread of δE of a single neutrino, which can lead to loss of oscillation pattern. Coherence broadening processes include the natural width of the emitting nucleus, pressure broadening from collision and the finite size of the wave packet of the captured electron. Realistically, the neutrino beam created at the origin is incoherent due to the slightly different energies of each individual neutrino, which gives rise to the energy spread of ΔE of the neutrino beam in Equation 2.24. This incoherent broadening mainly results from the energy spread of the captured electron and the Doppler shift from the thermal motion of the emitting nucleus. The authors then examined the distinguishability between this two scenarios at the detector and they reached the conclusion that although the physical processes that cause the incoherence and coherence broadenings of neutrino states are distinct at the source, they can not be distinguished at the detector even with the matter effect (MSW effect) taken into account.

The wave packet size is an essential parameter in evaluating coherence condition for neutrino oscillations, it is determined by the properties of the environments where neutrinos are produced. In the plasma medium of a supernova, the neutrino wave packet size is approximated as [47]

$$\sigma_x \simeq \frac{l}{v/c} \simeq (1.26 \times 10^{23}) \frac{\sqrt{m} T^{\frac{3}{2}}}{Z_1^2 Z_2^2 N} \text{ cm} \tag{2.25}$$

where l is the mean free path of the parent particle which produces neutrino and v is its velocity. Z_1 and Z_2 are the charges of the particles that produce the neutrinos and the plasma particles. T and m are in MeV and N is in cm^{-3}. The oscillation and coherence lengths in vacuum are

$$L_{osc} = \frac{4\pi E}{\Delta m^2}, \quad L_{coh} = \frac{4\sqrt{2}\sigma_x E^2}{\Delta m^2} \tag{2.26}$$

For neutrinos in matter, the oscillation and coherence lengths are

$$L_{osc}(X) \equiv \frac{4\pi E X}{\int_0^L dx \Delta\mu_{ab}^2(X)}, \quad L_{coh}(X) \simeq \frac{4\sqrt{2}\sigma_x E^2 X}{\int_0^L dx \Delta\mu_{ab}^2(X)} \tag{2.27}$$

with $\Delta\mu_{ab}^2$ being the mass squared difference in matter (effective mass squared difference) and X

representing the distance that the neutrinos have traveled. The condition that guarantees neutrino oscillation is

$$L_{coh} > L_{osc} \tag{2.28}$$

Based on formulas 2.25 and 2.26 and the typical Δm^2, the wave packet sizes, oscillation and coherence lengths for solar, reactor and accelerator neutrinos are computed and summarized in Table 2.1.

Table 2.1: Wave packet sizes, oscillation lengths and coherence lengths for solar, reactor and accelerator neutrinos in vacuum [47].

Experiment	$\Delta m^2(eV^2)$	E(MeV)	σ_x(cm)	L_{coh}(km)	L_{osc}(km)
Solar	7.3×10^{-5}	10	3.15×10^{-7}	2.44×10^{7}	3.40×10^{2}
Reactor	7.3×10^{-5}	1	5.1×10^{-4}	3.95×10^{8}	3.40×10^{1}
Accelerator	1.0×10^{-3}	10^3	1.0×10^{2}	5.65×10^{18}	2.48×10^{3}

Therefore, solar neutrinos en route to earth lose coherence and freeze out before reaching the earth (Earth-Sun distance $\sim 1.5\times 10^8$ km). Terrestrial neutrinos that are produced and detected on Earth always maintain coherence.

2.5 Neutrino Sources

Despite their elusiveness, neutrinos are very common particles in the universe. Figure 2.3 summarizes neutrino fluxes as a function of energy from various sources.

2.5.1 Cosmological Neutrinos

The standard theory of cosmology says that the universe started with a big bang about 14 billion years ago. Shortly ($<10^{-34}$ s) after the big bang, the universe underwent an exponential expansion known as inflation. The big-bang nucleosynthesis (BBN) predicts that when the universe was seconds old, a sequence of nuclear reactions produced light elements D, ^{3}He, ^{4}He and ^{7}Li. Measurements of ^{4}He abundance yield stringent limits on the number of active neutrino species N_ν as

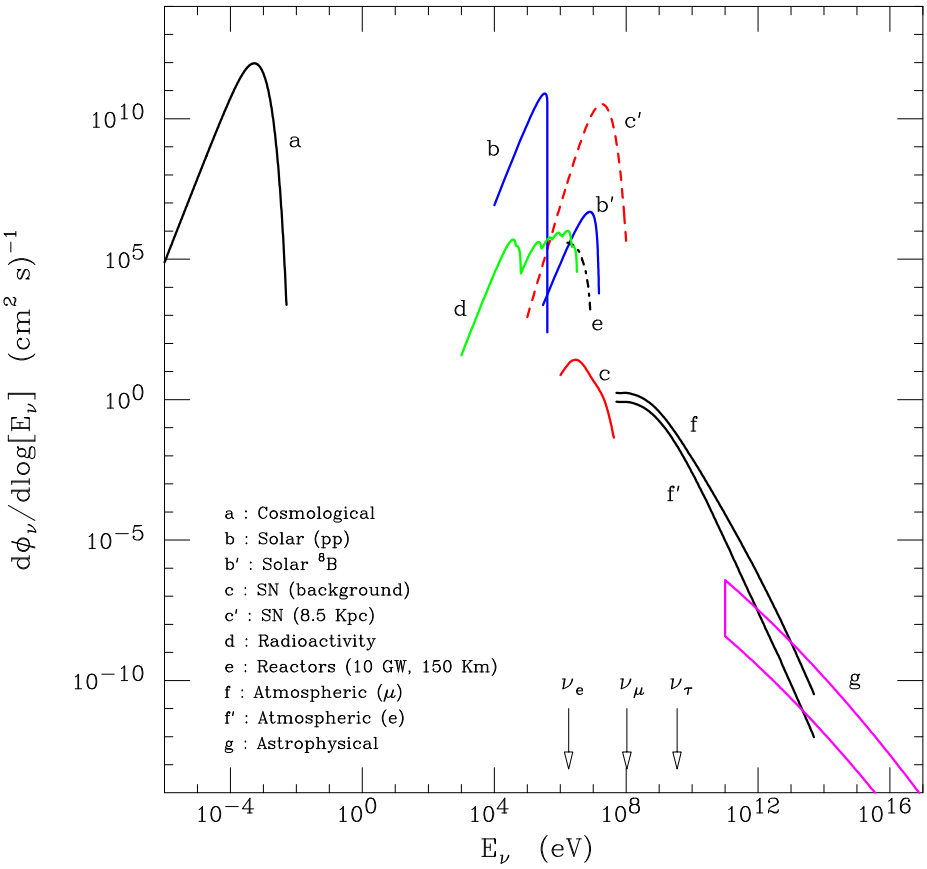

Figure 2.3: Neutrino fluxes as a function of energy from various sources. Figure is taken from [48].

the abundance of ^{4}He increases with N_ν. The current limit for active neutrino species from cosmological measurement is $N_\nu^{\text{eff}} \leq 3.7$ [49], while the measurement obtained from accelerator studies is $N_\nu = 2.9840 \pm 0.0082$ from the LEP experiment [29].

The critical energy density ρ_{crit} of the universe determines if the universe is ever-expanding and eventually turns into a cold dark lifeless place or recontracting after some time. Current calculation of ρ_{crit} is $\sim 8.4 \times 10^{-30}$ g cm^{-3}. Today, it is known that the universe is composed of 71.4% of dark energy which is believed to account for the accelerating expansion of the universe, 24% of dark matter and 4.6% ordinary matter [50]. In addition, the mass-energy composition of the Universe includes $\sim$ 0.002% photons and between 0.06% and 0.2% neutrinos, which is estimated based on the lower (0.06 eV) and upper (0.23 eV) limits of total neutrino mass $\sum m_\nu$ [29].

The 2.728 K cosmic microwave background (CMB) is relic radiation from the universe becoming transparent at an age of $\sim$ 300,000 years. The CMB has been well explored [51, 52, 53] since its discovery in 1964 by Penzias and Wilson [54]. The photon density of the CMB is $n_\gamma \simeq 412$ cm^{-3} [48]. Relic neutrinos from the big bang were produced in the early epochs of the evolution of the universe. They decoupled from the hot quark-and-lepton soup well before it became transparent. There should be three (ν_e, ν_μ and ν_τ) relic neutrino populations, for the weak interaction between neutrinos and electrons, positrons and nucleons brought neutrinos to thermal equilibrium when the universe was less than a second old. The black-body spectrum temperature associated with the relic neutrinos is $T_\nu \simeq 1.947$ K, equivalent to an average kinetic energy of 5×10^{-4} eV [48]. The relic neutrino abundance is comparable to that of the CMB, $n_\nu \simeq \frac{3}{11} n_\gamma \simeq 113$ cm^{-3} per species [55].

2.5.2 Solar Neutrinos

Stars produce energy through nuclear fusion. In the sun, about 98.5% of the energy is from burning hydrogen gas into helium (pp cycles) [48]. Neutrinos are produced copiously during the effective nuclear reaction chain

$$4p + 2e^- \rightarrow {}^4He + 2\nu_e + 26.73 \text{ MeV} \tag{2.29}$$

The energy released from this reaction chain is the binding energy of the protons $Q = 4m_p^2 + 2m_e^2 - m_{He} = 26.73$ MeV. Neutrinos produced are mostly with energy below 0.41 MeV. The ν_e flux from the sun arriving at earth can be estimated based on the luminosity of the sun, the distance between the earth and the sun and the energies released in fusion cycles

$$\Phi_{\nu_e} \simeq \frac{2L_\odot}{4\pi d_\odot^2 \left(Q - \langle E_\nu \rangle\right)} \tag{2.30}$$

where $L_\odot = 3.842 \times 10^{33}$ erg/s is the solar luminosity, $d_\odot = 1.495 \times 10^{11}$ m is the distance between the sun and the earth, and $\langle E_\nu \rangle \simeq 0.3$ MeV is the average energy carried away by the neutrino in one fusion cycle. Based on Equation 2.30, the neutrino flux at earth is estimated to be

$\Phi_\odot \sim 6 \times 10^{10}$ cm^{-2} s^{-1}. Solar neutrino flux predictions largely depend on the structure of the sun, element composition, temperature and rates of all fusion cycles. Measurement of solar neutrinos can help to test the standard solar models [56].

2.5.3 Geophysical Neutrinos

Anti-neutrinos from natural radioactivity are produced through β decay of heavy nuclei. About 36% of the earth's energy output is from uranium and thorium decay. Uranium and thorium concentrates in the crust and mantle of the Earth. β decay of these nuclei should generate a geophysical neutrino ($\bar{\nu}_e$) flux of $\sim 10^6$ cm^{-2} s^{-1}. Precise measurement of the geophysical neutrinos could shed light on the geophysical structures of the Earth [48, 57].

2.5.4 Reactor and Accelerator Neutrinos

Ever since neutrinos were first detected in 1956, experiments to understand the intrinsic properties of the neutrinos have been carried out through both reactor and accelerator experiments.

Reactor Neutrinos

Nuclear reactors generate power through nuclear fission that usually occurs with a sequence of β-decays releasing $\bar{\nu}_e$ in chain reactions. Taking the fission fuel ^{235}U as an example, in every fission about 6 $\bar{\nu}_e$ and 200 MeV are produced [58]

$$^{235}U + n \rightarrow X_1 + X_2 + 2n \tag{2.31}$$

where X_1 and X_2 are two unequal fragments. The lighter and heavier fragments have $A \simeq 94$ and $A \simeq 140$ on average respectively. For these two fragments to reach stability, a total of 6 n have to undergo β decay so as to be in their stable states of ^{94}Zr$_{94}$ and ^{140}Ce$_{58}$, yielding 6 $\bar{\nu}_e$ per complete fission chain.

Accelerator Neutrinos

Beams of ν_μ can be produced in the beam stop of a proton accelerator. Processes to produce neutrinos in accelerator neutrino experiments are:

$$N + p \rightarrow \pi^+ \rightarrow \mu^+ + \nu_\mu \tag{2.32}$$

$$\mu^+ \rightarrow \bar{\nu}_\mu + e^+ + \nu_e \tag{2.33}$$

$$\pi^- \rightarrow \mu^- + \bar{\nu}_\mu \tag{2.34}$$

$$\mu^- \rightarrow \nu_\mu + e^- + \bar{\nu}_e \tag{2.35}$$

First of all, hadrons are produced at the target. Then, the resulting hadrons including pions are collected by a focusing magnetic horn from the target, which will direct pions with one charge (π^+ or π^-) to the downstream experiment. A ν_μ or $\bar{\nu}_\mu$ beam will be made when pions decay to neutrinos prior to the beam dump. Some muons with long lifetime will decay into $\bar{\nu}_e$ or ν_e, which adds a background to the ν_μ or $\bar{\nu}_\mu$ beam [59].

2.5.5 Atmospheric Neutrinos

Neutrinos are also produced in the Earth's atmosphere when cosmic rays collide with the air nuclei in the atmosphere. The neutrino production in the atmosphere is similar to that of accelerator beam dump as described in Section 2.5.4. Since atmospheric neutrinos are the main neutrino background at IceCube, the creation mechanism and energy spectrum of atmospheric neutrinos will be discussed in detail in Chapter 3.

2.5.6 Astrophysical Neutrinos

Since cosmic rays were discovered near a century ago, ultra high energy (UHE, up to 10^{20} eV) cosmic rays have been detected at Earth. Even though the origin of the charged cosmic rays is still unknown, it is believed that the production sites of those UHE cosmic rays also produce high

energy neutrinos via either proton-proton collision or proton-photon collision and their subsequent pion decays. Candidate sites for high energy astrophysical neutrinos are Active Galactic Nuclei (AGNs) and Gamma Ray Bursts (GRBs) which are the most energetic objects ever detected in the distant universe. Exploding stars or supernovae (SNe) could also produce streams of neutrinos, typically with energies lower than those associated with UHE cosmic rays. Astrophysical neutrinos will be covered more in detail in Chapter 3.

Chapter 3

Neutrino Astronomy

This chapter discusses how neutrinos have gained prominence in astronomy. It begins with the discovery, energy spectra, acceleration mechanism and possible source candidates for cosmic rays. Then, the astrophysical neutrinos which are closely related to the highest energy cosmic ray acceleration sites such as AGNs and GRBs are introduced. In Section 3, the major background for astrophysical neutrino detection, the atmospheric neutrinos, are summarized. Section 4 briefly summarizes the existing experiments to detect astrophysical neutrinos.

3.1 Cosmic Rays

3.1.1 Discovery

In the late 1900's, Theodor Wulf invented the electrometer and used it to study radiation rates at the top and bottom of the Eiffel Tower [60]. His findings indicated that radiation at the top of the building is higher than that at the bottom. In 1911 and 1912, Domenico Pacini and Victor Hess carried out independent experiments to measure ionization rates at different altitudes [61, 60]. In Hess' experiment, he carried three electroscopes (enhanced precision Wulf electrometers) during free balloon flights up to an altitude of 5.3 kilometers. Those flights took place during both day and night. His experimental results showed that radiation decreased up to an altitude of around 1 kilometer and then increased as a function of altitude. At an altitude of 5.3 km, the radiation

intensity is about twice that at ground level. He concluded that there must be radiation coming from outer space penetrating the earth's atmosphere [60]. Hess' findings were confirmed by similar balloon flight experiments to higher altitudes ($\sim$ 9 km) and Hess won the Nobel Prize in Physics in 1936. Cosmic radiation was initially thought to be of electromagnetic nature like X-rays and gamma-rays, and hence gained the name "cosmic rays" from Robert A. Milikan who also proved them to be of extraterrestrial origin in 1926 [62]. Cosmic rays were demonstrated to be very energetic charged particles during 1928 and 1929 [63]. Nowadays, the term cosmic ray is still in use as a convenient synonym for an energetic charged particle from space.

3.1.2 Cosmic Ray Composition and Energy Spectra

Cosmic rays comprise stable charged particles that are constantly bombarding the Earth's atmosphere. Primary cosmic rays ("primaries") include protons, electrons, helium, carbon, oxygen, iron and other nuclei synthesized in stars. About 79% of the primaries are free protons and about 15% are helium nuclei [29].

Figure 3.1 shows the cosmic ray all-particle energy spectrum at Earth as a function of energy per nucleon. The spectrum is cut off below a few GeV due to the geomagnetic field. Above the geomagnetic cutoff and out to $O(100)$ TeV, the cosmic ray energy spectrum can be modeled by a power law [29]

$$\frac{dN}{dE} \sim 1.8 \times 10^4 (\frac{E}{1\text{GeV}})^{-2.7} \frac{\text{nucleons}}{\text{GeV m}^2 \text{ sr s}} \tag{3.1}$$

where E is the energy per nucleon, including rest energy. Between 10^{15} eV and 10^{16} eV, there is a steepening in the spectrum known as the "knee", above which the energy spectrum softens from $E^{-2.7}$ to $\sim$E^{-3}. Above $\sim 10^{18.5}$ eV, the spectrum hardens again, this feature is known as the "ankle". Above $\sim 5 \times 10^{19}$ eV, a suppression in the energy spectrum is expected due to the GZK cutoff as a result of ultra-high-energy cosmic rays (UHECRs) interacting inelastically with the cosmic microwave background. The GZK mechanism predicts that the UHECRs are confined to a horizon of $\sim$50 megaparsec (Mpc) [64, 65]. Above $\sim O(100)$ TeV, the cosmic ray flux is

$\sim$1 m^{-2} yr^{-1}, while above $\sim 10^{18}$ eV, this number drops to 1 km^{-2} yr^{-1}. Therefore, even though it is practical to observe cosmic rays through balloon-borne or satellite-borne experiments below $\sim$100 TeV, the highest energy ($>$ 100 TeV) cosmic rays have to be observed by large air shower arrays. An air shower is produced when a cosmic ray primary is energetic enough that the cascade it produces via interaction with the atmosphere is detectable at the ground. The Pierre Auger Observatory is the world's largest UHECR observatory, covering a detection area of 3000 km^2 [66].

3.1.3 Cosmic Ray Origin Candidates

Cosmic rays are deflected in magnetic fields owing to their charge, hence their arrival directions at Earth are almost completely scrambled – with isotropy observed to the level of $\sim 10^{-4}$ [68]. While the low to intermediate energy cosmic rays are expected to at least partially originate from the Galaxy, the sources of ultra-high-energy cosmic rays (UHECRs, $E > 10^{18}$ eV) are still actively ongoing research topics for various experiments with different detection channels and techniques. In principle, there are two fundamental scenarios to explain the production of highest energy cosmic rays. One is the so called *top-down* model and the other is the *bottom-up* model. In the top-down scenario, the UHECRs are expected to be produced locally through decays of massive Grand Unification Theory (GUT) particles with masses up to 10^{24} eV – the GUT scale. Protons produced this way could reach energies up to 10^{22} eV. However, the absence of an expected large flux of accompanying neutrinos and photons suggests that the top-down model is not favored. Also, the GZK suppression would have been avoided since these UHECRs can be produced locally. Yet, the observation of suppression in the highest energy cosmic ray spectrum [69] do indicate consistency with the GZK cutoff and hence the top-down model is disfavored [70]. The bottom-up scenario suggests that UHECRs are accelerated in magnetized plasmas in distant astrophysical sources. Intermediate energy cosmic rays ($< 10^{18}$ eV) are thought to be accelerated within the Galaxy, in sources such as supernovae remnants. Signatures of gamma rays ($\pi^0 \rightarrow \gamma\gamma$) suggest that magnetic clouds from supernovae remnants partially account for the acceleration of the intermediate energy cosmic rays [71]. Extremely high energy cosmic rays ($> 10^{18}$ eV) are expected to originate from

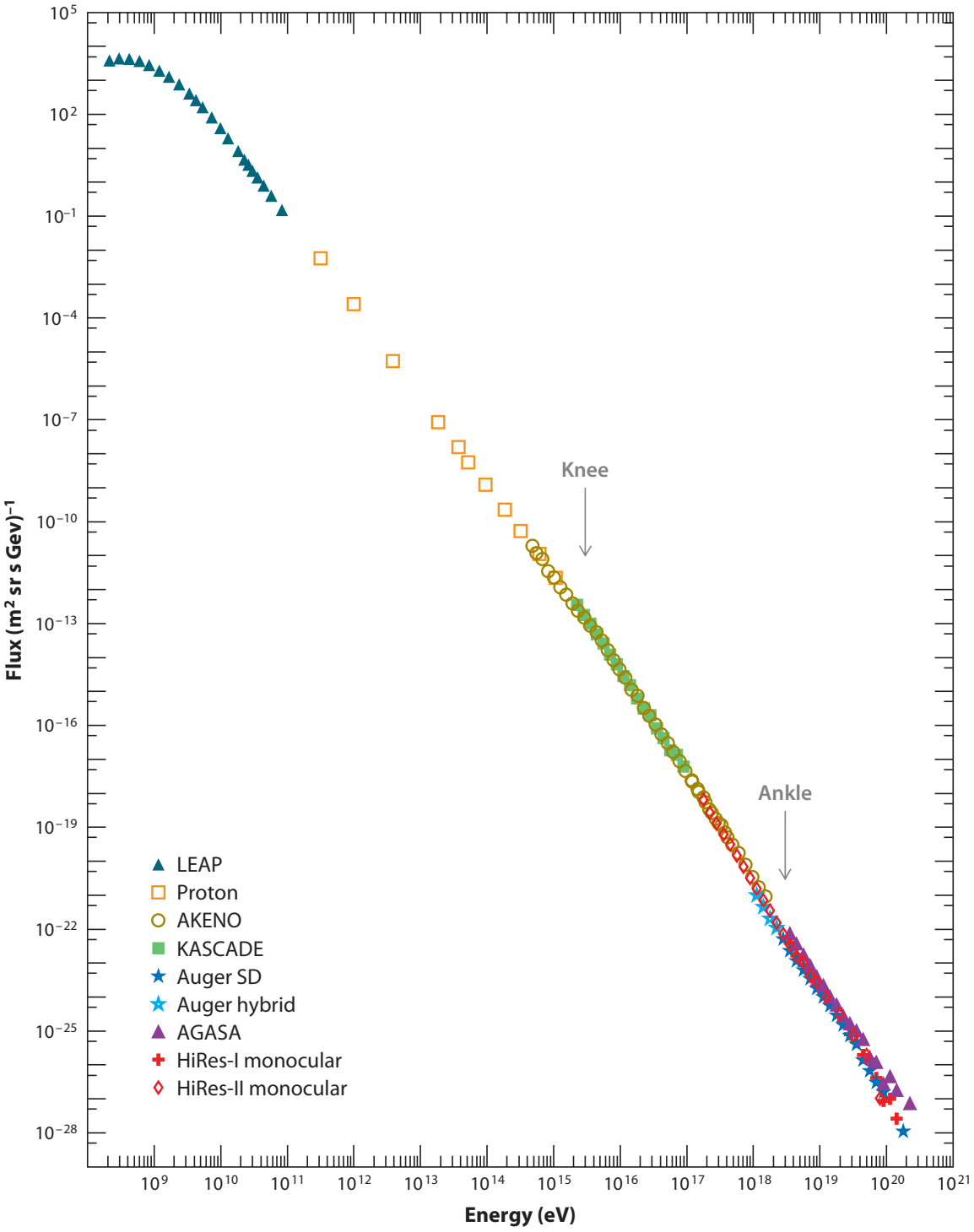

Figure 3.1: All particle cosmic ray energy spectrum. Figure is taken from [67].

extragalactic sources with strong magnetic fields present, such as Active Galactic Nuclei (AGN) [72, 73] and Gamma Ray Bursts (GRBs) [74].

3.1.4 Fermi Acceleration

The theory of UHECRs being accelerated stochastically in irregular magnetized plasmas was first proposed by Fermi in 1949 [75]. Energetic astrophysical phenomena such as supernovae explosions, galaxies merging and AGN jets would provide violent shock wave environments, which are ideal sites to accelerate the UHECRs. In strong astrophysical shock waves, charged particles gain energy stochastically through collisions with inhomogeneous magnetic fields. The original Fermi acceleration model leads to a second order energy gain for each complete chain of collisions when a charged particle exits the magnetic clouds: $\frac{\Delta E}{E} \propto (\frac{V}{c})^2$ with V being the characteristic velocity of the magnetic clouds. Assuming the particle being accelerated in the shock waves has an escape time scale of τ_{esc}, the resulting energy spectrum of the particles will be a power law distribution, which matches the observed power law spectrum for the cosmic rays as aforementioned. The derivation of this result can be achieved by requiring the steady-state solution for the generic diffusion-loss equation for charged particle interacting with magnetized plasmas [76]

$$-\frac{d}{dE}[\alpha E N(E)] - \frac{N(E)}{\tau_{\text{esc}}} = 0 \tag{3.2}$$

where α indicates the average fraction of energy increases ($\frac{dE}{dt} = \alpha E$) and $N(E)$ is number of particles with energy E. Solving this equation will give a power law solution

$$N(E) \propto E^{-x} \tag{3.3}$$

where $x = 1 + (\alpha\tau_{\text{esc}})^{-1}$, with α and τ_{esc} being model-dependent constants.

This solution, however, does not provide sufficient energy gains to account for the UHECRs due to several reasons including the relatively small random velocities of the magnetic fields ($\frac{V}{c} \leq 10^{-4}$) and low rate of collisions on the astrophysical scale (a few times per year). It also cannot answer the question why the observed energy spectra for all particles as shown in Figure 3.1 are

so similar. Developments of the particle acceleration mechanism in the late 1970's had found a similar energy gain process which is to the first order of the magnetic cloud velocity ($\frac{dE}{dt} \propto \frac{V}{c}$) and automatically results in a power law spectrum with the spectral index $x \simeq 2$ [76]. Unlike the second order Fermi acceleration which only examines the systematic behaviors of the particles after the chain of collisions is finished, in this developed process each individual collision is scrutinized. Denote the average energy of the particle after each collision to be $E = \beta E_0$, and P being the probability that the particle is retained in the acceleration site after one collision. Then, there are $N = N_0 P^k$ particles with energy $E = E_0 \beta^k$ after k collisions. Eliminating k in both equations gives

$$\frac{\ln(N/N_0)}{\ln(E/E_0)} = \frac{\ln P}{\ln \beta} \tag{3.4}$$

which yields the form

$$\frac{N}{N_0} = (\frac{E}{E_0})^{\ln P/\ln \beta} \tag{3.5}$$

and the solution is a power law

$$N(E)dE \propto E^{-1+(\ln P/\ln \beta)} dE \tag{3.6}$$

This is equivalent to the second order Fermi acceleration if $(\ln P/\ln \beta) \equiv -(\alpha \tau_{esc})^{-1}$. This process is often referred as the first order Fermi acceleration as the accelerated particle energy increases $\propto (\frac{V}{c})$. Evaluating the behavior of individual particles in a strong shock wave propagating through a diffuse medium such as an interstellar medium yields quantitative results for P and β to be [77]

$$\frac{\ln P}{\ln \beta} = -1 \tag{3.7}$$

This results in the famous E^{-2} differential spectrum of the high energy particles

$$N(E)dE \propto E^{-2} dE \tag{3.8}$$

The maximum energy a charged particle can reach in an acceleration site is determined by the strength of the magnetic field and the size of the acceleration region as derived by Hillas [78]

$$E_{\text{max}}^{18} = \beta_s \cdot Z \cdot B_{\mu G} \cdot R_{\text{kpc}} \tag{3.9}$$

where $E_{\text{max}}^{18} \equiv \frac{E_{\text{max}}}{10^{18} eV}$ is the maximum energy that can be achieved, $\beta_s = \frac{V_s}{c}$ is the shock velocity relative to light speed, Z is the charge of the particle in units of e, $B_{\mu G} \equiv \frac{B}{1 \mu G}$ is the magnetic field strength in units of 1 μG, and $R_{\text{kpc}} = \frac{R}{1\text{kpc}}$ is the size of the acceleration region in units of 1 kpc.

3.2 Astrophysical Neutrinos

High energy neutrinos are expected to be produced in astrophysical shock fronts via proton-photon interactions and/or proton-proton collisions at cosmic ray acceleration sites. Neutrinos should be produced via the following interactions of cosmic ray protons [66, 79]:

$$\text{Photohadronic:} \quad p + \gamma \rightarrow \Delta^+ \rightarrow \begin{cases} p + \pi^0 \ (66.7\%) \\ n + \pi^+ \ (33.3\%) \end{cases} \tag{3.10}$$

$$\text{Hadronic:} \quad p + p \rightarrow \begin{cases} p + p + \pi^0 \ (66.7\%) \\ p + n + \pi^+ \ (33.3\%) \end{cases} \tag{3.11}$$

If the incident particle is a neutron instead of a proton, π^- will be produced in these processes. The charged pions will decay in subsequent reaction chains, producing neutrinos

$$\pi^+ \rightarrow \nu_\mu + \mu^+ \rightarrow e^+ + \nu_e + \bar{\nu}_\mu + \nu_\mu \tag{3.12}$$

$$\pi^- \rightarrow \bar{\nu}_\mu + \mu^- \rightarrow e^- + \bar{\nu}_e + \nu_\mu + \bar{\nu}_\mu \tag{3.13}$$

3.2.1 Source Candidates and Energy Spectrum of Astrophysical Neutrinos

Astrophysical neutrino production in galactic and extragalactic sources is thought to be due to hadronic and/or photohadronic processes. The only difference between galactic neutrinos and extragalactic neutrinos is closely related to the energy thresholds of the primary cosmic rays that the acceleration sites can reach. Based on the discussions made in Section 3.1.4, the maximum energy a proton can reach from being accelerated in galactic sources is $< 10^{19}$ eV. Therefore the highest energy neutrinos produced in local galactic sources can reach $\sim$ 100 TeV [80].

Possible galactic sources of high energy neutrinos are supernovae explosions, supernovae remnants, microquasars, soft gamma repeaters and anomalous X-ray pulsars, molecular clouds and diffuse TeV emission [66]. All these sources have either strong plasma environments present such as supernovae explosions or new supernovae remnants which are known to be ideal acceleration sites for charged particles, or are associated with extreme phenomena such as TeV gamma ray emissions which can be related to the photohadronic production of π^0.

The highest energy astrophysical neutrinos ($>$100 TeV) have to originate from extragalactic sources such as AGNs and GRBs which are expected to be the acceleration sites for the highest energy cosmic rays. If the cosmic rays decay before interacting, the energy spectrum for such neutrinos would follow the energy spectrum of the primary UHECRs, which according to the first order Fermi acceleration mechanism would be a E^{-2}. Specific models of AGNs and GRBs predict harder or softer neutrino spectra with respect to the generic E^{-2} model, depending on the source environments and whether the cosmic rays interact and lose energy before decaying and producing neutrinos [66].

In AGN jets or GRBs, neutrinos are expected to be produced in the pγ or pp processes. Hence, the rate of UHECRs detected at Earth should help to constraint the neutrino fluxes produced at the UHECR acceleration sites. A diffuse astrophysical neutrino flux upper bound, based on the observed UHECR flux and assuming that UHECRs are produced in sources which are optically

thin to pγ interactions, is estimated to be [81]

$$E_\nu^2 \frac{dN_\nu}{dE_\nu} = 3.4 \times 10^{-8}\ \text{GeVcm}^{-2}\text{s}^{-1}\text{sr}^{-1} \tag{3.14}$$

for ν_μ and $\bar{\nu}_\mu$. This is called the Waxman-Bahcall upper bound. Figure 3.2 shows the predicted fluxes from various models of astrophysical neutrinos.

3.2.2 Coherence of Astrophysical Neutrino Oscillations and Flavor Ratios

The production of ν_τ from prompt decay of D_s and $B\bar{B}$ at the source is usually much below 1% of the ν_μ production [2]. Therefore, if the interaction of π^+ and μ^+ with the ambient material before decay is negligible, these chain reactions will lead to a neutrino flavor composition at source

$$(\nu_e^S + \bar{\nu}_e^S) : (\nu_\mu^S + \bar{\nu}_\mu^S) : (\nu_\tau^S + \bar{\nu}_\tau^S) \approx 1 : 2 : 0 \tag{3.15}$$

This flavor ratio holds for AGN models which predict neutrinos coming from photohadronic process $p + \gamma \to \pi + N$ [72, 2]. The 1:2:0 ratio at sources will result in a nearly 1:1:1 ratio at Earth assuming full mixing [2]. Interaction of π and μ with the source environment such as radiation and magnetic fields before decay could modify this ratio. Modifications as such are inevitably energy dependent, as the higher the energy of π and μ, the more likely they will interact before decaying. Since π has a shorter lifetime than μ, the probability for a μ to interact and undergo significant energy loss before decay is higher than that of a π. Therefore, one extreme is that at sufficiently high energies the neutrinos from μ decay will be largely suppressed and the neutrino ratio at source is modified to be $(0 : 1 : 0)^S$ [85]. Another extreme is only ν_e emission from neutron decay at the source, which results in a ratio of $(1 : 0 : 0)^S$ [86]. This scenario is true for neutron stars. Usually, the neutrino flavor composition at cosmic sources is a combination between these extremes, and is largely dependent on the source environment, the neutrino energy spectrum and the neutrino energy itself [87]. A detailed overview on neutrino flavor compostions at various cosmic sources is given in [88]. Based on the best global fit values of standard neutrino mixing parameters from [89], flavor ratios of $(0.6 : 1.3 : 1.1)$ and $(1.6 : 0.6 : 0.8)$ at Earth are expected for $(0 : 1 : 0)^S$ and

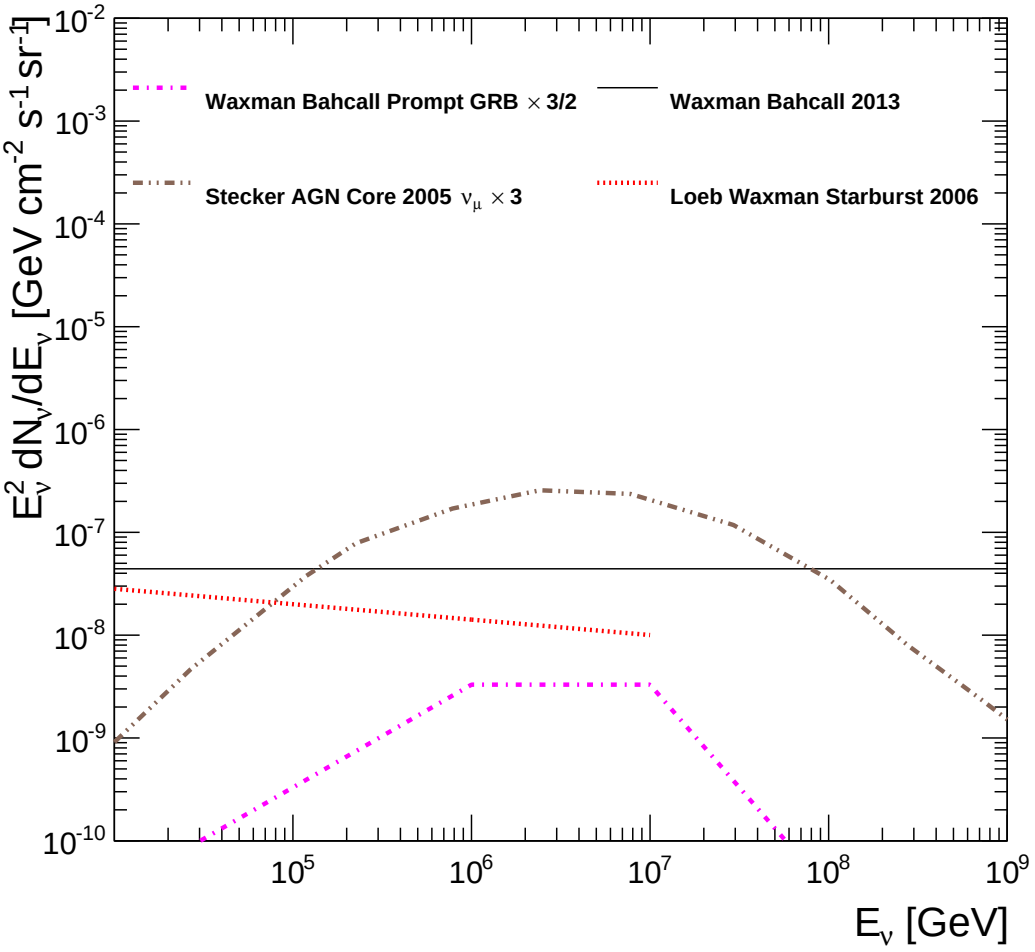

Figure 3.2: Neutrino fluxes from various models. The solid line is the Waxman-Bahcall upper bound which uses the UHECR flux to set a bound on astrophysical neutrino production [81]. The dash-dotted line is prompt neutrino flux predicted from GRBs; prompt in this context means in time with the gamma rays [82]. The dash-dot-dot line is neutrino flux predicted from the cores of active galaxies [83]. The dotted line is neutrino flux predicted from starburst galaxies, which are rich in supernovae [84].

$(1:0:0)^S$ scenarios respectively [90].

Neutrinos produced in exotic cosmic sources could lose coherence while traversing out from the sources and/or across astronomical distances. In the scenario of coherence loss, neutrinos don't oscillate anymore and hence could further modify the flavor composition seen at Earth which is

derived based on the standard oscillation assumption. In [43], extensive discussions on coherence and oscillations of cosmic neutrinos are addressed. Three main circumstances are considered: the interaction free environment (a good representation of cosmogenic neutrinos generated through cosmic rays interacting with galactic and intergalactic medium), the radiation-dominated environment (gamma ray bursts) and environment with magnetic fields. As discussed in Section 2.4.3, the size of a neutrino wavepacket σ_x is essential in determining its coherence conditions in various environments. For a source of baseline (distance from source to detector at Earth) L=100 Mpc, E_ν=10 TeV and Δm^2=Δm^2_{atm} = 2.5 $\times$ 10^{-3} eV^2, the coherence loss condition is [43]

$$\sigma_x \ll d_L = 3 \times 10^{-3} \text{ cm } \left(\frac{L}{100 \text{ Mpc}}\right) \left(\frac{\Delta m^2}{2.5 \cdot 10^{-3} \text{ eV}^2}\right) \left(\frac{10 \text{ TeV}}{E_\nu}\right)^2 \tag{3.16}$$

In an interaction free environment,

$$\frac{d_L}{\sigma_x} \sim 0.1 \left(\frac{L}{100 \text{ Mpc}}\right) \left(\frac{\Delta m^2}{8 \cdot 10^{-5} \text{ eV}^2}\right) \left(\frac{10 \text{ TeV}}{E_\nu}\right) \left(\frac{3 \times 10^{-8} \text{ sec}}{\tau_0}\right) \tag{3.17}$$

Where τ_0 is the lifetime of the parent particle (pion or muon). Equation 3.17 is generally much less than unity, which indicates coherence is preserved.

In a radiation dominated environment where parent particles interact with the medium, the neutrino wavepacket length is shorter than that in the interaction free environment. The kinematics of pion and muon decay - the former a two body decay and latter three body decay - also play an important role in deciding the wavepacket length of their product neutrinos. The neutrino wavepacket length from pion decay in the observer frame is

$$\sigma_{x,\pi} \sim 3 \times 10^{-5} \text{ cm } \left(\frac{10 \text{ TeV}}{E_\nu}\right)^2 \left(\frac{4 \text{ KeV}}{T_\gamma}\right)^3 \left(\frac{\Gamma_{jet}}{100}\right) \tag{3.18}$$

And the neutrino wavepacket length from muon decay in the observer frame is

$$\sigma_{x,\mu} \sim 5 \times 10^{-3} \text{ cm } \left(\frac{10 \text{ TeV}}{E_\nu}\right)^4 \left(\frac{4 \text{ KeV}}{T_\gamma}\right)^5 \left(\frac{\Gamma_{jet}}{100}\right)^3 \tag{3.19}$$

With T_γ being the photon temperature (typically $\sim$ few keV) and Γ_{jet} the Lorentz boost factor ($\sim$

100). Compared to Equation 3.16, neutrinos produced from muon decay usually maintain their coherence, while neutrinos from pion decay suffer coherence loss.

When magnetic fields are present (which are common in AGN and GRB jets), the neutrino wavepacket from pion decay in the observer frame is

$$\sigma_{x,\pi} \sim 2 \times 10^{-14} \text{ cm } \left(\frac{\Gamma_{jet}}{100}\frac{10^7 \text{ Gauss}}{B}\right)^{1/2} \left(\frac{10 \text{ TeV}}{E_\mu}\right)^{3/2} \tag{3.20}$$

Coherence is lost for these neutrinos over cosmological distance when the magnetic field satisfies

$$B \gg 5 \times 10^{-13} \text{ Gauss } \left(\frac{8 \times 10^{-5} \text{ eV}^2}{\Delta m^2}\right)^2 \left(\frac{100 \text{ Mpc}}{L}\right)^2 \frac{E_\nu}{10 \text{ TeV}} \frac{\Gamma_{jet}}{100} \tag{3.21}$$

And the neutrino wavepacket from muon decay in the observer frame is

$$\sigma_{x,\mu} \sim 5 \times 10^{-11} \text{ cm } \left(\frac{\Gamma_{jet}}{100}\right) \left(\frac{10^7 \text{ Gauss}}{B}\right) \left(\frac{10 \text{ TeV}}{E_\mu}\right)^2 \tag{3.22}$$

Complete loss of coherence in this case occurs when magnetic field meet the following condition

$$B \gg 10 \text{ Gauss } \left(\frac{8 \times 10^{-5} \text{ eV}^2}{\Delta m^2}\right) \left(\frac{100 \text{ Mpc}}{L}\right) \frac{\Gamma_{jet}}{100} \tag{3.23}$$

Therefore, for neutrinos from pion decay, coherence is lost with even relatively small magnetic fields present. While for neutrinos from muon decay, coherence could be maintained in magnetic fileds with moderate strength. With very strong magnetic fields which could be up to 10^9 Gauss in some GRB sources [91, 92, 93], neutrino coherence is entirely lost.

The decoherence of astrophysical neutrinos will distort the neutrino energy spectrum observed at Earth, as will other exotic processes such as neutrino decay [94], sterile neutrinos [95], pseudo-Dirac neutrinos [96] and Lorentz or CPT violation [97]. Based on standard oscillation, even assuming a large amount of ν_τ production at the sources will result in a nearly 1:1:1 ratio at Earth [90]. This is due to the values of the mixing angles $\theta_{23} \sim \frac{\pi}{4}$ and $\theta_{13} \sim 0$, which result in only a small contribution from ν_τ at the source to the flavor ratio after mixing. Therefore, observation of

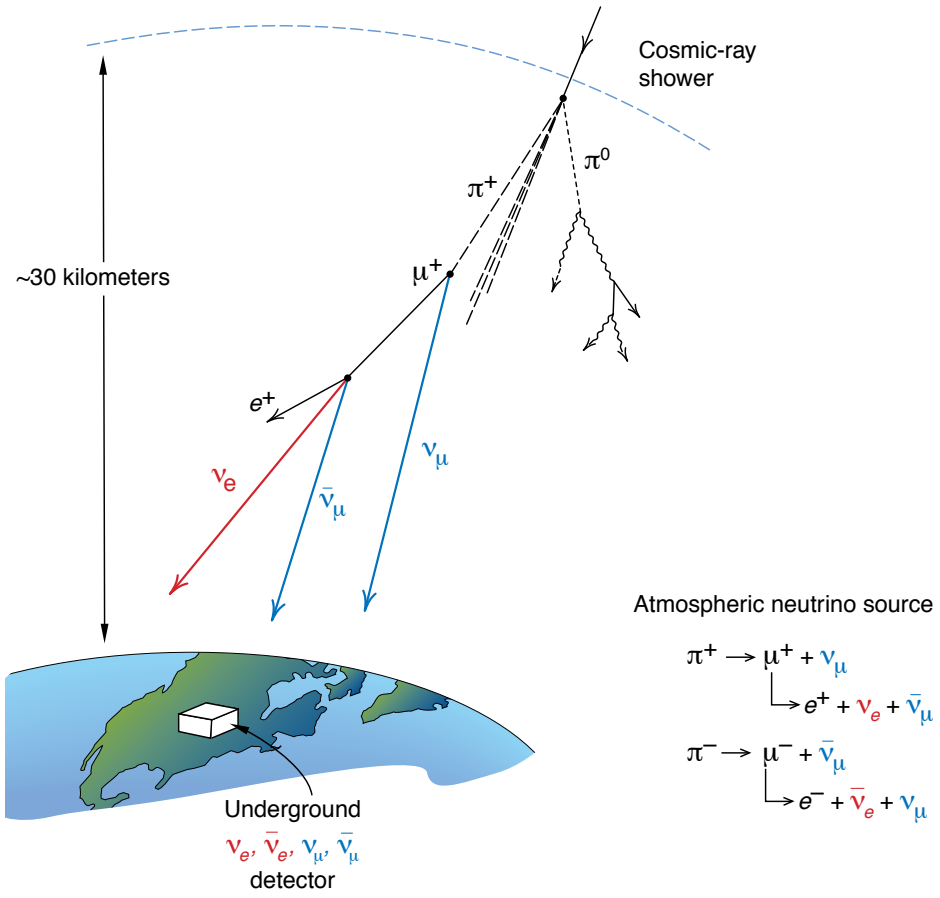

Figure 3.3: Atmospheric neutrino production chain in the atmosphere. Cosmic rays striking the atmosphere produce pions and other mesons, whose decay chain produce muons, electrons and neutrinos. This figure is taken from [21].

significant deviation from the 1:1:1 ratio of the astrophysical neutrino flavors at Earth would signal new physics.

3.3 Atmospheric Neutrinos

3.3.1 Conventional Atmospheric Neutrino Flux

The main background for astrophysical neutrino searches is the cosmic ray induced atmospheric muons (discussed in Chapter 5) and neutrinos. Figure 3.3 demonstrates the neutrino production chain occurring in the atmosphere.

Up to 100 GeV, decay of charged pions is the dominant atmospheric neutrino source. Above 100 GeV, decay of kaons becomes the dominant source. Models of atmospheric neutrino flux from pion and kaon decays are usually referred to as "conventional" models. Neutrino fluxes predicted from these models [98, 99, 100] are called *conventional fluxes*.

In the charged pion dominated regime, if both the pion and muon decay before reaching the earth, every decay chain of a π^+ will produce two muon neutrinos (one ν_μ plus one $\bar{\nu}_\mu$) and one electron neutrino, as is illustrated in Figure 3.3. Because the primary cosmic ray energy spectrum is $E^{-2.7}$, the pions and muons have relatively long mean life time of 2.6×10^{-8} s and 2.2×10^{-6} s respectively [29], and could interact with the ambient medium before decaying and producing neutrinos, which softens the neutrino energy spectrum to $\sim$E$^{-3.7}$. As energy rises above 100 GeV, kaons decay to ν_μ ($\bar{\nu}_\mu$) and ν_e ($\bar{\nu}_e$) through multiple decay channels with various branching ratios, as shown in Figure 3.5. Therefore, ratio of ν_μ to ν_e is about 2:1 at lower energies, and with a smaller fraction of ν_e at higher energies where kaon decay dominates the neutrino flux. Neutrino-producing meson decay chains are summarized as follows [101]:

$$
\begin{aligned}
\pi^{\pm} &\rightarrow \mu^{\pm} + \nu_{\mu}(\bar{\nu}_{\mu}) \quad (100\%), \\
\mu^{\pm} &\rightarrow e^{\pm} + \nu_{e}(\bar{\nu}_{e}) + \bar{\nu}_{\mu}(\nu_{\mu}) \quad (100\%), \\
K^{\pm} &\rightarrow \mu^{\pm} + \nu_{\mu}(\bar{\nu}_{\mu}) \quad (63.5\%) \\
&\rightarrow \pi^{\pm} + \pi^{0} \quad (21.2\%) \\
&\rightarrow \pi^{\pm} + \pi^{+} + \pi^{-} \quad (5.6\%) \\
&\rightarrow \pi^{0} + \mu^{\pm} + \nu_{\mu}(\bar{\nu}_{\mu}) \quad (3.2\%) \quad (K_{3\mu\nu}) \\
&\rightarrow \pi^{0} + e^{\pm} + \nu_{e}(\bar{\nu}_{e}) \quad (4.8\%) \quad (K_{3e\nu}) \\
&\rightarrow \pi^{\pm} + \pi^{0} + \pi^{0} \quad (1.73\%), \\
K_{S}^{0} &\rightarrow \pi^{+} + \pi^{-} \quad (68.6\%), \\
K_{L}^{0} &\rightarrow \pi^{+} + \pi^{-} + \pi^{0} \quad (12.37\%) \\
&\rightarrow \pi^{\pm} + \mu^{\mp} + \nu_{\mu}(\bar{\nu}_{\mu}) \quad (27\%) \quad (K_{3\mu\nu}) \\
&\rightarrow \pi^{\pm} + e^{\mp} + \nu_{e}(\bar{\nu}_{e}) \quad (38.6\%) \quad (K_{3e\nu}).
\end{aligned}
$$

Figure 3.4 from [100] compares conventional atmospheric neutrino fluxes predicted by Fluka [102], Bartol [98], HKKM04 [99] and results from Honda2006 [100]. Experimental measurements are roughly consistent with these conventional flux predictions up to 100 TeV [103]. Figure 3.5 shows experimental measurements of atmospheric neutrino fluxes.

3.3.2 Prompt Atmospheric Neutrino Flux

At even higher energies, heavy particles with charm (D and $\bar{D}$) and bottom content would be produced in the cosmic ray interactions in the atmosphere. The short lifetime ($\sim 10^{-12}$ s) of the charmed particles causes them to decay before interacting up to 10^{9} GeV [66], producing neutrinos promptly. Those neutrinos are therefore called *prompt neutrinos*, and they follow the energy spectrum of the primary cosmic rays $\propto E^{-2.7}$. The prompt flux dominates over the conventional flux beyond around 100 TeV, with ν_{μ} and ν_{e} produced in equal amounts [104].

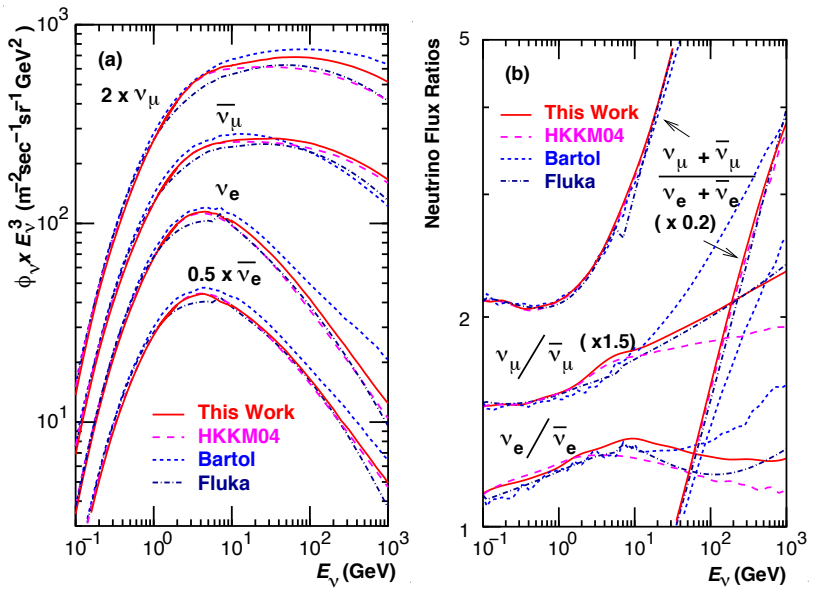

Figure 3.4: Comparison of atmospheric neutrino fluxes predicted by models [102, 98, 99, 100]. Fluxes are averaged over all direction: a) absolute value of atmospheric ν_μ and ν_e fluxes, b) ratio of ν_μ and ν_e fluxes. This figure is taken from [100].

A small component of ν_τ can be produced from the charm production via D_s decay to ν_τ. The fluxes for prompt ν_τ production are generally predicted to be at least an order of magnitude lower than that for prompt ν_μ and ν_e. Figure 3.6 shows the predicted fluxes for prompt neutrinos [104]. It should be noted that the prompt atmospheric neutrino flux has not yet been observed, even by IceCube or by any other experiment .

3.4 Existing Astrophysical Neutrino Experiments

The only extraterrestrial objects to have been observed in neutrinos are the Sun and Supernova 1987a (SN 1987A). The Sun produces neutrinos as a result of nuclear fusion in its core, whereby the sun generates its energy. Solar neutrinos have energies on the order of 1 MeV and have been observed in experiments such as Homestake [105], GALLEX [106], SAGE [107], Kamiokande/Super-Kamiokande [108, 109], SNO [110], KamLAND [28] and Borexino [111].

In a type II core-collapse supernova, electron neutrinos are produced through inverse beta decay (electron capture) when the stellar equilibrium between degeneracy pressure of the electrons and

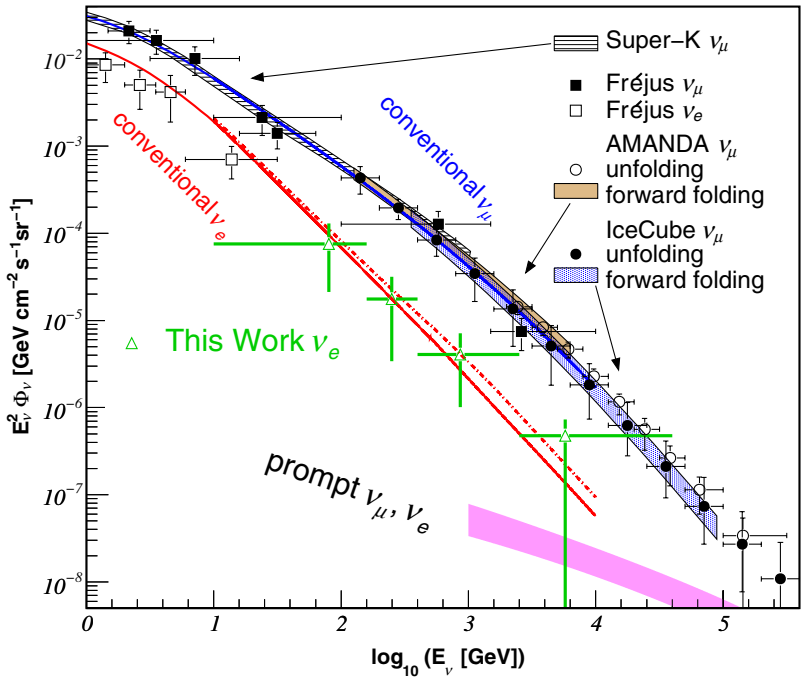

Figure 3.5: Measurement of atmospheric neutrino fluxes from various experiments: blue indicates the conventional atmospheric muon neutrinos and red indicates the conventional electron neutrinos, pink is the expected prompt atmospheric neutrino flux which is as yet unobserved. Plot is taken from [103], the green crosses refer to the atmospheric ν_e flux measurement done by IceCube.

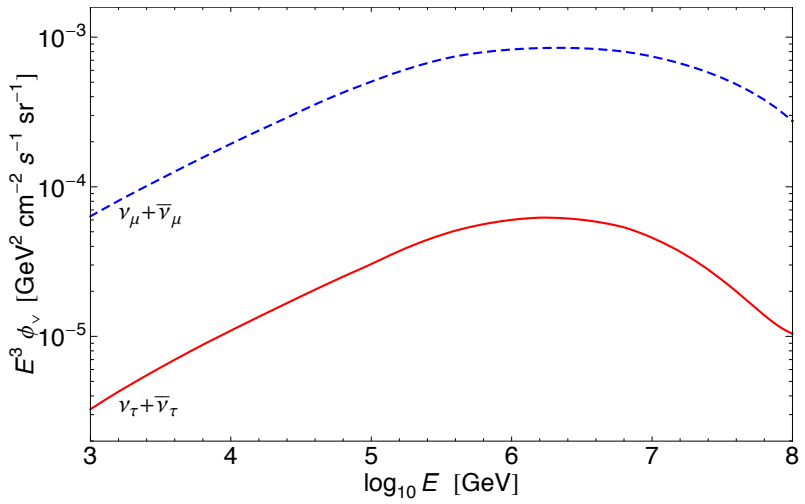

Figure 3.6: Atmospheric prompt ν_τ flux in comparison to the prompt ν_μ flux (the prompt ν_e flux is the same as ν_μ). The B-meson decay to ν_τ is not accounted for in this plot, which could add 10%-20% to the prompt ν_τ flux [104]. This figure is taken from [104].

gravity is broken. Furthermore, neutrino-antineutrino pairs are produced as the binding energy of the star is lost. In 1987, such neutrinos were observed by three neutrino detectors three hours prior to the optical detection of the supernova SN 1987A which occurred in the outskirts of the Tarantula Nebula in the Large Magellanic Cloud, 168,000 light years away. A total of 24 $\bar{\nu}_e$ were detected with 11 from Kamiokande-II [112], 8 from IMB [113] and 5 from Baksan [114, 115]. This detection made SN 1987A the first observed astrophysical neutrino source and marked the dawn of neutrino astronomy.

Since the predicted fluxes for astrophysical neutrinos are low and the neutrino-nucleon cross sections are small (more details on this in Chapter 5), the corresponding detectors are required to have a large instrumented volume for the rare astrophysical neutrinos to interact with. The interaction medium is also expected to be transparent to the neutrino-induced Cherenkov light so that the resulting photons can be detected by nearby photon sensors.

Water and ice are excellent media for Cherenkov light at the optical and UV wavelengths. The DUMAND[1] project was the very first under sea high energy neutrino detector, located in the Pacific Ocean off Keahole Point on the Big Island of Hawaii. It existed from 1976 to 1995, and was decommissioned due to short circuits failure [116]. The first successfully functioning underwater neutrino detector was BAIKAL, which detects atmospheric muons and neutrino-induced cascades in Lake Baikal in Russia with strings of PMTs deployed to a depth of 1100 m. The total instrumented volume of water is ~ 0.005 km^3. In continuous operation since 1998, BAIKAL's sensitivity to an astrophysical diffuse flux for all three neutrino flavors is $\sim 2 \times 10^{-7}$ GeV cm^{-2} s^{-1} sr^{-1} [117]. The ANTARES[2] experiment in the Mediterranean Sea consists of 12 strings of PMTs deployed to a depth of $\sim$2500 m encompassing a volume of $\sim$ 0.03 km^3 [118]. The sensitivity of ANTARES is 5.3×10^{-8} GeV cm^{-2} s^{-1} sr^{-1} [119]. Along with the ANTARES experiment, the NEMO[3] [120] and NESTOR[4] [121] experiments were built near the coasts of Italy and Greece respectively to explore different sites and techniques for neutrino detection in the deep ocean so that the location choice and detector design are optimal for the planned successor KM3NeT, which

[1]Deep Underwater Muon and Neutrino Detection
[2]Astronomy with a Neutrino Telescope and Abyss environmental RESearch
[3]NEutrino Mediterranean Observatory
[4]Neutrino Extended Submarine Telescope with Oceanographic Research

will instrument a water volume exceeding 1 km^3 [122].

AMANDA[5] was proposed in the mid 90's and constructed from 1996 to 2000 with a total of 677 photon sensors buried in the ice at the South Pole, instrumenting $\sim$0.016 km^3. The sensitivity for AMANDA was $\sim 3 \times 10^{-8}$ GeV cm^{-2} s^{-1} sr^{-1} [123]. AMANDA demonstrated that the Antarctic ice was transparent to optical light and that a detector could function over many years in the ice. AMANDA was decommissioned in 2009, and succeeded by the currently operating IceCube Neutrino Observatory which is elaborated in Chapter 4. Instrumenting a cubic kilometer of Antarctic glacial ice at the geographic South Pole, IceCube is also the world's largest neutrino detector to date. IceCube was designed to be the first detector with sensitivity exceeding the Waxman-Bahcall bound and is most sensitive in the TeV-PeV energy range.

A proposed source of extremely high energy neutrinos above energies of 10^{18} eV is the GZK effect, whereby neutrinos are produced during cosmic ray interactions with the cosmic microwave background [124, 125, 126, 127], as discussed in Section 3.1.3. GZK neutrino detectors must instrument even larger volumes than IceCube, due to the extremely low fluxes of neutrinos predicted at energies above 1 EeV. Such detectors currently rely on the Askaryan effect [128, 129], whereby coherent radio emission is produced in EeV neutrino interactions. In media such as ice, rock salt and the lunar regolith, radio waves have a much longer attenuation length than optical radiation, allowing more sparse instrumentation and larger detectors. The Askaryan effect has been demonstrated in sand [130], salt [131] and ice [132] at SLAC beam tests. Detectors based on the Askaryan effect include GLUE (lunar regolith) [133], RICE (ice) [134], ANITA (ice) [135], AURA (ice) [136] and ARIANNA (ice) [137]. Test measurements have been made in rock salt as well.

This work discusses tau neutrinos specifically. Although cosmic ray air shower detectors are not designed to be sensitive to electron or muon neutrinos, which produce air showers very rarely, air shower arrays can detect air showers from tau neutrinos due to the mechanism of regeneration. In this mechanism, tau neutrinos which skim the Earth produce tau leptons inside the Earth, which then decay again and produce tau neutrinos of lower energy. Eventually, the exiting particles may

[5]Antarctic Muon And Neutrino Detector Array

produce an air shower from the side of a mountain [138]. Cosmic ray detectors such as Auger [139] search for showers from mountains which would be produced by tau neutrinos. The energy threshold for such a search is high ($\sim$ 1 EeV), and to date no such showers have been observed.

Chapter 4

The IceCube Detector

The IceCube neutrino detector is introduced in this chapter, beginning with the overall detector design. The photomultiplier tube (PMT) and the digital optical module (DOM) which is the fundamental unit of the IceCube sensors are described. Finally, the interaction medium, the South Pole glacial ice, is discussed. In Section 2, the data acquisition system of IceCube will be introduced. This includes the digitization of the waveforms and the triggering logic, local coincidence and transmission of data. In Section 3, geometry, time and DOM calibrations will be covered.

4.1 Detector Design

The IceCube neutrino detector is a cubic kilometer Cherenkov array located near the geographical south pole. Construction of the detector began in 2004 and was completed in December, 2010. IceCube is the world's largest neutrino detector to date. The full detector consists of 86 cables called "strings", each with 60 digital optical modules (DOM) deployed between 1450 m and 2450 m deep. The DOM consists of a photomultiplier tube (PMT) and digitizing electronics. Seen from overhead, the 86 strings form a hexagonal shape with length $\sim$1 km on each side, see Figure 4.1. Therefore the instrumented volume is $\sim$km^3. With such a large interaction volume, IceCube aims to detect very rare high energy neutrinos ($\sim O$(TeV)-O(PeV)) from astrophysical accelerators.

The IceTop array is a surface detector built for cosmic ray air shower detection. There are 81

IceTop stations on top of the IceCube strings; each of which has 2 tanks, containing two DOMs per tank. Using the correlation between cosmic ray showers and cosmic ray muons, IceTop can also be used as a veto for separating down-going muon events from neutrino interaction events in the ice.

At the center of the detector is a denser sub-array called the DeepCore detector. The 8 DeepCore strings are instrumented with high quantum efficiency (HQE) DOMs. The efficiency of the HQE DOMs is $\sim$1.35 times that of the standard IceCube DOMs. Unlike the uniform vertical spacing of DOMs on each standard IceCube string, DeepCore has 10 DOMs between the depths of 1750 m and 1850 m, and 50 DOMs between 2100 m and 2450 m with $\sim$7 m vertical spacing, forming two small sub-arrays. The top array acts as an active veto for the down-going muons. DeepCore was designed to detect lower energy neutrinos ($\sim O$(GeV)), in particular, neutrinos coming from the earth's atmosphere. Being surrounded by the standard IceCube strings enables DeepCore to veto a large fraction of the down-going muon background.

4.1.1 Photomultiplier Tubes (PMT)

PMTs are extremely sensitive and versatile detectors of light in the ultraviolet, visible, and near-infrared regions of the electromagnetic spectrum. Figure 4.2 is a schematic representation of a PMT. The fundamental sensor of a PMT is the photocathode which absorbs incident photons and translates them into photo-electrons through the photoelectric effect. The successive high-voltage charged dynodes receive the primary photoelectrons from the photocathode and produce a number of secondary photoelectrons associated with each impinging primary photoelectron. After several dynode transmissions, a final amplification/gain ($\sim 10^7$) is achieved in a sub-nanosecond time scale. The photo-electrons from the last dynode are collected by the anode and transform current to voltage that can be read out. The photocathode, dynodes and anode are housed in a high vacuum tube to obtain an extremely quiet environment. The high gain, ultra-fast response, low noise characteristics of PMTs are important in fields such as nuclear/particle physics and astronomy which requires precise identification of weak signals [140].

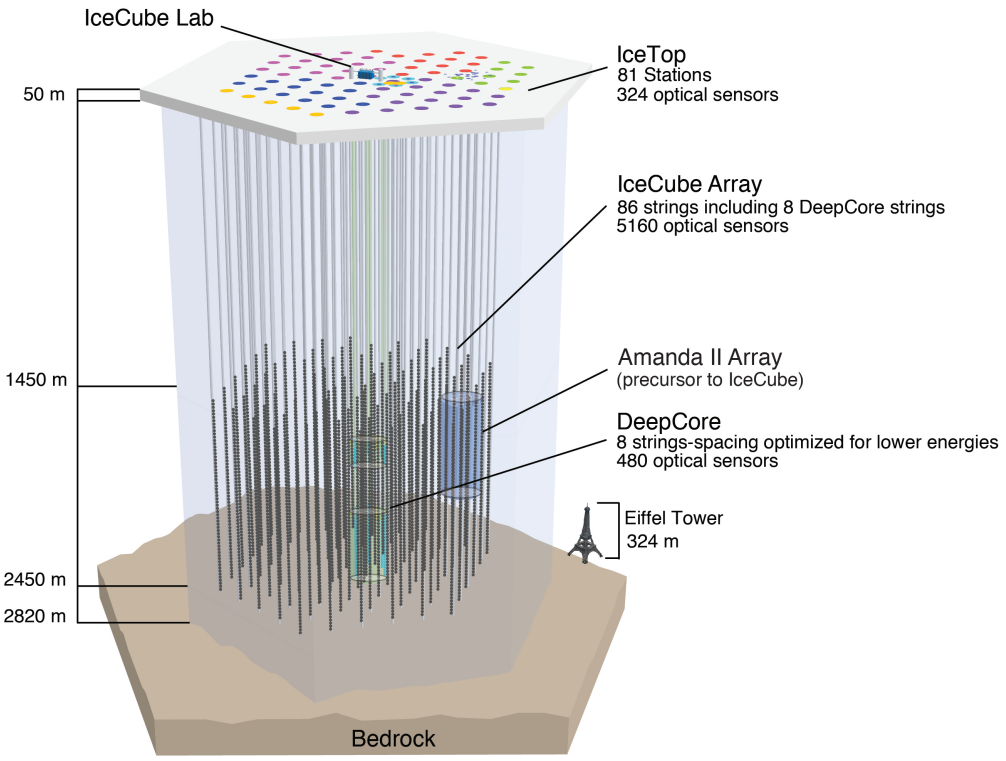

Figure 4.1: Viewing from top to bottom: the IceCube computer lab located at the center of the IceCube array at the glacial ice surface. Each color dot on the surface represents one string, the color codes indicate in which year the string was deployed, starting from 2005 and ending in 2010. The IceTop cosmic ray stations are located on top of the IceCube strings. There are 81 stations, each of which has 4 tanks. The black dots on each string from depth 1450m to 2450m are the digital optical modules (DOM), 60 DOMs per string on 86 strings. The green sub-array in the center of the detector is the denser DeepCore detector. The blue array is the IceCube predecessor, Amanda II, which was decommissioned in 2009. Figure is taken from the IceCube internal figure gallery: https://gallery.icecube.wisc.edu/internal/main.php.

IceCube uses the commercially available R7081-02 PMTs manufactured by Hamamatsu Photonics. These PMTs are selected because of their low dark noise and excellent timing and charge resolution for single photons. The dark noise rate was measured to be $\sim$300 Hz in the -40° C to -20° C temperature range when the PMT was operated with a discriminator threshold of 0.25 PE at gain of 10^7 [141]. The R7081-02 PMTs have a nominal gain of 10^7, with other lower gains available. The nominal gain used for the standard IceCube DOMs gives single photon pulses with amplitudes of $\sim$8 mV. The digitizer precision and other electronic noise, on the order of $\sim$0.1 mV,

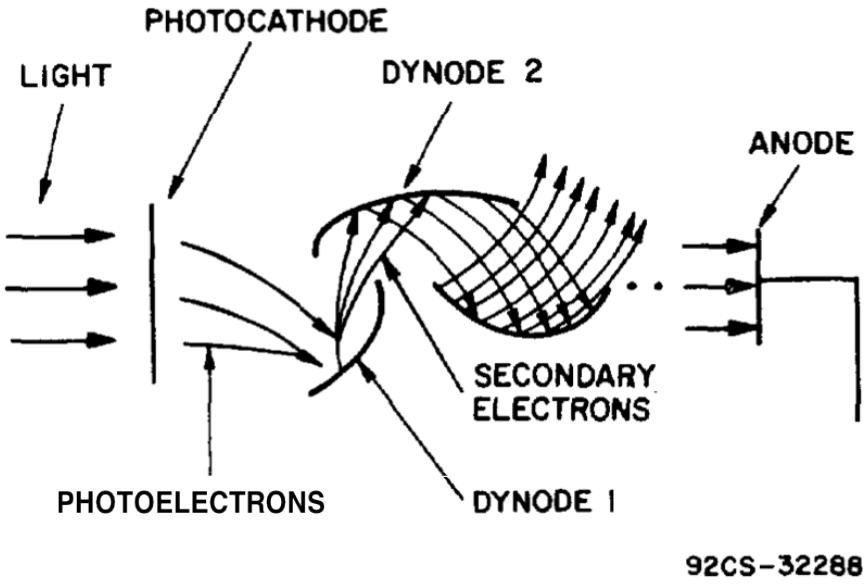

Figure 4.2: Schematic diagram of a PMT taken from [140].

are well below the single photon pulse amplitude. The large-area (25 cm in diameter) photocathode gives a peak quantum efficiency of $\sim$25% at 390 nm [141].

Additional sources of PMT pulses are prepulses, late pulses and afterpulses. Prepulses are caused by photons missing the photocathode and hit the dynode directly. For IceCube PMTs, the characteristic advance time for prepulsing measured in the lab is $\sim$31.8 ns for an HV setting of 1345 V (typical IceCube HV setting is 1500 V) and a PMT gain of 10^7. The advance time of prepulses scales as $(31.8 \text{ ns}) \times \sqrt{\frac{1345\ V}{supply\ voltage}}$. The average charge for a prepulse electron (PPE) is $\sim\frac{1}{15}$ PE, the relative quantum efficiency of a PPE relative to the quantum efficiency of a PE is $\sim$0.007. Figure 4.3 shows prepulses with respect to the main SPE pulses measured in the lab.

Late pulses are caused by photoelectrons backscattered from the first dynode elastically or inelastically. The overall probability of late pulses is $\sim$3.5%. Late pulses from elastic scattering have a narrow time distribution which centers at about two photoelectron transit lengths away from the on-time SPE peak. These pulses can be full amplitude. Late pulses from inelastic scattering have a broader smeared out time distribution, with smaller pulses which can persist and appear as multiple pulses distributed over the whole time range. Late pulses in IceCube PMTs can occur tens

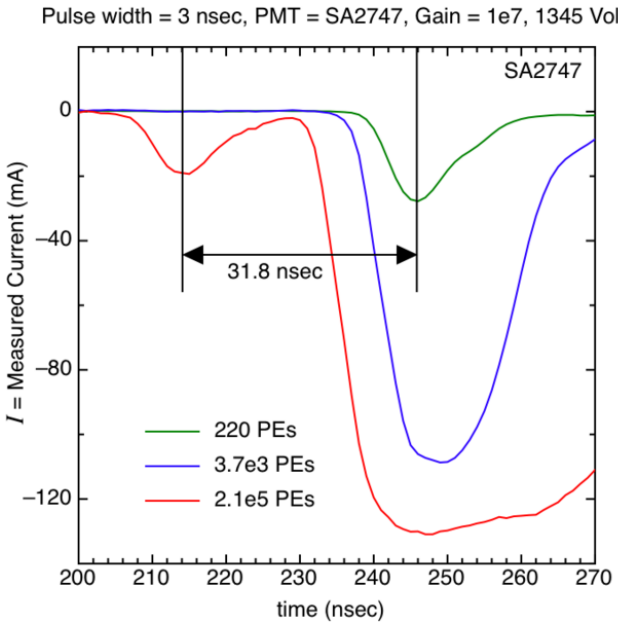

Figure 4.3: PMT prepulses measured in the lab, seen in the red curve which recorded 2.1×10^5 PE. This figure was taken from [142].

of nanoseconds later than the main on-time SPE peak.

Afterpulses occur when remnant atoms are ionized and accelerated in the phototube, creating pulses. Typical time scales for afterpulses range from 500 ns to microseconds later than the main on-time SPE pulse.

Figure 4.4 shows late pulses and afterpulses of IceCube PMTs measured in the lab. The late pulse distribution is fitted to a series of Fisher-Tippett distributions by Rodín Porrata [143], while the afterpulse distribution is fitted to a series of Gaussian components [144]. The resulting parameters from the fits are employed in the IceCube waveform simulations.

4.1.2 Digital Optical Module (DOM)

A DOM is the most basic unit of the IceCube detector. Major elements in a DOM consist of

- A Hamamatsu R7081-02 PMT
- A 2 kV high voltage (HV) generator which powers the PMT

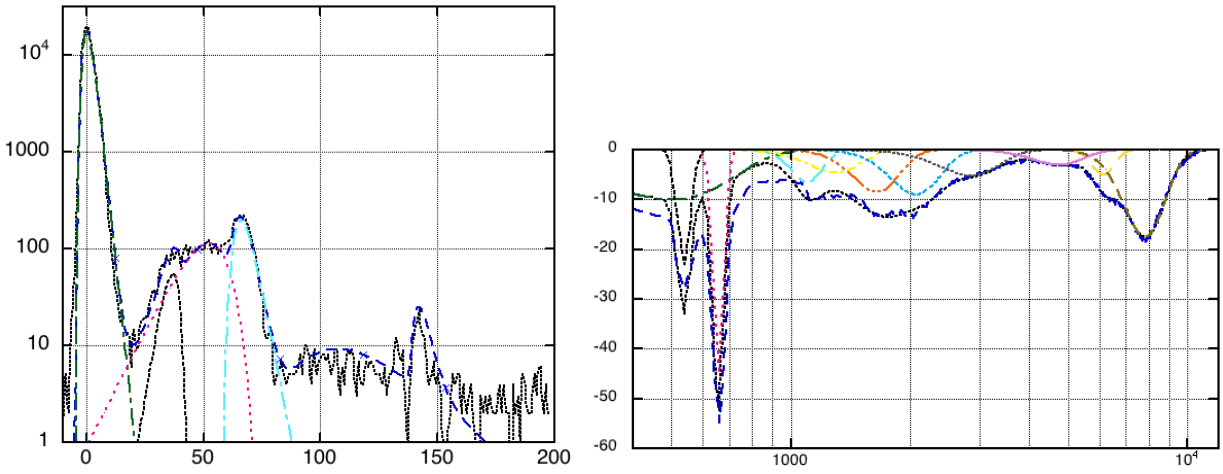

Figure 4.4: Left: late pulse time distribution measured in the lab with x-axis being time in units of ns, and y-axis being counts. Right: afterpulses measured in the lab with x-axis being time in units of ns, and y-axis being current in units of mA. These figures were taken from [143] and [144].

- The DOM Main Board (MB) which digitizes signals from the PMT and communicates with the surface
- The LED Flasher Board that consists of 12 405 nm LEDs uniformly distributed in azimuth (6 pointing horizontally and 6 tilted at a zenith angle of 45°)
- A stripline signal delay board that buffers the signals up to 75 ns

All these elements are enclosed in a 13 mm thick glass ($\sim$25 cm in diameter) sphere pressure vessel, capable of withstanding a pressure of 10000 psi, with flexible RTV gel to optically couple the glass sphere to the PMT's face. A mu-metal grid surrounds the PMT to shield it from Earth's magnetic field. To ensure mechanical integrity, the assembled DOM is filled with dry nitrogen to a pressure of $\sim\frac{1}{2}$ atm. A single twisted copper wire-pair running through the penetrator connects each DOM MB to a cable that runs up to the IceCube Laboratory (ICL) which is located at the surface of the ice and transmits buffered and packetized data on demand. Figure 4.5 demonstrates the key elements of a DOM [145].

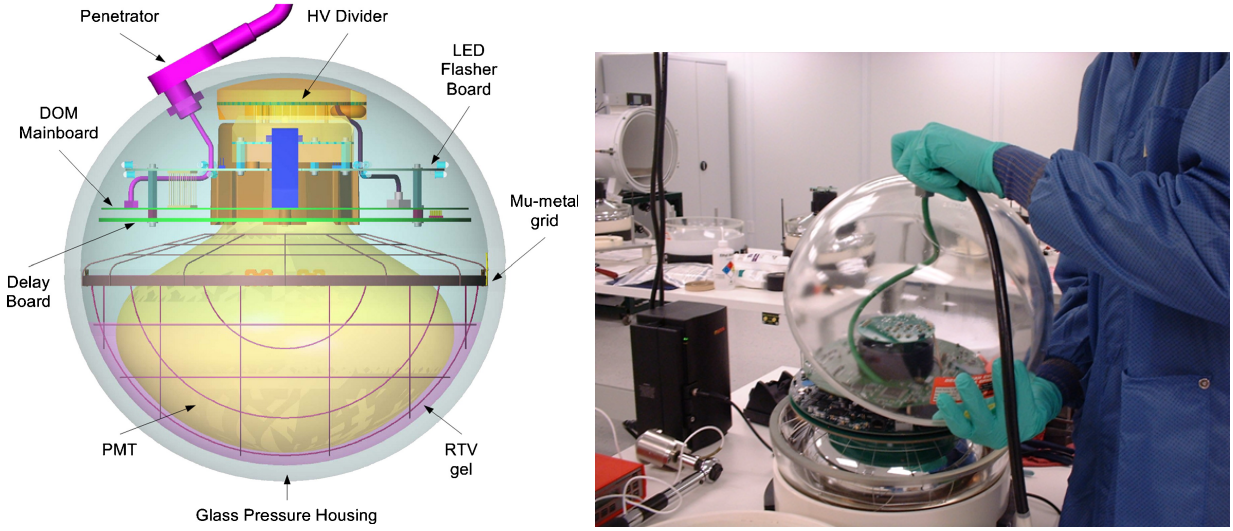

Figure 4.5: Left: Schematic representation of a DOM. Right: a DOM is being assembled in the lab.

4.1.3 Detection Medium: the South Pole Ice

Neutrino detection in IceCube is made possible through neutrino interactions with the glacial ice. The secondary particles produced during the interaction are extremely relativistic. They travel faster than the phase velocity of light in ice and emit Cherenkov radiation. Those Cherenkov photons propagate through the ice, undergoing complex scattering and absorption processes. Scattering of Cherenkov photons delays and hence distorts the timing information, while absorption of photons causes loss of energy information of an event. Photons are absorbed by electron or molecule excitations, and deflected by trapped air bubbles, dust particles and ice crystal defects. The combination of scattering and absorption effects from the ice contribute to the largest uncertainty in IceCube's neutrino searches. Therefore, it is of essential importance to understand the ice properties and account for them in the IceCube event simulation and reconstruction.

The $\sim$2600 meter thick Antarctic glacial ice sheet was formed from snow accumulation since $\sim$100,000 years ago. Ice at the depths between 1450 m and 2450 m, where the IceCube photon sensor array is located, accumulated about 60 to 70 thousand years ago. Figure 4.6 shows South Pole ice age as a function of depth.

The formation history of the glacial ice results in complex optical properties of the ice. Both scattering and absorption lengths are found to be depth dependent. Air bubbles trapped in ice

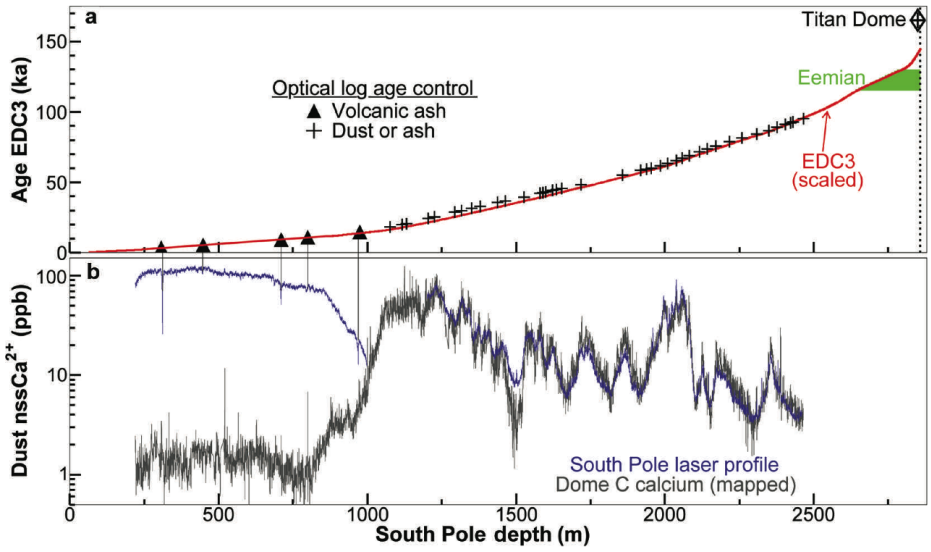

Figure 4.6: Top: South Pole ice age as a function of depth. Bottom: South Pole dust concentration as a function of depth. Figure is taken from [146].

decrease in size as a function of depth down to ∼1350 m. These trapped air bubbles turn into hydrates due to increasing pressure from accumulating snow exerted from above. At IceCube's instrumented depths, the hydrated air bubbles have almost the same refractive index as the ice. Bubble-free ice is the most transparent natural solid on earth in the ultraviolet to visible wavebands. Over the years, dust from volcanic eruptions has been preserved in the ice layers. The dust layers were studied with bore-hole logger data [146].

To study and model the South Pole ice, IceCube uses *in situ* light sources (lasers and on-board LEDs, a.k.a. flashers) to flash pulses of lights into the ice. Photons from each flashing travel in the ice and register at nearby DOMs. Ice properties such as scattering and absorption coefficients can be extracted from the flasher data given that both the emitted and received energies are known.

4.1.4 Modeling the South Pole Ice

Ice models used in IceCube data analyses are constructed phenomenologically. The current baseline ice model used in IceCube simulations is called the SpiceMie model [147]. Spice stands for South Pole Ice. Mie refers to the theory of electromagnetic radiation scattering off small particles

which was first treated by Gustav Mie [148]. In the Mie scattering model, the total effective length of light transport λ_e is given by

$$\lambda_e = \lambda_s \sum_{i=0}^{n} \langle \cos\theta \rangle^i \rightarrow \frac{\lambda_s}{1 - \langle \cos\theta \rangle} \tag{4.1}$$

where λ_s is the scattering mean free path (or geometric scattering length) which indicates the average distance between two scatters, θ is the deflected angle for a single scatter, and n is number of total scatters. The average cosine $\langle \cos\theta \rangle$ describes the nature of the scattering processes. For isotropic scattering processes, $\langle \cos\theta \rangle$ = 0. Photons undergoing scattering in the Antarctic ice are highly forward oriented with $\langle \cos\theta \rangle$ computed to be $\sim$0.9. The effective scattering coefficient $b_e = \frac{1}{\lambda_e}$ for light between 300 nm and 600 nm scattering off dust follows a power law dependence on the wavelength

$$b_e \propto \lambda^{-\alpha} \tag{4.2}$$

with $\alpha \sim$1 depending on the dust composition of the ice [149]. Photon absorption is characterized by the absorption length λ_a which is defined as the distance over which the photon density is reduced to $\frac{1}{e}$. The effective absorption coefficient a is the reciprocal of the absorption length, $a = \frac{1}{\lambda_a}$.

The Spice model uses a global fit to a collection of datasets from all flashers on string 63. The fitting procedure is done using the PPC (Photon Propagation Code [150]) program which simulates and traces every photon in ice. For every fitting point, a set of scattering and absorption parameters are optimized to best match the flasher data. These sets of optimized parameters are tabulated for later usage in event simulation and reconstruction. The baseline SpiceMie model assumes azimuthally isotropic South Pole ice. Further studies on recent IceCube flasher data indicate slight azimuthal dependence of ice optical properties. An updated version of the SpiceMie model accounting for the ice anisotropy was made in 2013, with the name SpiceLea [151]. Figure 4.7 shows South Pole ice optical properties from SpiceMie and SpiceLea models.

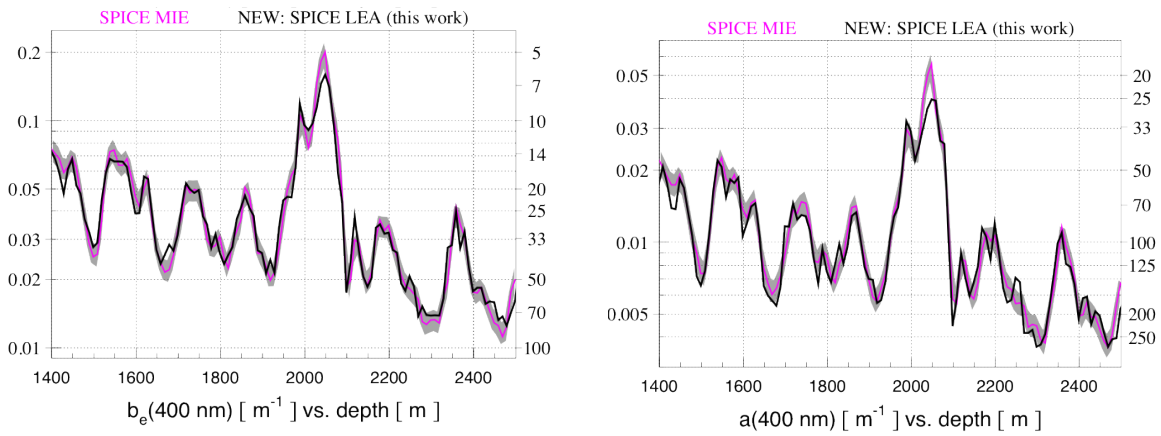

Figure 4.7: Left: scattering coefficient (reciprocal of scattering length) of the South Pole glacial ice as a function of depth, dark represents the SpiceLea model which includes angle-dependent ice anisotropy and pink represents the SpiceMie model. Right: absorption coefficient (reciprocal of absorption length) of the South Pole glacial ice as a function of depth, with the same color code as the scattering coefficient. Note that at depth $\sim$2050 m, there is a big dust layer which exhibits both higher scattering and absorption coefficients: photons are more likely to be scattered or absorbed at this layer. Figure is taken from [151].

4.2 Data Acquisition (DAQ)

To precisely capture and timestamp the complex and widely varying electrical signals read out from the PMTs, digitization of the signals is done individually inside each DOM through the waveform digitizers located on the DOM MB. The digitized signals are then collected through the copper wire-pairs (packed in a cable) which connects to the IceCube Laboratory (ICL) on the surface of the ice. Power is also supplied from ICL to each DOM through the cable network.

4.2.1 IceCube Waveforms

There are two types of digitizers on the DOM MB. One is the Analog Transient Waveform Digitizer (ATWD), and the other is the fast Analog to Digital Converter (fADC). There are two identical ATWDs on each DOM in order to minimize detector deadtime - when one is busy digitizing, the other continues to read.

The ATWD has an analog memory of 128 sampling capacitors. It samples at a configurable rate, currently configured to be 300 mega samples per second (MSPS) which is equivalent to 3.3

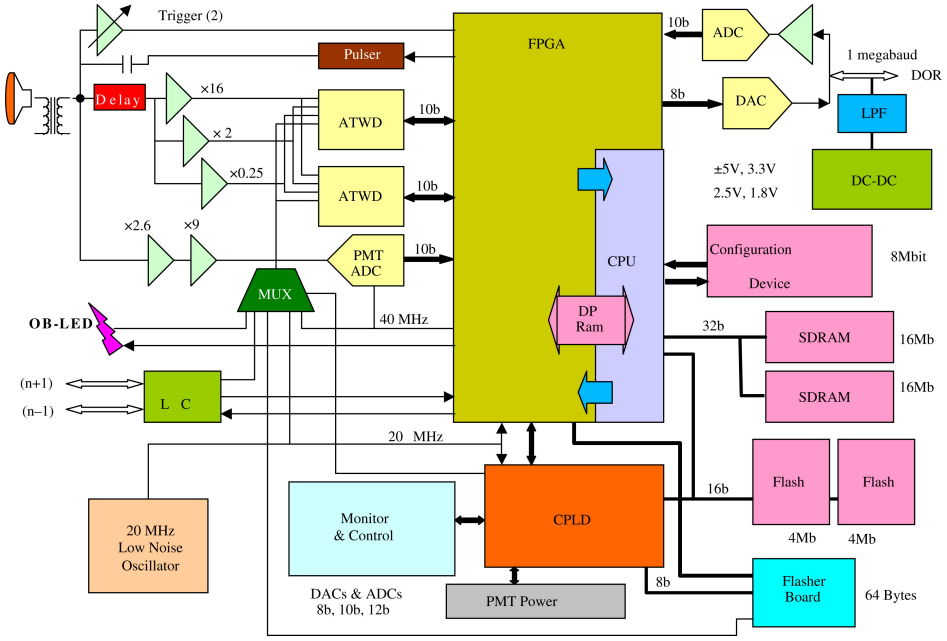

Figure 4.8: Digital circuit of a DOM MB. The adjustable threshold of the Trigger at the upper left of the circuit determines how big a signal can trigger the detector, the LC logic (described in later sections) decides if the captured ATWD samples should be transmitted to the surface. There are two ATWDs in the circuit, one acts as a backup digitizer to capture signals while the other one is busy. The Field Programmable Gate Array (FPGA) initiates the actual digitization, communicates with nearby DOMs and the surface. The CPU controls the FPGA, handles data transport, tests and monitors the system. Figure is taken from [152].

ns/sample. This allows the ATWDs' acquisition of 422 ns long waveforms. The fADC samples at a lower rate of 40 MSPS and the sampling time window is configured to be 6.4 μs, corresponding to 256 samples per acquisition.

Figure 4.8 illustrates that analog signal output from the PMT is split into three paths at the input to the DOM MB. The upper path is for trigger, the middle path is delayed for 75 ns by going through a delay line and then further split into three and amplified by three different levels ($\times$16, $\times$2, $\times$0.25) before inputting it to the three channels of the two ATWDs. The third path is amplified by $\times 2.6 \times 9$ and sent to the fADC so that information from longer physics signals is kept at a coarser rate [145, 152].

Figure 4.9 shows examples of a captured waveforms from the three ATWD channels and the fADC channel. The most sensitive ATWD channel 1 ($\times$16) is digitized first, the channel 2 ($\times$2)

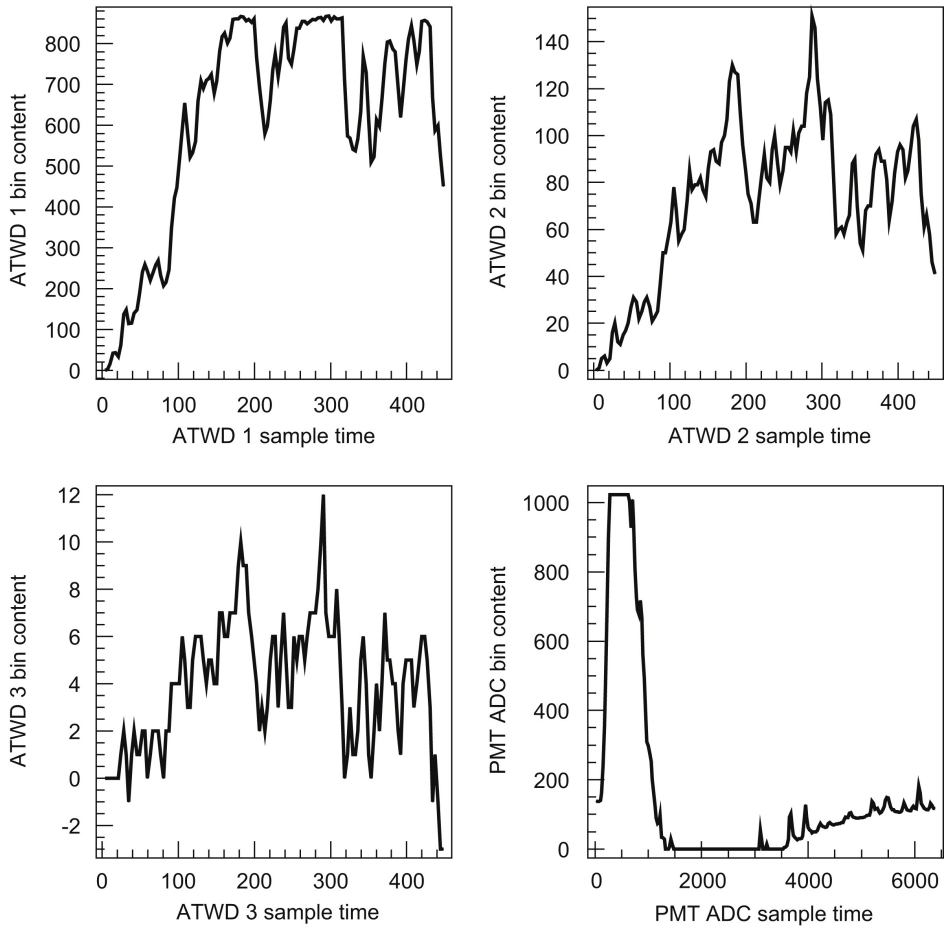

Figure 4.9: Waveform examples captured by the three ATWD gain channels and the fADC channel. Unit of the sample time is in ns. Figure is taken from [152].

will be digitized if any sample in channel 1 exceeds 768 counts. The third channel ($\times 0.25$) will be digitized if any sample in channel 2 exceeds 768 counts. This digitization scheme allows the ATWDs to cover the whole PMT dynamic range. The fADC is more susceptible to overflow than any of the ATWD channels due to its higher ($\times$ 23.4) amplification and resolution [152].

Figure 4.10 is an example of a digitized ATWD waveform from a single photoelectron (SPE).

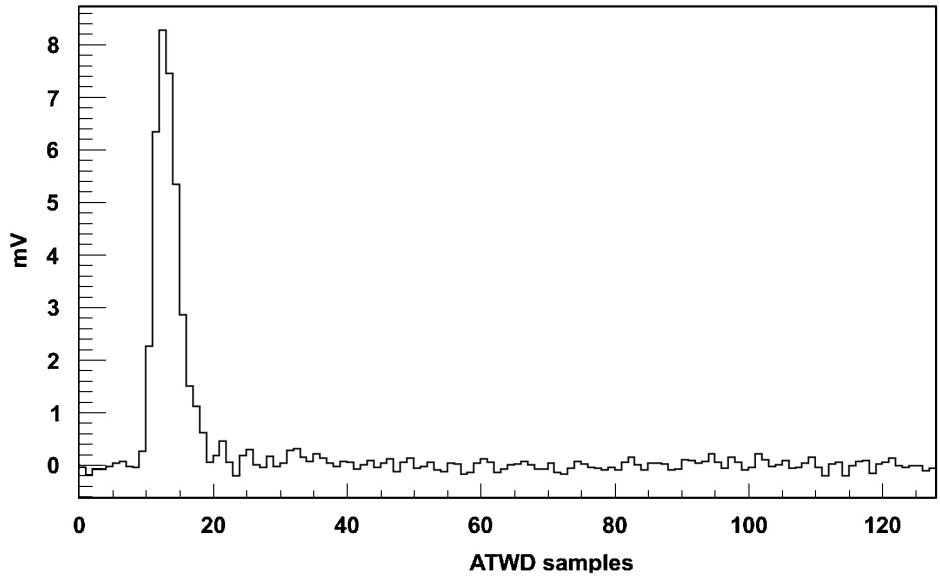

Figure 4.10: Digitized ATWD waveform from a single photoelectron. Figure is taken from [152].

4.2.2 The Hit

A hit is the most fundamental unit of IceCube data. A "hit" occurs whenever one or more photons are detected by a DOM crossing the discriminator threshold of 0.25 PE. A hit contains a timestamp generated locally at the DOM and digitized waveform information [152]. Depending on the complexity of the digitized waveforms, a hit size can range from 12 bytes to hundreds of bytes.

The concept of hits allows for limiting data flow sent to the surface either by 1) requiring neighboring channels to have coincident hits within a certain time window - as real physics hits tend to be coincident in spacetime, whereas random PMT noise hits are isolated, and by 2) minimizing the waveform information packetized in a hit.

4.2.3 Local Coincidence

Local coincidence (LC) logic is incorporated to limit data flow from DOMs to the surface due to limited capacity of the copper wire-pairs. LC is realized by DOMs connecting to neighbors above and beneath them through transceivers over the copper wire-pairs. Two LC modes are employed in IceCube signals. Hard Local Coincidence (HLC) requires nearest or next-to-nearest DOMs having

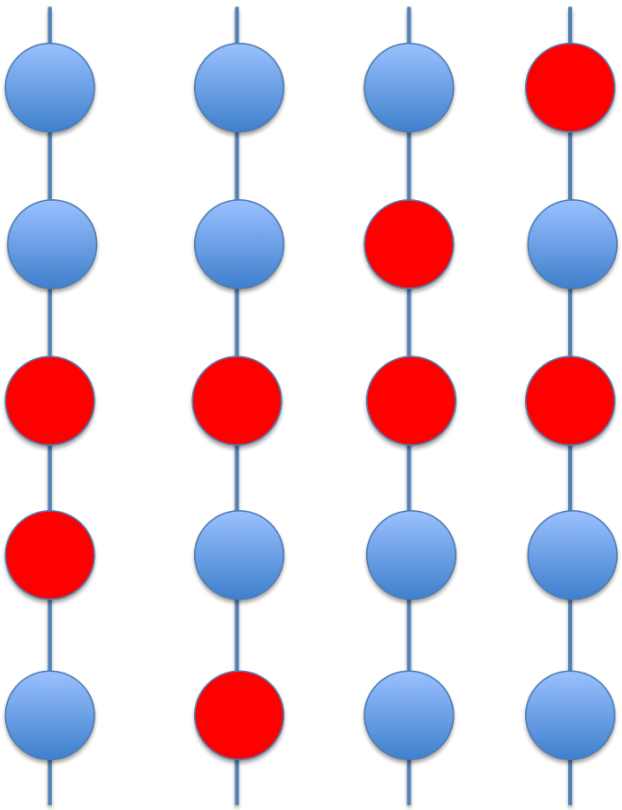

Figure 4.11: Schematic demonstration of local coincidence. Red circles represent hit DOMs, and blue circles represent unhit DOMs. LC conditions always occur between DOMs on the same string. There are four situations a LC condition would satisfy as illustrated on the four independent strings: the hit DOM pairs being nearest or next-to-nearest to each other.

hits within a time window of ± 1000 ns to send data up to the surface. Soft Local Coincidence (SLC) is the baseline operation mode. It does not require neighboring DOMs to have coincident hits, which results in about two orders of magnitude higher rates than the HLC mode. In SLC mode, only hits with the LC tag are sent up to the surface with full waveform information (ATWD and fADC); for isolated hits without LC tag, only a compressed digitization header which contains the highest fADC sample and its two nearest neighboring samples from the first 16 samples after the trigger will be sent up to the surface [152, 153]. Figure 4.11 illustrates LC conditions.

4.2.4 Triggering and Filtering

There are multiple triggering conditions in IceCube depending on the specific physics goals. A simple example is the Simple Multiplicity Trigger (SMT) which triggers the detector when the condition of a certain number of LC within a certain triggering time window is satisfied. For the data used in this work, the SMT8 trigger, which requires at least 8 LC hits to occur within a time window of 5 μs, is employed. The readout time window consists of the triggering time window plus 4 μs prior and 6 μs after the triggering time window. The global trigger window is the minimum time interval over which all readout windows for all satisfied triggers are encompassed (i.e. a logical OR of all triggers). All the recorded hits within a global trigger time window are packeted into an event and passed onto the processing and filtering (PnF) system at the South Pole, which will decide whether an event is interesting enough to be transmitted to the North via satellite for further analysis. Trigger rate in IceCube is $\sim$2.8 kHz, dominated by atmospheric muons. The allocated satellite bandwidth for IceCube is $O(100)$ GB per day, so only about one third of the triggered events will be transmitted through satellite. All events at trigger level are stored on tapes or disks.

IceCube uses a software framework called IceTray to process data. In IceTray, every event is represented by a "frame", which is a collection of all the key values associated to the event. Filtering is done through IceTray by requiring an event to possess certain properties. The Extremely High Energy (EHE) filter used in this work selects bright events with event-wise charge greater than 1000 PE. The EHE filter rate is $\sim$1 Hz. Other filtering algorithms select up-going events, or contained events or other types of events for specific physics analyses.

4.3 Calibration

Photons detected by IceCube DOMs go through multiple steps before they are transformed to digitized signal for read-out. To measure deposited energy and time of events in ice precisely, the PMT gain, digitizer amplification and timing must be understood with precision. Event reconstructions also require precise measurement of DOM positions.

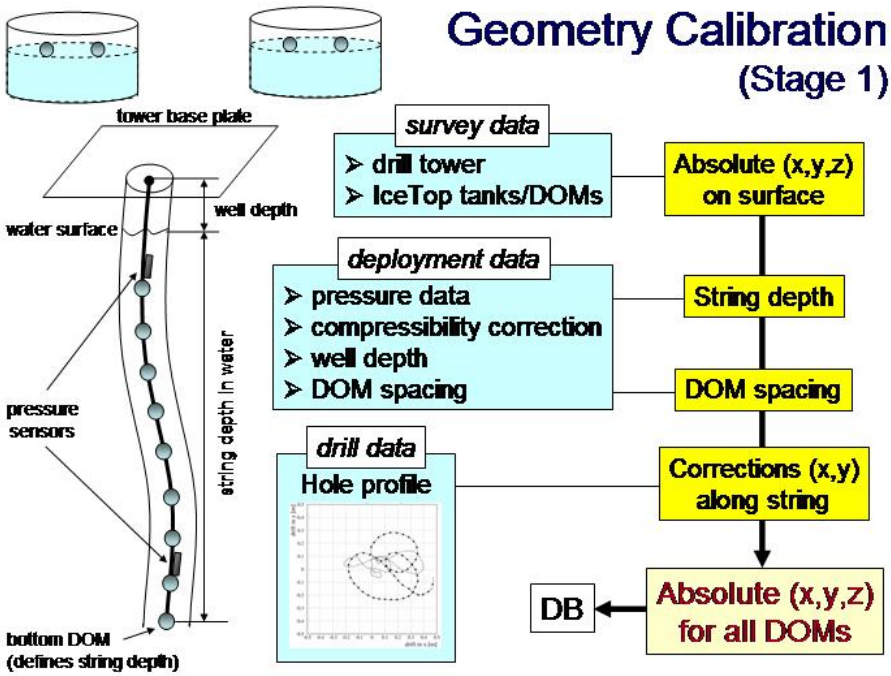

Figure 4.12: Stage 1 geometry calibration, using data from the drill.

4.3.1 Geometry Calibration

The IceCube coordinate system follows a right-handed coordinate system with the origin (0, 0, 0) located at 46500' E, 52200' N, at an elevation of 883.9 m. The y-axis is aligned with the Prime Meridian, pointing towards Greenwich, UK (Grid North), the x-axis points 90° clock-wise from Grid North (Grid East), and the z-axis is perpendicular to the earth's surface, pointing upwards. IceCube geometry calibration is done through two stages.

Stage 1 makes use of non-optical data collected during DOM deployment and pre-deployment survey of the drill tower. It produces a set of 3-dimensional coordinates for all IceCube DOMs in IceCube coordinate system. Figure 4.12 shows what measurements have been done to achieve the stage 1 geometry of the IceCube detector.

Stage 2 measures the relative depth offsets between the top DOM on each string using inter-string LED flasher data. These offsets are measured relative to the stage 1 geometry. For each flasher data taking cycle (a run), a few flashers on every string are initiated, and all adjacent strings are read out. A conjugate hyperbola is then fitted to the receiver distance versus relative depth to

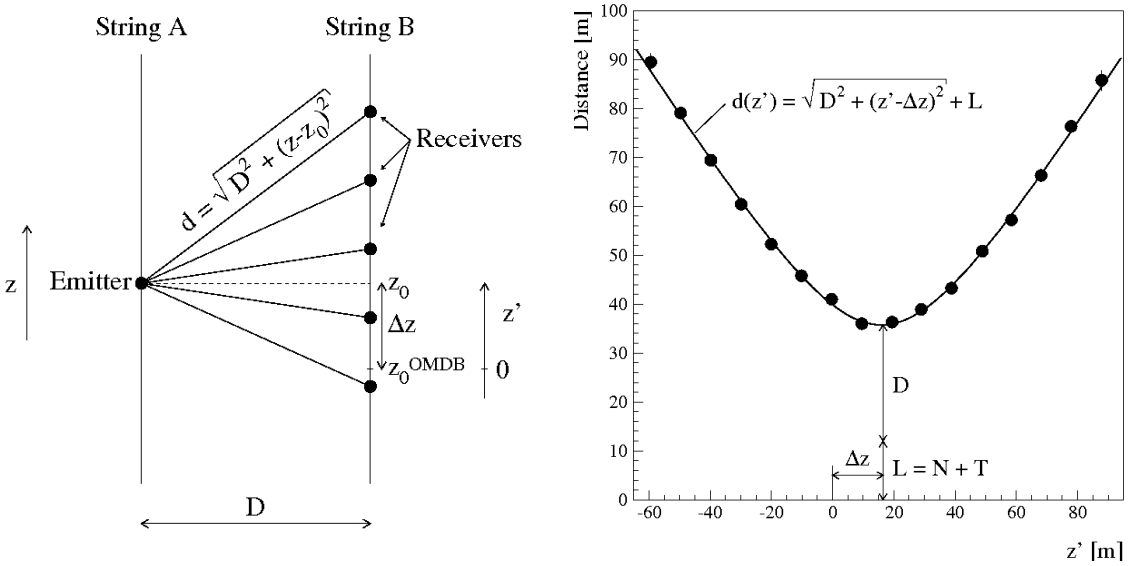

Figure 4.13: Left: parameter definitions of stage 2 geometry calibration. D is the horizontal interstring distance, and Δz is the depth offset. Right: a conjugate hyperbola fit to the receiver distance versus relative depth ($z' = z_{\text{receiver}} - z_{\text{flasher}}$), D and Δz are the extracted interstring distance and depth offset from the fit.

extract interstring distance and depth offsets. Figure 4.13 demonstrates how the calibration procedure at this stage works. At the end, a global fit is done for all flasher and receiver pairs to extract the relative depths for the whole array. Extracted depth offsets from this stage are used to correct stage 1 geometry. At stage 2, the individual DOM positions are measured to a precision of one meter.

4.3.2 Time Calibration

IceCube waveforms are timestamped locally inside the DOMs before being sent up to the surface. This timestamping is controlled by a local free running 20 MHz oscillator located on the DOM MB. Synchronization of the whole array is done through a procedure called RAPCal (Reciprocal Active Pulsing Calibration) [145]. During this procedure, a surface master oscillator controlled by GPS sends a fast bipolar pulse with known interval from the surface DOR (DOm Readout) card to the DOM. Upon receiving this pulse, the DOM will delay for a known interval of time, then sends back an identical fast bipolar pulse to the DOR card. Both bipolar waveforms are produced and digitized by the same Digital to Analog Converters (DACs) and Analog to Digital Converters

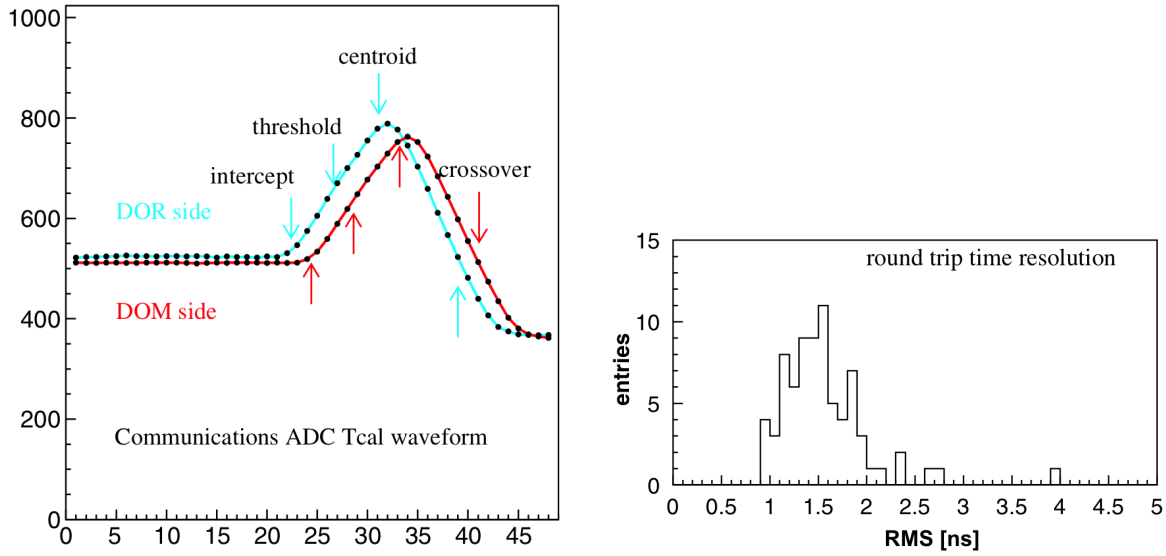

Figure 4.14: Left: RAPCal waveforms. Right: The RMS variation of the round-trip time measured by the RAPCal procedure. Figure is taken from [145].

(ADCs) operating at 20 MSPS. The one-way transit time is one half of the round trip time minus the known delay, which can be extracted from comparing one point on the transmitted waveform to the delayed point on the reciprocal waveform (two waveforms are identical in shape). Time resolution from RAPCal procedure is typically less than 2 ns. This time calibration procedure is done every two seconds. Figure 4.14 shows the RAPCal waveforms and timing variations measured by the RAPCal procedure.

4.3.3 Calibration of ATWD, Amplifier and PMT

The DOM ATWD readout response, DOM front-end amplifier gains for the three channels (16x, 2x, 0.25x) and PMT gains are calibrated by a software package called DOMCal which is embedded on the FPGA. For ATWD readout calibration, DOMCal measures the ATWD readout response by varying the ATWD bias voltage and performing a linear fit to the resulting amplitudes for each bin (0-127) as the ATWD bin readout scales linearly with input voltage. In order to calibrate the PMT gain, the amplifiers with various channels must be calibrated with precision first. For amplifier calibration, the absolute gain of the high-gain channel (16x) is determined first, by injecting artificial single photoelectron (SPE) like pulses to the PMT input and comparing the peak amplitude from

the ATWD response to the true peak amplitude of the injected pulses. To minimize integration error, the waveform sampling speed is maximized. The high-gain amplifier gain is then given from the ratio of the mean peak averaged over many pulses of the response to the true injected pulses. Calibration of the low-gain channels of 2x and 0.25x uses the PMT signals from an LED on the DOM MB as input pulses to both the already calibrated high-gain channel of 16x and the unknown low gain channel, then compare the average ratio between the pulse integrals from the low-gain and high-gain channels. The absolute gain for the low-gain channel is then this ratio times the absolute gain of the high-gain channel. Potential offsets (pedestals) are measured with forced triggers. The individual pedestals for each digitizer bin are measured as a function of the bias voltage during DOMCal. The average baseline offset is measured during data taking with "beacon" hits which are forced launches on each DOM at the rate of 1 Hz. Figure 4.15 (left) shows the ratio of the gains of two ATWD channels [145].

Each PMT has a unique gain related to the photocathode-anode response. A PMT constantly sees light from uncorrelated noise from the thermal background of the photocathode and correlated noise from radioactive decay of isotopes in the DOM glass pressure sphere. This noise results in a significant ($\sim$500 Hz) rate of SPE signals, as demonstrated in Figure 4.15 (right). The nominal gain for a PMT is set to 10^7. The calibration of absolute PMT gain takes several steps as follows: 1) At each high voltage (HV) setting, acquire thousands of PMT waveforms with a low discriminator threshold. 2) Integrate around the peak for each waveform, then the total charge is obtained by multiplying the integrated waveform amplitude with the sampling time interval and then dividing by the load impedance i.e. $C = \frac{V \cdot T}{R}$ where C is the total charge, V is the integrated waveform amplitude, T is the sampling time interval (3.3 ns for ATWD) and R is the load impedance. A distribution of SPE charge is obtained for the group of waveforms. 3) Fit the mean SPE charge distribution to a Gaussian plus exponential component, then the PMT gain is the SPE charge divided by the electron charge. 4) Repeat this procedure for HV ranging from 1200 V to 1900 V in 100 V increments, and fit a linear function to the 1og10 (gain) versus log10 (voltage). The resulting fit function is later used to calculate the voltage which would yield the desired gain [145].

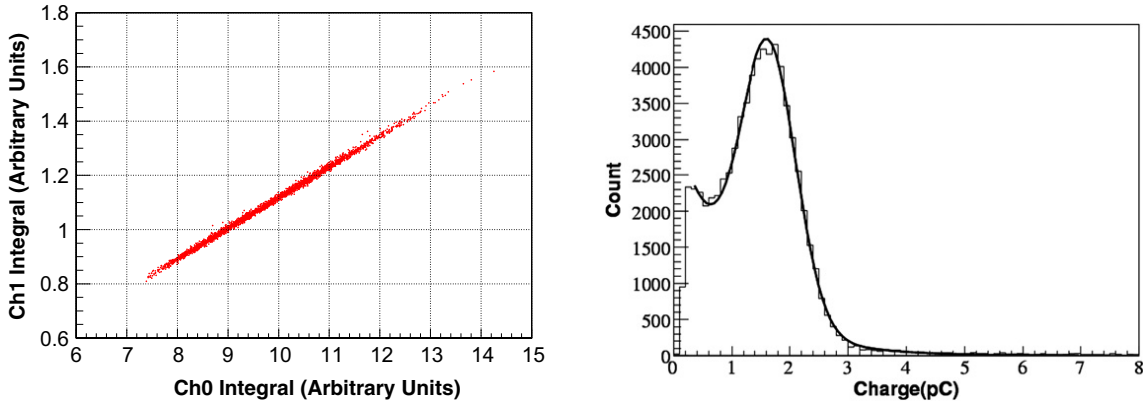

Figure 4.15: Left: Calibration of DOM ATWD low-gain channel 1 to high-gain channel 0. Right: a DOM discriminator spectrum at PMT gain of 10^7, the peak of the spectrum is a Gaussian distribution of SPE. Figure is taken from [145].

Chapter 5

Physics in IceCube

This chapter begins with an overview of physics processes in IceCube including neutrino interactions and the interactions of the resulting charged particles in ice, and the corresponding event topologies. The next section covers IceCube simulation chains and weighting schemes. The third section briefly describes the event reconstructions that are relevant to this work. Finally, recent results from IceCube which motivate this work are summarized.

5.1 Neutrino Interactions in Ice

5.1.1 Neutrino-nucleon Deep Inelastic Scattering

For neutrinos above O(TeV) energies, deep inelastic scattering (DIS) is the dominant process for neutrino-nucleon interaction. All flavors of neutrinos can undergo DIS with ice nuclei through charged-current (CC) and neutral current (NC) interactions:

$$\nu + N \rightarrow l + X \quad (\text{CC}) \tag{5.1}$$

$$\nu + N \rightarrow \nu + X \quad (\text{NC}) \tag{5.2}$$

where ν can be any neutrino or antineutrino flavor[1], l is the appropriate lepton that conserves the lepton number during the interaction process, and X is the emerging hadron system. Figure 5.1 shows Feynman diagrams for both CC and NC DIS interactions.

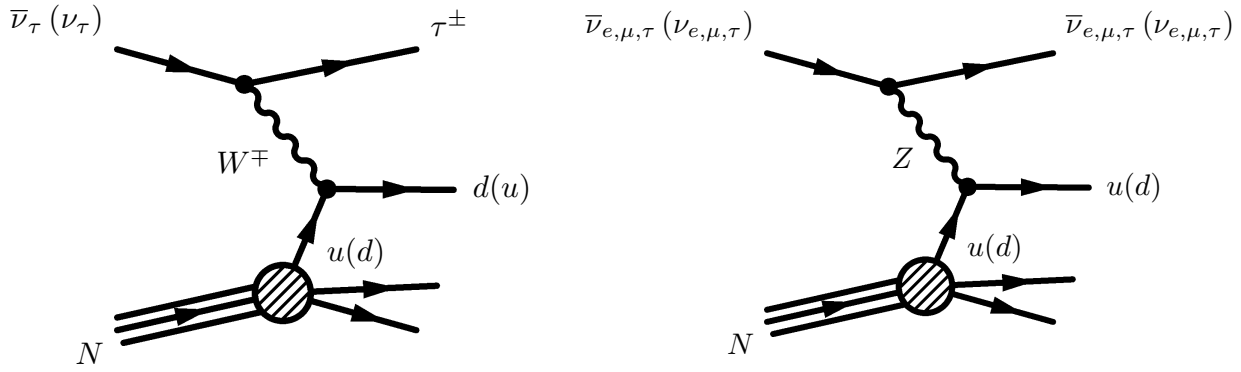

Figure 5.1: Left: a ν_τ undergoing charged-current deep inelastic scattering off a nucleon. The shaded circle indicates the nucleon. One of the three quarks is excited and the neutrino is transformed into a lepton mediated by a charged W boson; the two remaining spectator quarks are associated to the X system of emerging hadrons as written down in formula 5.1. This interaction holds for all neutrino flavors, with ν_τ exchanged for other neutrino flavor and the τ lepton for the corresponding lepton. Right: neutral current deep inelastic interaction for all three flavors of neutrinos. The mediator for this process is the neutral Z boson. Figure is taken from [67].

The differential cross sections for both CC and NC interactions can be written as [154, 155]

$$\frac{d\sigma^2}{dxdy} = \frac{2G_F^2 M E_\nu}{\pi}\left(\frac{M_W^2}{Q^2+M_W^2}\right)^2[xq(x,Q^2)+x\bar{q}(x,Q^2)(1-y)^2] \quad \text{(CC)} \tag{5.3}$$

$$\frac{d\sigma^2}{dxdy} = \frac{G_F^2 M E_\nu}{2\pi}\left(\frac{M_Z^2}{Q^2+M_Z^2}\right)^2[xq^\circ(x,Q^2)+x\bar{q}^\circ(x,Q^2)(1-y)^2] \quad \text{(NC)} \tag{5.4}$$

where the Bjorken scaling variables x and y are defined as

$$x = \frac{Q^2}{2M(E_\nu - E_l)} \tag{5.5}$$

$$y = \frac{E_\nu - E_l}{E_\nu} \tag{5.6}$$

[1]IceCube cannot distinguish neutrinos from antineutrinos on an event by event basis.

Subscript l indicates the appropriate outgoing lepton associated with the corresponding neutrino, Q^2 is the 4-momentum transfer from the incident neutrino to the outgoing lepton (neutrino) in the CC (NC) interaction, M is the nucleon mass, M_W and M_Z are the mass of the mediating bosons, and $G_F = 1.16632 \times 10^{-5}\,\text{GeV}^{-2}$ is the Fermi constant. The quark distribution functions q, $\bar{q}$, q° and $\bar{q}^\circ$ encompass our best knowledge of the nucleon structure, they are dependent on Q^2 and x and usually derived and extrapolated from lepton-hadron scattering and hadron-hadron collision experiments.

5.1.2 Neutrino-electron Scattering

Due to the small mass of an electron compared to that of a nucleon, the neutrino-electron scattering cross sections are expected to be much smaller than that of the neutrino-nucleon DIS processes. However, for the electron antineutrino ($\bar{\nu}_e$) scattering off electrons, the cross sections become important when the center-of-mass energy reaches the scale to excite a W^- boson of rest energy 80.4 GeV [154, 156]:

$$\bar{\nu}_e + e^- \rightarrow W^- \rightarrow \text{anything} \tag{5.7}$$

with the W^- boson decaying to hadrons 67.4% of the time, to an electron 10.7% of the time, to a muon 10.6% of the time and to a tau 11.4% of the time [29]. Take $\bar{\nu}_e + e^- \rightarrow \bar{\nu}_\mu + \mu^-$ as an example, the differential cross section can be written as [154]:

$$\frac{d\sigma(\bar{\nu}_e e^- \rightarrow \bar{\nu}_\mu \mu^-)}{dy} = \frac{G_F^2 m E_\nu}{2\pi} \frac{4(1-y)^2[1-(\mu^2-m^2)^2/2mE_\nu]^2}{(1-2mE_\nu/M_W^2)^2 + \Gamma_W^2/M_W^2} \tag{5.8}$$

where m = 0.51 MeV/c^2 is the electron mass, μ = 105.66 MeV/c^2 is the muon mass, and Γ_W = 2.08 GeV is the total W width [29]. Hence, the energy of a $\bar{\nu}_e$ to cause resonance (Glashow resonance) in Equation 5.8 is

$$E_\nu^{\text{res}} = \frac{M_W^2}{2m} \simeq 6.3\ \text{PeV} \tag{5.9}$$

Cross sections for neutrino-nucleon CC and NC DIS interactions and electron antineutrino-electron interactions, which dominate at the Glashow resonance energy of 6.3 PeV, are shown in Figure 5.2.

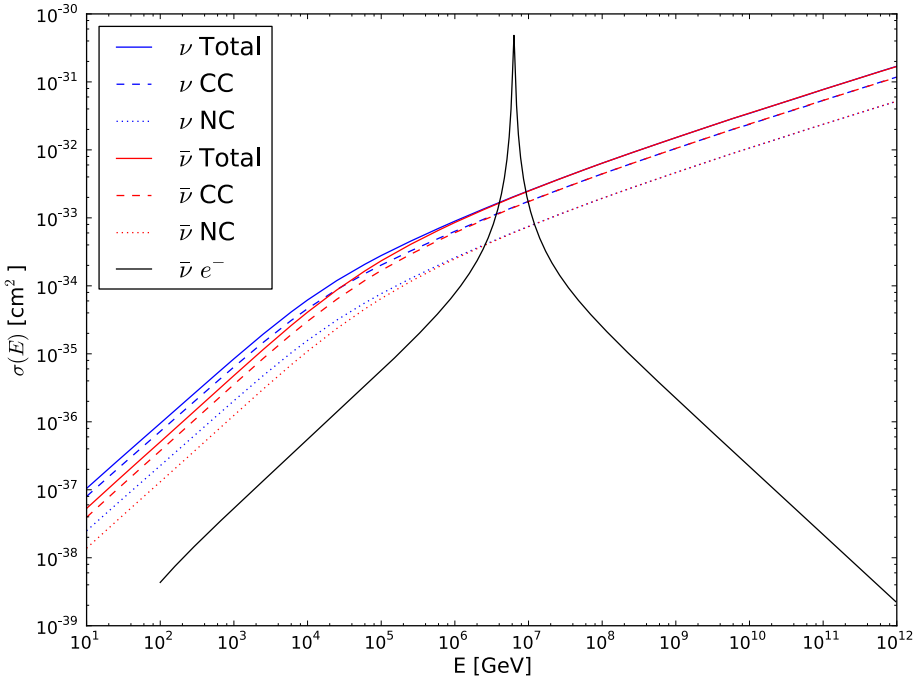

Figure 5.2: Neutrino interaction cross sections as a function of neutrino energy. The blue (red) lines indicate neutrino (antineutrino), and the black line is $\bar{\nu}_e e^-$ cross section which peaks at 6.3 PeV, which is known as the Glashow resonance [156]. At $E_\nu \leq 1$ TeV, $\sigma \propto E_\nu$, and at $E_\nu \geq 1$ PeV, $\sigma \propto E_\nu^{0.4}$ [154]. The data points are taken from [155] and replotted by Voigt Bernhard [157].

5.2 Particle Interactions and Event Topologies in Ice

IceCube detects Cherenkov light from the secondary particles which are induced by neutrino-nucleon DIS interactions. The main composition of these secondary particles include muons, electrons and hadrons, which produce distinctive light patterns in the PMT array.

5.2.1 Cherenkov Radiation

Fast charged particles traveling through some medium will induce the medium to emit Cherenkov radiation if the particle speed $v = \beta c$ exceeds the phase velocity of light c/n in the medium, where n is the refractive index of the medium. The Cherenkov photons are emitted coherently at an angle of $\theta_C = \cos^{-1}(\frac{1}{n(\lambda)\beta})$, and will form a light cone along the direction of the charged particle. The number of Cherenkov photons produced per unit wavelength per unit distance from a particle with charge ze is [158, 29]

$$\frac{dN}{dxd\lambda} = \frac{2\pi\alpha z^2}{\lambda^2}(1 - \frac{1}{\beta^2 n^2(\lambda)}) \tag{5.10}$$

where λ is the photon wavelength and $\alpha \simeq \frac{1}{137}$ is the fine structure constant.

Figure 5.3 illustrates the radiation wavefronts of charged particles traveling at $0.5c$ and c through water.

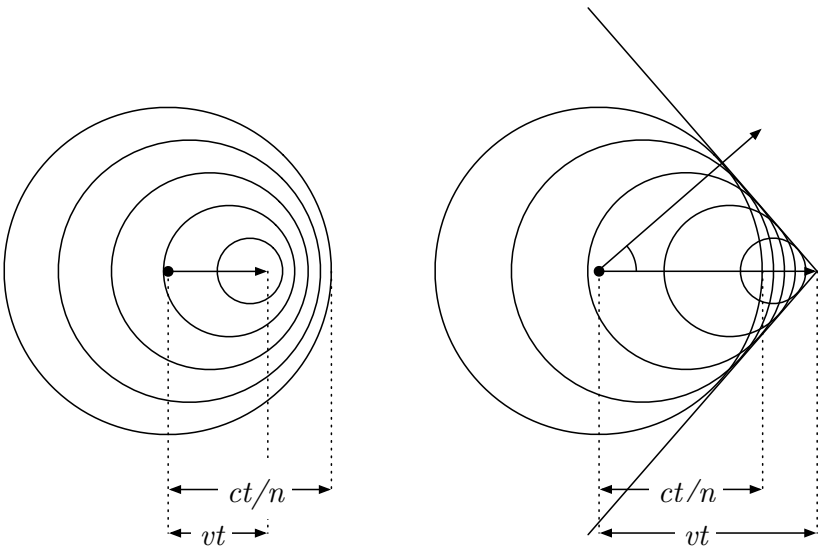

Figure 5.3: Left: radiation wave fronts condense slightly along the direction of travel for charged particle at $0.5c$. Right: Cherenkov light cone with $\theta_C = 41^\circ$ for a charged particle traveling at speed of c in water (n=1.33). Figure is taken from [67].

Since $\cos(\theta_C) = \frac{1}{n\beta} \leq 1$, the threshold speed of the charged particle required to induce Cherenkov radiation is $v \geq \frac{c}{n}$. The threshold energy of the charged particle for Cherenkov radiation can be

derived based on the relativistic energy relations

$$E_C = mc^2 \frac{n}{\sqrt{n^2 - 1}} \tag{5.11}$$

where m is the charged particle mass. The Cherenkov threshold energy in ice ($n = 1.31$) for e is 0.8 MeV, for μ is 164 MeV and for τ is 2750 MeV [153].

5.2.2 Tracks from Muons in Ice

Cosmic ray induced atmospheric muons trigger the IceCube detector at $\sim$ 2.8 kHz. ν_μ undergoing CC interaction also produce outgoing muons. Sufficiently energetic muons passing through matter lose energy mainly through four processes: ionization, bremsstrahlung, e^+e^- pair production, and photonuclear interactions in addition to Cherenkov radiation. The radiative processes (bremsstrahlung, pair production and photonuclear interaction) occur in a stochastic fashion on top of the ionization losses, hence they are also often called "stochastic energy losses". The critical energy $E_{\mu c}$ for muons where ionization energy loss equals radiative energy loss in solids with atomic number Z is given by [29]

$$E_{\mu c} = \frac{5700}{(Z + 1.47)^{0.838}} \text{ GeV} \tag{5.12}$$

For muons passing through ice, $E_{\mu c} \sim 1$ TeV. The average energy loss rate of a muon of energy E can be approximated as

$$-\langle \frac{dE}{dx} \rangle = a(E) + b(E) \cdot E \tag{5.13}$$

where $a(E)$ is the ionization energy loss and $b(E)$ is the sum of stochastic energy losses which include bremsstrahlung, e^+e^- pair production and photonuclear interaction. Most of the cosmic ray induced muons detected in IceCube lose their energy through radiative processes. In the energy range of 20 GeV to 10^{11} GeV, a and b are only weakly energy dependent, the best fit values of a and b for stochastic losses in ice are a = 0.268 GeV (meter water equivalent)$^{-1}$, b = 0.470 $\times 10^{-3}$

(meter water equivalent)$^{-1}$ [159]. Figure 5.4 shows the energy loss processes for a muon traveling through ice, and Figure 5.5 shows the median muon range in ice. On average, a muon loses $\sim$ 50 GeV m^{-1} in ice. A 10 TeV muon could penetrate $\sim$ 2 km through ice, emitting Cherenkov light along its way. The light pattern recorded by the nearby DOMs from a high energy muon is called a "track" in IceCube, see left panel of Figure 5.8.

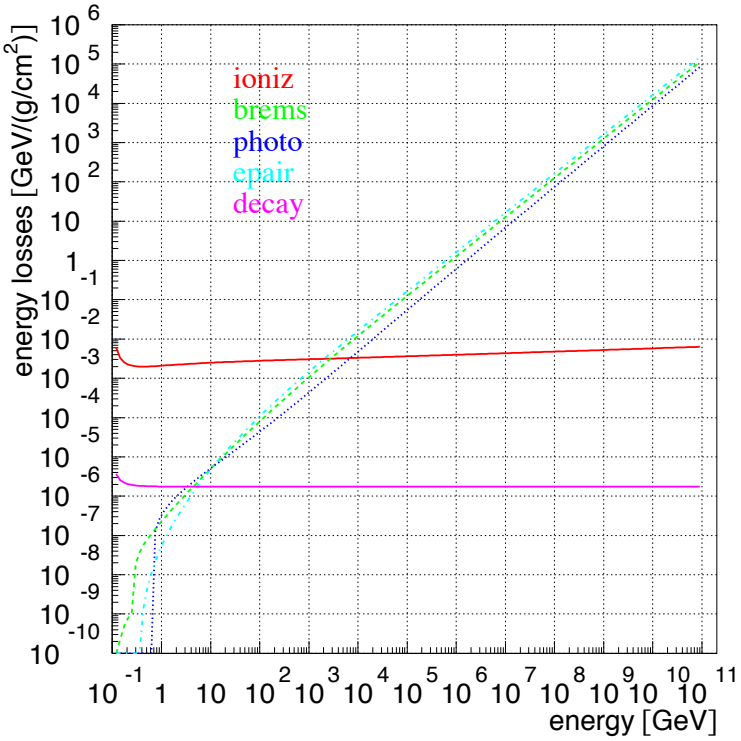

Figure 5.4: Muon energy loss in ice for ionization (red), bremsstrahlung (green), photonuclear interaction (blue), pair production (cyan) and decay (pink). Figure is taken from [159].

5.2.3 Cascades

Cascades are roughly spherical light patterns deposited by ν_e CC, low energy ν_τ CC and NC of all neutrino flavors.

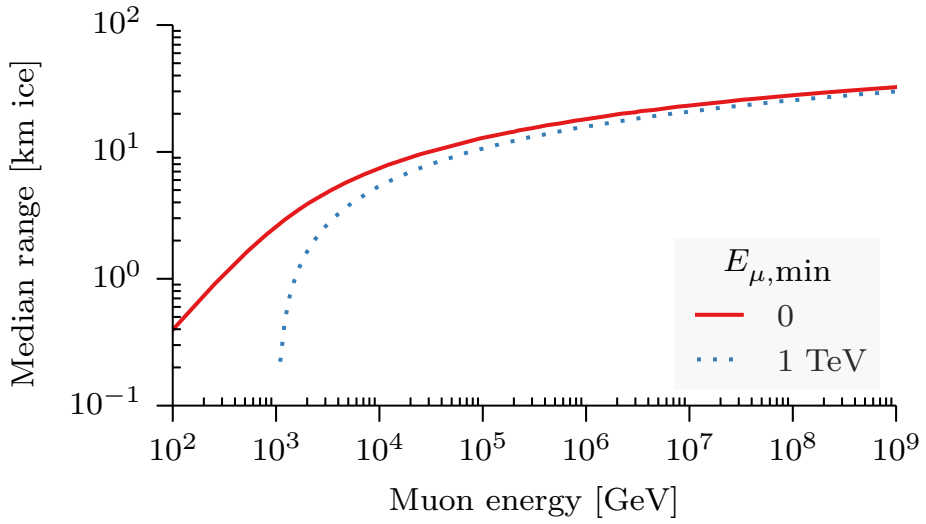

Figure 5.5: Muon range in ice as a function of initial energy. The solid line shows the median range, while the dotted line shows range where 50% of muons still have more than 1 TeV of kinetic energy. Figure is taken from [67], which was calculated using PROPOSAL [160].

Electromagnetic Showers

The CC interaction of a ν_e or $\bar{\nu}_e$ results in an electron or positron. Electrons lose energy in matter similarly to muons, except that electrons are much lighter than muons so they lose energy much faster and stop more quickly in matter. The critical energy for electrons E_{ec} where bremsstrahlung dominates over ionization in solids with atomic number Z is given by [29]

$$E_{ec} = \frac{610}{(Z + 1.24)} \text{ MeV} \tag{5.14}$$

For an electron in ice, $E_{ec} \sim 72$ MeV. For high energy electrons when their energy loss is dominated by bremsstrahlung, the energy loss can be modeled as

$$(\frac{dE}{dx})_{rad} = -\frac{E}{X_0} \tag{5.15}$$

where the electron radiation length X_0 (~ 39 cm in ice [161]) represents the average distance over which an electron reduces to $\frac{1}{e}$ of its total initial energy.

The high energy photons produced from the electron-bremsstrahlung emission continue to lose

energy through e^+e^- pair production. On average, the e^+/e^- each traverses a radiation length X_0 and emits another photon, and that photon goes on to initiate another e^+e^- pair. This process will continue until all the particles fall below the critical energy E_{ec}. This "cascade" or "shower" of particles will develop longitudinally in distance which is t (t=0, 1, 2, ..) multiples of X_0. At step t, the total number of particles is N=2^t. The total track length of the cascade is $L \propto \frac{E_0}{E_{ec}}$ which is proportional to the incident electron energy E_0. Figure 5.6 illustrates the cascade development initiated by a high energy electron [162].

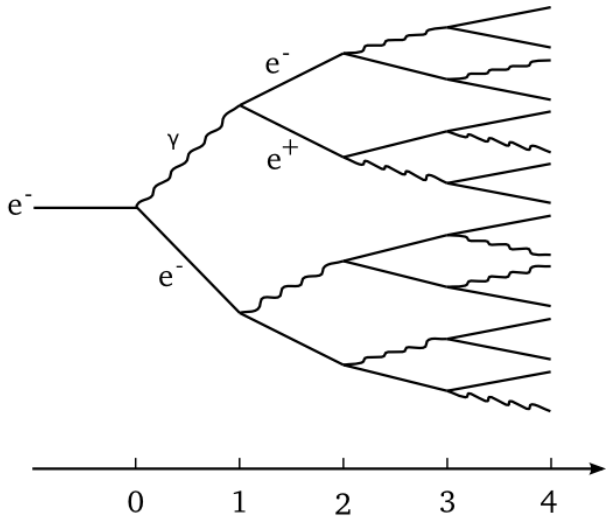

Figure 5.6: Illustration of electromagnetic cascade development [162].

The longitudinal energy deposition of the electromagnetic cascade can be parametrized with a Γ distribution [29]:

$$\frac{dE}{dt} = E_0 b \frac{(tb)^{a-1}\exp(-tb)}{\Gamma(a)} \tag{5.16}$$

where E_0 is the initial energy of the electron, t is the length in unit of radiation length, and a and b for ice are fitted from GEANT simulation to be [163, 164, 165]

$$a = 2.03 + 0.604 \cdot \ln\frac{E_0}{\text{GeV}} \tag{5.17}$$

$$b = 0.633 \tag{5.18}$$

The maximum of the shower occurs when the Γ distribution reach its maximum at $t_{max} = \frac{a-1}{b}$. The transverse spread of the cascade is governed by the Molière radius [29]

$$R_M \simeq 21\text{MeV} \cdot \frac{X_0}{E_{ec}} \tag{5.19}$$

Generically, about 99% of the cascade energy is deposited within 3.5 R_M. A 100 TeV cascade in ice typically has a longitudinal length of $\sim$ 5 m in a cylinder of radius $\sim$ 0.35 m [162].

For cascades over 100 PeV, the cross section for bremsstrahlung and pair production is suppressed due to the Landau-Pomeranchuck-Midgal (LPM) effect, which will elongate the cascade [29].

Hadronic Showers

As discussed before, hadrons can emerge from the neutrino-nucleon DIS interaction vertex. These high energy hadrons also lose energy rapidly in ice, producing showers of baryons and mesons. The system of hadronic energy losses is more complicated than the pure electromagnetic cascade because more particles (charged and uncharged) are involved. Some of the hadronic cascade energy could transfer to neutrons which will not produce Cherenkov light, some of the energy is lost in the nuclear binding, and the Cherenkov energy thresholds for pions, kaons and protons are higher than that of electrons. The combination of those factors result in lower Cherenkov light production from a hadronic cascade than an electromagnetic cascade with same initial energy. Nevertheless, in every hadronic cascade there is an electromagnetic component from $\pi^0 \to \gamma\gamma$. This electromagnetic component becomes more dominant as the hadron cascade energy increases as more π^0 are produced. The ratio of shower lengths from a hadronic cascade and an electromagnetic cascade

with same energy is [164]

$$F = \frac{T_{\text{hadron}}}{T_{\text{em}}} = F_{\text{em}} + (1 - F_{\text{em}}) \cdot f_0 \tag{5.20}$$

where F_{em} represents the electromagnetic fraction of the hadronic cascade, f_0 indicates the relative Cherenkov light production from the purely hadronic part of the hadronic cascade. The electromagnetic fraction F_{em} increases with the cascade energy, and can be modeled as

$$F_{\text{em}} = 1 - (\frac{E}{E_0})^{-m} \tag{5.21}$$

with m and E_0 being parameters which are determined from Monte Carlo simulation.

Figure 5.7 shows the relative Cherenkov light yield F with respect to an electromagnetic cascade with the same energy as a hadronic cascade. For a 100 TeV hadronic cascade, the Cherenkov light yield is $\sim 90\%$ of that from an electromagnetic cascade. Hadronic cascades and electromagnetic cascades cannot be distinguished from each other in IceCube. Middle panel of Figure 5.8 shows a cascade event from a ν_e CC interaction. All NC interactions and low energy ν_τ CC interaction produce cascades of this nature.

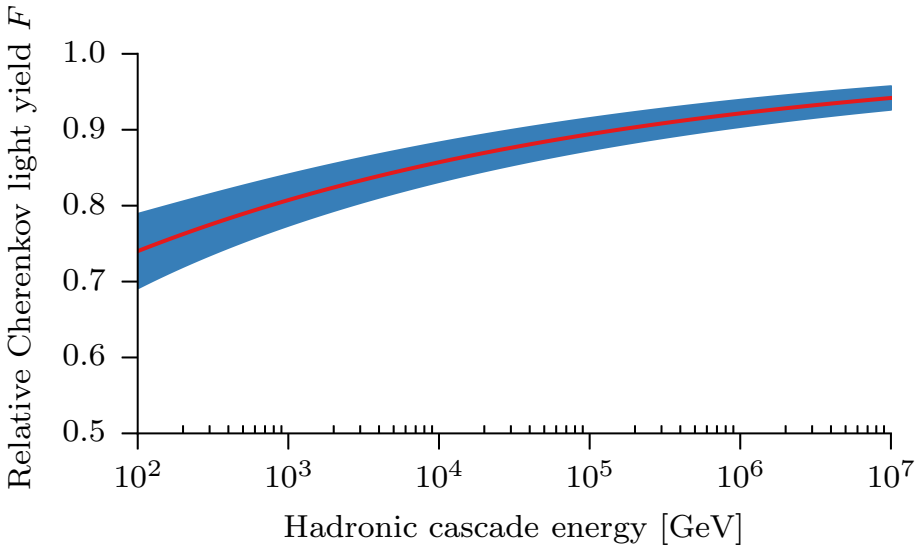

Figure 5.7: Relative Cherenkov light yield from a hadronic cascade as a function of hadronic cascade energy[67].

5.2.4 Double Cascades

At energies above 1 PeV, a ν_τ undergoing CC interaction in IceCube produces a hadronic cascade and a τ lepton that can penetrate tens of meters through the ice before decay. A τ will decay to hadrons 64.8% of the time, to electrons 17.8% of the time and to muons 17.4% of the time. Hadronic and electronic tau decays will produce a second cascade. These two subsequent depositions of energy would form the distinctive pattern of a "double bang" signature for ν_τ in IceCube [2], see right panel of Figure 5.8. To date, this signature has not been observed in IceCube. This work looks for a double cascade which can be resolved by a single IceCube sensor, as described in Chapter 6.

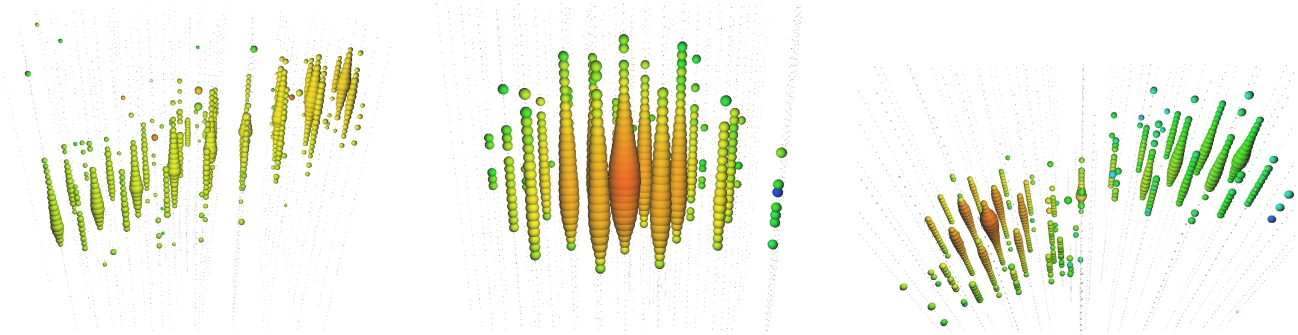

Figure 5.8: Left: a simulated track made by a 117 TeV muon in IceCube. Middle: a simulated cascade event made by a 3.61 PeV ν_τ CC event, the τ lepton decays to hadrons of 2.92 PeV. A ν_e CC interaction and NC interaction of all neutrino flavors will be of this event shape. Right: a simulated double bang event made by a 328 PeV ν_τ CC event, the second "bang" is from the τ lepton decay to 119 PeV hadrons. The time sequence is indicated by rainbow colors with red representing early and blue late.

5.3 Simulations

Physical processes in IceCube are simulated in a chain of Monte Carlo simulations, which model the particle interactions and propagations occurring both in the air and in the ice, and the detector response when photons register at the detector. To meet the challenge of computational expense, a scheme of weighting is employed in IceCube's particle simulations.

5.3.1 Simulation Chains

Simulations in IceCube are done in four major steps. First of all, primary cosmic rays and neutrinos near the surface of the Earth are simulated by a **Particle Generator**, and then propagated through the atmosphere and ice through a **Particle Propagator**. Photons induced by particles passing through ice are propagated through a **Photon Propagator**. When photons register at the PMTs, a series of processes are simulated with **Detector Response** which encompasses **HitMaker** that makes the "hits", and **DOMLauncher** that simulates the DOM electronics response to the hits and produces raw voltage output corresponding to the hits.

Particle Generator

CORSIKA - Atmospheric muon simulations are done using an air shower simulation program named CORSIKA (COsmic Ray SImulations for KAscade [166, 167]). CORSIKA in detail simulates extensive air showers caused by high energy cosmic ray particles. Nuclei ranging from protons up to iron, photons and other particles may be treated as primaries. These primary particles are tracked through the atmosphere until they interact with an air nuclei or decay. Three major types of interactions are treated in CORSIKA: hadronic interactions, particle decays and electromagnetic interactions. CORSIKA simulation in IceCube uses the SIBYLL hadronic interaction model [168]. For atmospheric down-going muon simulation, IceCube adopts an internal release of CORSIKA with the name dCORSIKA which accounts for the necessary modifications specific to the IceCube detector and AMANDA – the obsolete predecessor of IceCube. dCORSIKA traces primaries and secondaries through the atmosphere and stores the outgoing muons.

Neutrino Generator - Neutrino simulations used in this work are done with the Neutrino Generator ("NuGen" in short) [169], which incorporates the neutrino-nucleon DIS cross sections using the CTEQ5[2] parton distribution functions [170]. The NuGen simulations can simulate neutrinos with energy from 10 GeV to 10^9 GeV. However, below a few hundred GeV, other neutrino interaction processes, such as quasi inelastic scattering and resonances, become important. At energies between 1 GeV and 200 GeV where atmospheric neutrino oscillation physics and solar dark matter

[2]The Coordinated Theoretical-Experimental Project on QCD

physics are important for the IceCube-DeepCore detector, the GENIE (Generates Events for Neutrino Interaction Experiments [171]) neutrino generator is employed that GENIE accounts for the neutrino interaction cross sections relevant at these energies.

Particle Propagator

Charged leptons are propagated through matter (rock and ice) using the Monte Carlo code PROPOSAL (Propagator with Optimal Precision and Optimized Speed for All Leptons, written in C++) [160], which is a reimplementation of the Muon Monte Carlo (MMC, written in Java) [159] for better performance and compatibility with contemporary computing platforms. In MMC/PROPOSAL, the muon energy loss is treated with two components, the continuous minimum ionization loss and the stochastic loss from the bremsstrahlung process, e^+e^- pair production, and photonuclear interactions. Tau decay in MMC/PROPOSAL is treated as follows: 1) leptonic decay of a tau into a muon (branching ratio 17.37%) or an electron (branching ratio 17.83%) are treated exactly as a two-body decay into a neutrino and a lepton; 2) hadronic decay is approximated by a two-body decay into a neutrino and a hadronic part, which is one of the following four particles/resonances: π (11.09%), ρ-770 (25.40%, M=769.3 MeV/c^2), a_1-1260 (18.26%, M=1230 MeV/c^2) and ρ-1465 (10.05%, M=1465 MeV/c^2). The energy of the hadronic part is $\frac{m_\tau^2+M^2}{2m_\tau} \cdot c^2$ in the tau rest frame.

Photon Propagator

The photons induced by the secondary particles (from neutrino interactions) passing through matter are propagated through the ice by the Photon Propagation Code (PPC) [150]. PPC tracks every single photon through the detector, so it consumes a large amount of computing resources. It is most optimal to run PPC on the Graphics Processing Unit (GPU) of a graphics card, which is much more efficient than the standard CPUs due to their highly parallel structure.

Detector Response

Once the simulated photons register at the DOMs, Monte Carlo hits (MCHits) are made by the HitMaker. Then the noise simulation is added to account for the noise rate from each DOM.

The average dark noise rate for each DOM is $\sim$ 500 Hz in IceCube, and is assumed to arise from an uncorrelated Poisson process that is of thermionic origin. A recent new development of noise simulation in IceCube called "Vuvuzela" accounts for the correlated noise originating from radioactive decays and scintillation in the PMT glass. The proper treatment of this correlated noise is of essential importance for low energy events as they can trigger the detector and mimic a physical event [172]. The MCHits are then passed to the PMTResponseSimulator which simulates the PMT physics including amplification, time jitter and saturation. A charge is assigned to the MCHits based on a known PE distribution and a discriminator threshold of $\frac{1}{4}$ PE is applied, making a series of MCPulses. The MCPulses from the PMT response are further passed through the DOMLauncher where the HLC/SLC logic is modeled and the digitization of ATWD and fADC waveforms are simulated. This waveform information is packeted and stored in an object called "InIceRawData". The triggering of the detector is also simulated through the dedicated trigger simulation package called TriggerSim.

5.3.2 Weighting

Tracking enormous numbers of particles traversing through the atmosphere is computationally intense. Since the cosmic ray primary energy spectrum follows a power law function, many more events occur at low energy than at high energy. However, the majority of lower energy events won't trigger the detector. Therefore, if the simulation is done following the natural cosmic ray spectrum, much computing time will be wasted by simulating the lower energy events. To solve this challenge, IceCube simulation adopts a method of sampling based on importance, a..a. weighting.

CORSIKA

In the weighted simulation scheme, events can be sampled based on any energy spectrum, provided that one knows the probability of how likely such an event would happen in reality. For instance, to ensure simulation efficiency at higher energy, one would want to simulate a high energy optimized sample with a steeper spectrum rather than with the realistic cosmic ray spectrum of $E^{-2.7}$. The importance-sampling weight can be calculated:

$$w(E) = \frac{A_{total}}{N p_{gen}(E)} \Phi_{target}(E) \tag{5.22}$$

where $A_{total} = \int_0^{\pi/2} (\pi r^2 \cdot cos\theta + l \cdot 2r \cdot sin\theta) \cdot d\Omega = \pi^2 r(r+l)$ is a constant with unit of $m^2 sr$ [173], N is the total number of generated events (usually, number of generated events per file times number of files), Φ_{target} is the cosmic ray flux being weighted to, in units of GeV^{-1} m^{-2} s^{-1} sr^{-1}, and p_{gen} is the probability of drawing a certain event with energy E from the generation spectrum. The generation probability is defined as:

$$p_{gen}(E, Z) = \begin{cases} \frac{E^{-\gamma}}{\int_{E_0}^{E_1} E^{-\gamma}\,\mathrm{d}E} & \text{if } \; E_0 \leq E \leq E_1 \\ 0 & \text{otherwise} \end{cases} \tag{5.23}$$

The generation probability depends on both energy and primary particle type Z. With these ingredients put together, the unit for $w(E)$ is one over time.

IceCube is a multi-purpose neutrino detector. Various physics analyses are ongoing with different physics goals targeting different energy ranges. Therefore, simulation samples are also optimized for different energy ranges to suit the various physics goals. Often, the analyser will need to combine many sets of simulation samples to gain maximum statistics and coverage of effective livetime. It is straightforward to combine multiple samples with different generation spectra together. The importance-sampling weight for an event with energy E and type Z (Z=1,...,26) from multiple simulation samples with different generation spectrum is:

$$\tilde{w}(E) = \frac{A_{total}}{\sum_i N_{Z,i}\, p_{gen,i}(E, Z)} \Phi_{target}(E) \tag{5.24}$$

$N_{Z,i}$ is the total number of events generated for Z-type primary particle in the i^{th} sample, $p_{gen,i}$ is the drawing probability for such an event within that sample. Note that the difference between

the event weight from a single simulation sample and combined samples is in the normalization. Instead of normalizing to a single generation sample $Np_{gen}(E)$, now the weight is – renormalized to account for the contributions from various samples – normalizing to an entries-weighted sum of these samples $\sum_i N_{Z,i}\, p_{gen,i}(E, Z)$.

For weighted simulation, effective livetime T_{eff} is defined as the time it would take to get N_{eff} events out of an unweighted simulation which generates $N_{unweighted}$ events in $T_{unweighted}$ seconds [174]. Hence, T_{eff} can be computed as:

$$T_{eff} = \left(\frac{\sum_i w_i}{\sum_i w_i^2} \right) \tag{5.25}$$

where $N_{eff} = \sum_i w_i$ and variance of the weights is $\sigma^2 = \sum_i w_i^2$. When plotting weighted Monte Carlo data, say in a 1D histogram, one typically plots the $\sqrt{\sum_i^{N_j} w_i^2}$ (N_j is the total number of entries in bin j) as statistical error for bin j.

5-component CORSIKA - The most popular CORSIKA simulation currently employed in IceCube is the 5-component CORSIKA which generates cosmic rays with different fractions of the 5 primary nuclei H, He, N, Al, and Fe with an arbitrary power-law spectrum with index < 1.0. Weights associated with each event are generated such that when applied to the events, the ratio of the nuclei is of 1:1:1:1:1 and the spectrum is E^0. Then the simulated 5-component CORSIKA samples can be weighted to any flux models. Other CORSIKA simulations in IceCube include unweighted CORSIKA which simulates natural spectra like Polygonato ("many knees" in Greek) by Hörandel [175].

The total weight of each 5-component CORSIKA event i is

$$\mathrm{W}_i = \frac{\mathrm{Weight}_i \cdot \mathrm{DiplopiaWeight}_i \cdot \mathrm{PolygonatoWeight}_i}{\mathrm{TimeScale}_i} \tag{5.26}$$

Weight: the weight indicating importance-of-sampling.

DiplopiaWeight: In IceCube, we simulate single and multiple cosmic ray induced muon events separately. This weight factor accounts for the probability that generated single events actually in

coincidence with other uncorrelated events.

PolygonatoWeight: the polygonato weight accounts for the weighting factor for each primary nucleon type following the polygonato scheme.

$$\text{PolygonatoWeight} = \Phi^0_{Z,tot} \cdot \text{pure}_{27} \cdot \text{rigidity} \tag{5.27}$$

Where

$$\Phi^0_{Z,tot} = \begin{cases} 11735.95, & Z_{prim} = 1 \\ 4749.37, & Z_{prim} = 2 \\ 3315.46, & Z_{prim} = 7 \\ 2816.35, & Z_{prim} = 13 \\ 1157.33, & Z_{prim} = 26 \end{cases} \tag{5.28}$$

with Z_{prim} being the atomic number of each primary nucleon type, and $\Phi^0_{Z,tot}$ are flux model weights in units of GeV.

$$\text{pure}_{27} = \begin{cases} E_{prim}^{-2.71}, & Z_{prim} = 1 \\ E_{prim}^{-2.64}, & Z_{prim} = 2 \\ E_{prim}^{-2.67}, & Z_{prim} = 7 \\ E_{prim}^{-2.65}, & Z_{prim} = 13 \\ E_{prim}^{-2.575}, & Z_{prim} = 26 \end{cases} \tag{5.29}$$

with E_{prim} being the primary energy. The Polygonato modification is then reflected by the rigidity

$$\text{rigidity} = [1 + (\frac{E_{prim}}{4.5 \times 10^6 \cdot Z_{prim}})^{1.9}]^{(-\frac{2.1}{1.9})} \tag{5.30}$$

TimeScale: total simulated time scale in seconds for a specific event.

Figure 5.9 shows the 5-component total weights distribution as a function of primary energy.

Therefore, the total number of CORSIKA events triggering the detector is

$$\sum_i \mathrm{W}_i = N_{\text{trigger events}} \tag{5.31}$$

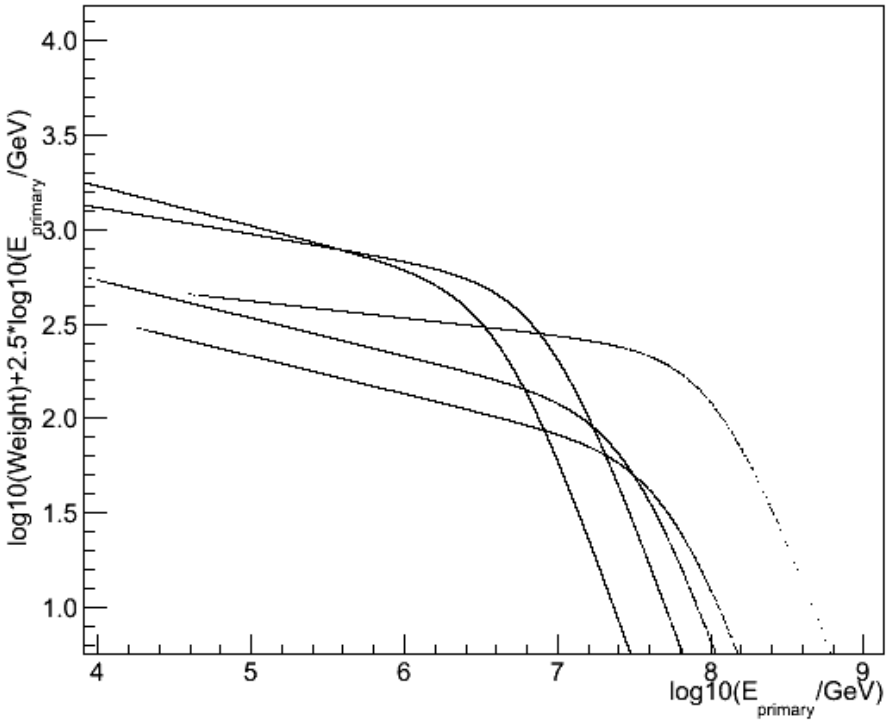

Figure 5.9: Distribution of 5-component CORSIKA weights for each of the five components as a function of primary energy.

Neutrino Generator

The same sampling scheme is employed in NuGen data with a few names changed. The weight for NuGen neutrinos is of the form

$$w(E,\theta) = p_{int}\frac{A\Omega}{N p_{gen}(E)}\ \Phi_{target}(E,\theta) \tag{5.32}$$

where A $\equiv \pi r_{gen}^2$ is the total area of NuGen's injection surface, $\Omega \equiv (cos\theta_1 - cos\theta_0)(\Phi_1 - \Phi_0)$ is the solid angle over which events are generated and p_{int} is the actual interaction probability for

a neutrino at some point of the detector where it was forced to interact. Similar to CORSIKA weighting, the weight for combined NuGen samples with different generation spectra is

$$\tilde{w}(E) = p_{int} \frac{A\Omega}{\sum_i N_i p_{gen,i}(E)} \Phi_{target}(E, \theta) \tag{5.33}$$

5.4 Event Reconstruction

Event reconstruction in IceCube attempts to solve for a set of physical parameters such as time and energy that is specific to a certain event, based on the collective information of time and charge recorded in the PMTs. There are two major event reconstruction hypotheses in IceCube: track and cascade. A third hypothesis is hybrid which usually tries to reconstruct an event topology with a cascade plus an outgoing muon track or double bang topology as discussed in the previous section.

Event reconstructions take place in multiple stages in IceCube data processing and analysis. Some first guess reconstruction algorithms based on χ^2 fitting to the hit time and hit DOM postions are run at the South Pole to quickly identify and filter the obviously track-like atmospheric muons so that transmitted data could fit the allocated satellite bandwidth. These first guess reconstructions do not account for the scattering and absorption of photons in ice. More sophisticated reconstructions involving maximum likelihood methods take into account the ice properties by using tabulated results of light propagation in ice based on simulation [176].

5.4.1 Likelihood Models

Time likelihood

The shortest time for photons to arrive at a DOM is the time for them to travel the distance from the emission point to the DOM without scattering, this time is called t_{geo} and those photons are called "direct photons". Often, photons are scattered and take longer time than t_{geo} to arrive at a given DOM. A relative arrival time, called the time residual, can be defined as the difference between the actual hit time t_{hit} and t_{geo}, $t_{\text{res}} \equiv t_{\text{hit}} - t_{\text{geo}}$. The distribution of t_{res} depends strongly on the distance d and orientation η of the DOM from the track where the Cherenkov photons are emitted. Hence,

the probability distribution function (p.d.f.) for arrival time for a single photon can be written as $p(t_{\text{res}}|\mathbf{a})$, where **a**=($d$, η) is a vector encompassing the physical parameters specific to a given DOM location. Then, the time likelihood can be constructed as [177]

$$\mathcal{L}_T = \prod_i^{N_{\text{hits}}} p(t_{\text{res},i}|\mathbf{a} = d_i, \eta_i, ...) \tag{5.34}$$

This time likelihood function is most important in track reconstructions.

Energy likelihood

For a deposition of energy E in ice, the expected number of photons λ detected follow a Poisson distribution [176].

$$\lambda = \Lambda E + \rho \tag{5.35}$$

with Λ being photons produced per unit energy and ρ the expected number of photons from noise.

The likelihood $\mathcal{L}$ for an energy E deposition which results in k actual detected photons is

$$\mathcal{L}_E = \frac{\lambda^k}{k!} \cdot e^{-\lambda} \tag{5.36}$$

substituting λ for Equation 5.35 and taking the logarithm of $\mathcal{L}_E$ will give

$$\ln\mathcal{L}_E = k\ln(E\Lambda + \rho) - (E\Lambda + \rho) - \ln(k!) \tag{5.37}$$

The energy E can be obtained by maximizing Equation 5.37 with respect to E. This energy likelihood function is most important in cascade reconstructions.

5.4.2 Track Reconstruction

The track reconstruction in this work uses an empirical parametrization of the photon arrival time distribution $p(t_{\text{res}}|\mathbf{a})$ based on analysis of laser light signals from the BAIKAL experiment [178]. Only the earliest arrival time of a photon in each DOM is used in constructing the p.d.f., so this

track reconstruction algorithm is called **SPE** (short for single photoelectron). The SPE is seeded with results from a first guess reconstruction for fast convergence and iterates 32 times with randomly chosen directions. A minimum of the negative log-likelihood $-\ln\mathcal{L}_{\text{min}}$ is returned for each reconstructed event. A reduced log-likelihood is derived by normalizing $-\ln\mathcal{L}_{\text{min}}$ to the number of degrees of freedom ($n_{d.o.f.}$) associated with each reconstruction, $n_{d.o.f.}$ is usually represented by the number of hit DOMs (N_{Ch}).

$$r\ln\mathcal{L} = \frac{-\ln\mathcal{L}_{\text{min}}}{N_{\text{Ch}}} \tag{5.38}$$

5.4.3 Cascade Reconstruction

Two cascade reconstruction algorithms are used in this work. The first one is called **CascadeLLH**, which uses the same analytical arrival time distribution as in SPE except with a point source emitter hypothesis. CascadeLLH is seeded with another first guess algorithm which provides a center-of-gravity (COG) position and an average time. Similarly to SPE reconstruction, a reduced log-likelihood $r\ln\mathcal{L}$ is returned for each CascadeLLH reconstructed event. The reduced log-likelihood $r\ln\mathcal{L}$ from SPE for an intrinsically track-like event is lower than for a cascade-like event. Likewise, the reduced log-likelihood $r\ln\mathcal{L}$ from CascadeLLH for an intrinsically cascade-like event is lower than for a track-like event. Therefore, the difference between $r\ln\mathcal{L}$ from SPE and $r\ln\mathcal{L}$ from CascadeLLH is used to separate cascade-like events from track-like ones in the event selection, more details are given in Section 6.3.2. Table 5.1 summarizes the average $r\ln\mathcal{L}$ values for SPE and CascadeLLH reconstructions on both signal ν_τ and background CORSIKA sub samples.

Table 5.1: Average $r\ln\mathcal{L}$ values from SPE and CascadeLLH reconstructions. The difference between average $r\ln\mathcal{L}$ from CascadeLLH and SPE, as summarized in the 4^{th} column, is more negative for ν_τ than CORSIKA.

Samples	$\langle$SPE.$r\ln\mathcal{L}\rangle$	$\langle$CascadeLLH.$r\ln\mathcal{L}\rangle$	$\langle$CascadeLLH.$r\ln\mathcal{L}\rangle$ - $\langle$SPE.$r\ln\mathcal{L}\rangle$
ν_τ CC	7.646	7.213	-0.433
CORSIKA	7.618	7.476	-0.142

A more sophisticated cascade reconstruction algorithm, called **Monopod**, is employed to determine event vertices at higher event selection levels. Due to the layered structure of the South Pole glacial ice, the arrival time and number of detectable photons at a certain DOM from an energy deposition in the detector can not be modeled in simple analytical terms. To obtain the best reconstruction results, a tabulated template of light yields from a simulated 1 GeV electromagnetic cascade is employed. Then the deposited energy can be inferred by scaling the template to match the total collected charge by each DOM. This tabulated template is obtained from Photonics simulation [179] and fitted to a 5-dimensional B-spline surface [180]. Full charge information extracted from the binned waveforms is used in the log-likelihood construction based on the form as expressed in Equation 5.37. In bin i, the probability of observing k_i PE with an expected charge of μ_i PE follows a Poisson distribution. A set of best fit values of event vertex, direction, time and energy are returned by maximizing the binned log-likelihood. The energy resolution from Monopod is $\sim$8% above 100 TeV, vertex resolution is $\sim$10 m horizontally and $\sim$5 m vertically [67, 176].

5.5 Recent Results

5.5.1 Diffuse Astrophysical Neutrino Flux

A recent search for high energy neutrinos in IceCube has found 37 events with a total of $15^{+7.2}_{-4.5}$ expected atmospheric events (atmospheric muons + atmospheric neutrinos) in three years of IceCube data collected over the time period of 2010-2013 (988 days of livetime). One of these 37 events is clearly produced by a coincident pair of background muons from unrelated air showers and hence is excluded from the sample. The result from this analysis exclude a pure atmospheric origin hypothesis at 5.7σ significance [1].

A veto (as illustrated in Figure 5.10) was employed in this search to remove atmospheric muon tracks that originate from outside of the detector. It also removes atmospheric neutrinos which have accompanying muons produced from the same cosmic ray induced air shower [181]:

Figure 5.11 shows the deposited energy (left) and declination (right) distributions of the observed events. The event energies range from 30 TeV to 2000 TeV. The 2000 TeV event is the

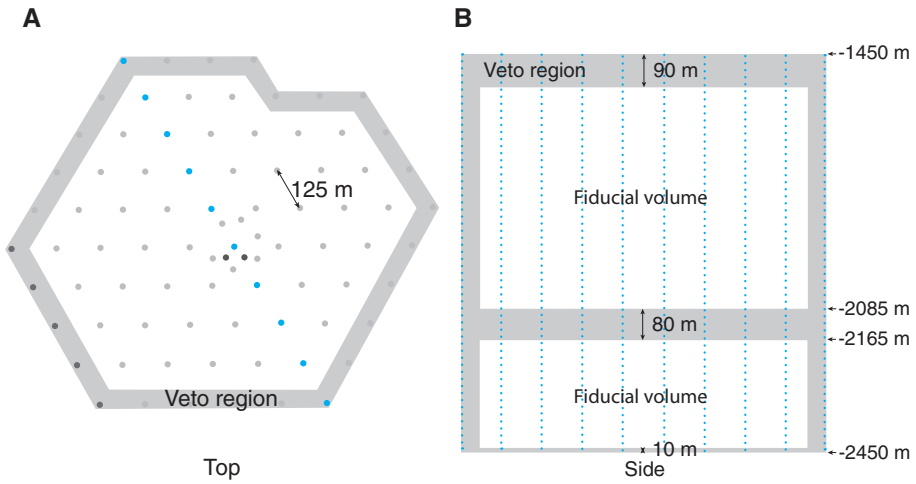

Figure 5.10: Sketch of atmospheric self veto [181].

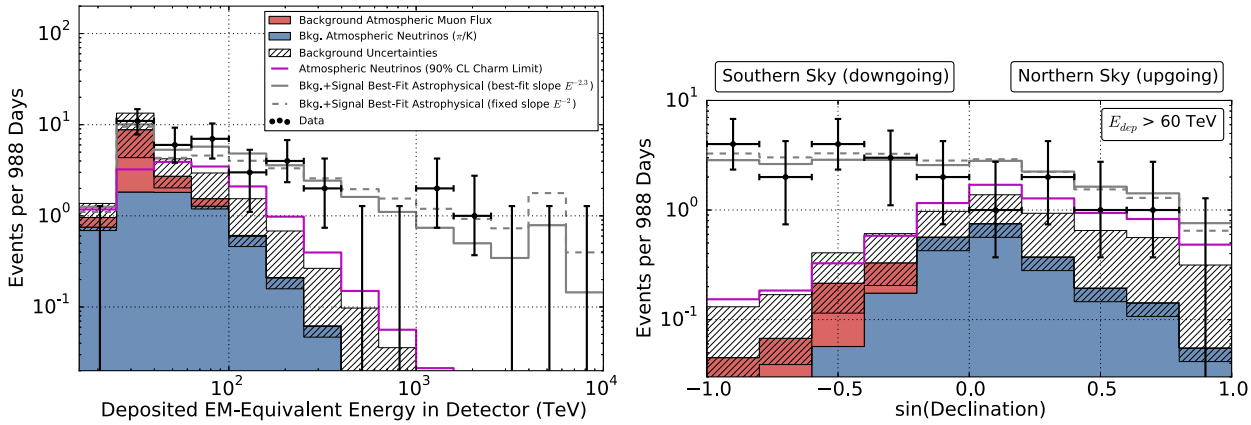

Figure 5.11: Left: deposited energy distribution of observed high energy starting events in IceCube. Right: declination distribution of observed high energy starting events in IceCube [1].

highest energy neutrino interaction ever observed. Among these 36 events, 28 are cascades and 8 are tracks. This is consistent with equal fractions of all neutrino flavors, or a fully oscillated astrophysical neutrino flux at Earth's surface. Note that in this analysis, no attempt is made to distinguish tau neutrinos from other flavors. So far, the observed astrophysical neutrino flux appears to be diffuse. No significant clustering in space or time has been identified with these events. A sky map of the arrival directions of these events is shown in Figure 5.12 [1].

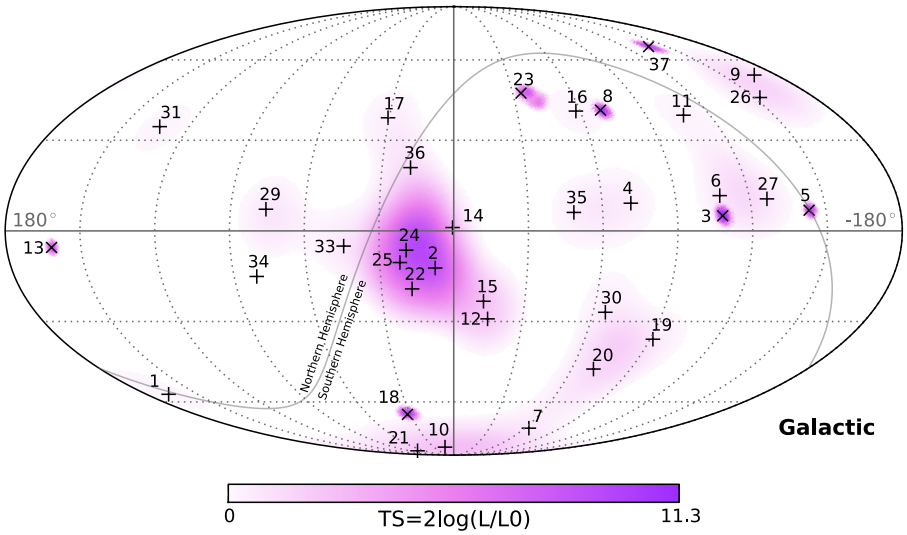

Figure 5.12: Sky map for observed high energy starting events in IceCube [1]. The sky map is in galactic coordinates; the center of the map is the galactic center.

5.5.2 ν_τ Double Bang Search

A search for ultra-high-energy (UHE) ν_τ double bang events was performed with data collected during the IceCube construction stage with 22 strings instrumented. The analysis searched for event signatures that are consistent with ν_τ CC interactions fully and partially contained within the partially instrumented detector. A fully contained ν_τ CC event will have a double bang signature while a partially contained event with one of the cascades outside of the detector will have a hybrid track plus cascade signature. A total of 200 days of livetime were used. The analysis found 3 events with 0.6 ± 0.19 (stat.)$^{+0.56}_{-0.58}$ (syst.) expected background events. Closer inspection of these 3 events indicate that they are consistent with background. One of the events is consistent with light produced by an AMANDA optical module that was observed to emit light intermittently, the second is consistent with a nearly horizontal muon interaction near the bottom of the detector, and the third event has the characteristics of a neutrino-induced shower yet the scenario of it being produced by an atmospheric muon accompanied by a stochastic energy loss can not be ruled out. The analysis methods developed for this search turned out to be almost equally sensitive to all flavors of neutrinos, and was in fact more sensitive to ν_e than to ν_τ. An upper limit on UHE

astrophysical neutrinos of all flavors was thus set to be $E_\nu^2 \Phi_{90}(\nu) < 16.3 \times 10^{-8}$ GeV cm^{-2} sr^{-1} s^{-1} for the neutrino energy range of 340 TeV to 200 PeV [182], based on an older version of the Waxman-Bahcall upper bound as discussed in Section 3.2 [183].

Chapter 6 and 7 describe my search for tau neutrinos, the first dedicated search for tau neutrinos in the full IceCube data sample.

Chapter 6

Analysis: A Search for Double Pulse Signals from Astrophysical ν_τ

As discussed in Section 5.5, a very recent all-flavor search for high energy astrophysical neutrinos in IceCube has observed 37 events in three years with 28 cascades, 8 tracks and 1 coincident atmospheric muon event, with a total expectation of $15^{+7.2}_{-4.5}$ atmospheric background events. Assuming a neutrino flavor ratio of $\nu_e : \nu_\mu : \nu_\tau = 1 : 1 : 1$ at Earth's surface, about 7 ν_τ events are expected. Since the ratio of charged current (CC) events to neutral current (NC) events is $\sim 2 : 1$ at these energies, about 5 astrophysical ν_τ CC events are expected in IceCube in three years. The prompt ν_τ production rate in the atmosphere is at least two orders of magnitude lower than the astrophysical ν_τ rates and hence the background is negligible. Therefore, if we identify high energy ν_τ events in IceCube, they are very likely to have originated from astrophysical sources.

A high energy (>100 TeV) ν_τ undergoing a charged current (CC) interaction in the ice would produce two showers, with the first shower from deep inelastic scattering (DIS) interaction of ν_τ with the ice nuclei and the other from the hadronic or electromagnetic tau lepton decay, see Fig. 6.1. A ν_τ CC event would manifest itself as a double pulse signature in the waveforms recorded by the DOM, if the time separation between the two showers is such that the two consecutive energy depositions both fit in the ATWD time window (422.3 ns) and do not overlap with each other. Fig. 6.2 shows a simulated double pulse waveform made by a ν_τ CC event.

A tau lepton has several decay modes. About 65% of the time, a τ decays to hadrons and a ν_τ; 18% of the time, a τ decays to an electron and a ν_τ, and 17% of the time, a τ decays to a muon and a ν_τ. The graphs below summarize the three decay modes mentioned above, with τ^- as an example. The same holds for a τ^+. IceCube cannot distinguish between τ^+ and τ^-.

$$\tau^- \rightarrow \nu_\tau + hadrons \ (64.8\%)$$
$$\tau^- \rightarrow \nu_\tau + \bar{\nu}_e + e^- \ (17.8\%)$$
$$\tau^- \rightarrow \nu_\tau + \bar{\nu}_\mu + \mu^- \ (17.4\%)$$

When a τ decays to hadrons or an electron, the second hadronic/electromagnetic shower from the hadrons or the electron will develop and deposit energy in the ice within tens of nanoseconds. When the τ decays to a muon, the outgoing muon will travel at the speed of light in the ice and emit Cherenkov light along the muon track, mimicking the signature of a ν_μ CC interaction. These features make the hadron and electron decay modes (BR $\sim$ 82%) more promising double pulse detection channels.

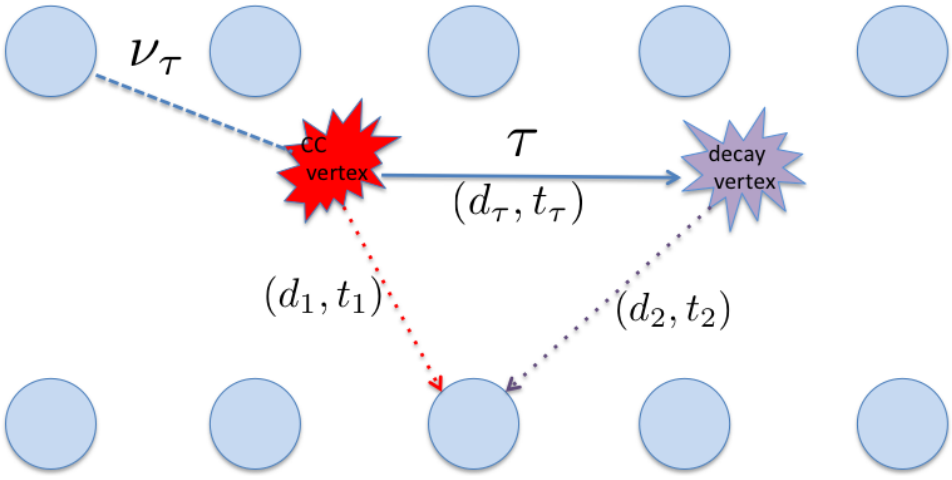

Figure 6.1: Sketch of a ν_τ undergoing CC interaction in the ice and the subsequent τ lepton decay, making the double bang. Blue circle indicates DOMs.

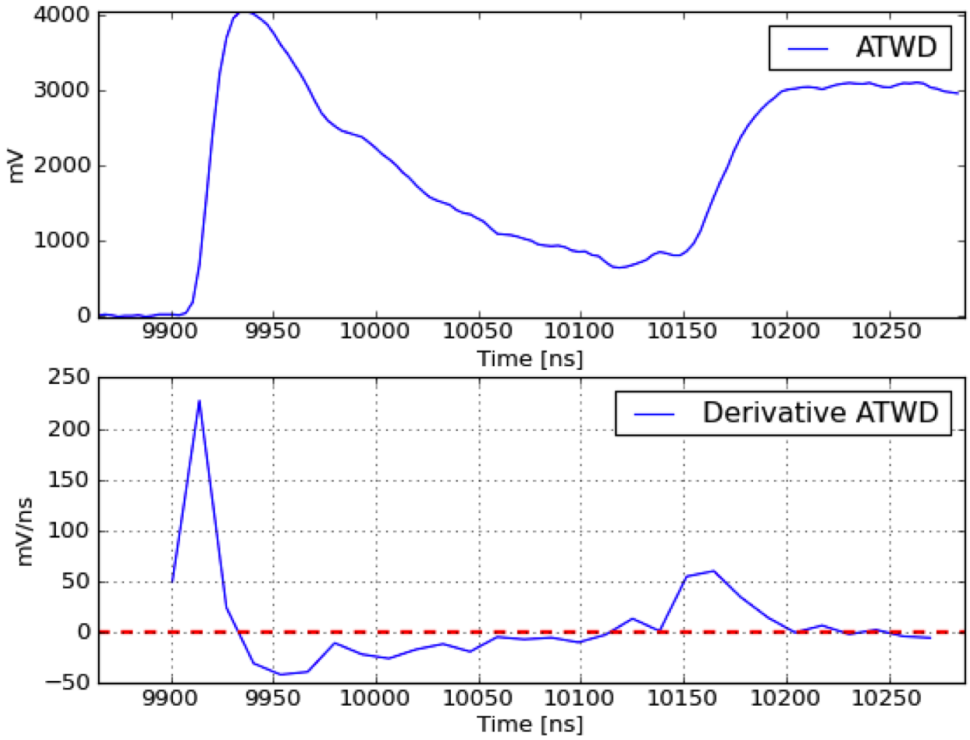

Figure 6.2: Top: a double pulse waveform made by a simulated ν_τ CC event. Bottom: first time derivative of the ATWD waveform from the top. The first derivative is used in the double pulse identification algorithm described later.

6.1 Double Pulse Waveform Characteristics

6.1.1 Signal: ν_τ

A double pulse waveform from a ν_τ depends on the optical properties of the ice as well as the relative energy and position of the ν_τ CC interaction and τ decay.

I begin with a selected sample of double pulse events from IceCube ν_τ simulation in order to investigate the relative amplitude, timing and shape of the two pulses. This led to the development of an algorithm for identifying double pulse waveforms.

To study the potential ν_τ double pulse events, a sample of ν_τ Monte Carlo simulation with energies between 1 TeV and 10 PeV was generated with an E^{-1} energy spectrum to maximize the statistics of high energy events. This sample is numbered 12345 according to the IceCube internal simulation database. A total of 10^6 events were generated for set 12345, with 35144

events triggering the detector. This sample was later reweighted to a more realistic E^{-2} spectrum for event rate estimation.

The hand-selected sample is made following two simple geometrical selection criteria based on Monte Carlo truth information:

- the time difference between unscattered photons from the first shower arriving at a nearby DOM and photons from the second shower arriving at the same DOM, $\Delta t_{arr} = |t_1 - t_2| = |\frac{d_2 - d_2}{V_{ice}}| > 100$ ns, where $V_{ice} = \frac{c}{n_{ice}}$ is the speed of light in ice, n_{ice}=1.36 is the refractive index of the Antarctic glacial ice at a wavelength of 400 nm. The error in distance from using a single wavelength refractive index is 3% compared to that from using full wavelength dependent refractive index [184]. As illustrated in Figure 6.1, d_1 and d_2 are distances from the CC vertex and decay vertex to the DOM respectively; t_1 and t_2 is the time for photons to travel distances d_1 and d_2 and register at the DOM.

- $d_1 <$200 m and $d_2 <$ 200 m. Any ν_τ CC event that has at least one DOM satisfying these criteria is considered as a potential double pulse event.

Figure 6.3 shows the $\Delta t = t_1 - t_2$ distribution ($\Delta t_{arr} = |\Delta t|$) on a waveform by waveform basis.

The first requirement ensures some reasonable timing separation between the two pulses. The second requirement ensures capturing the most direct light from the two cascades. Light arriving from larger distance is scattered, with the late light causing pulses to overlap. It turns out that most of the events satisfying the first requirement will satisfy the second automatically. The contribution from the second requirement is less than 2% of the total events that pass the geometrical requirements.

After performing the aforementioned selection, all selected events have primary ν_τ energies greater than 100 TeV, and with tau tack length (the distance over which a tau travels before decaying) greater than 10 meters. Typically, double pulse waveforms occur in DOMs within tens of meters of the neutrino interaction vertex.

A total of 493 raw events passed these geometrical selection criteria, which translates to $\sim$0.2 events per year based on a flux limit of $E^2\Phi_{\nu_\tau} = 1.0 \times 10^{-8}$GeV cm^{-2}s^{-1} sr^{-1} [1].

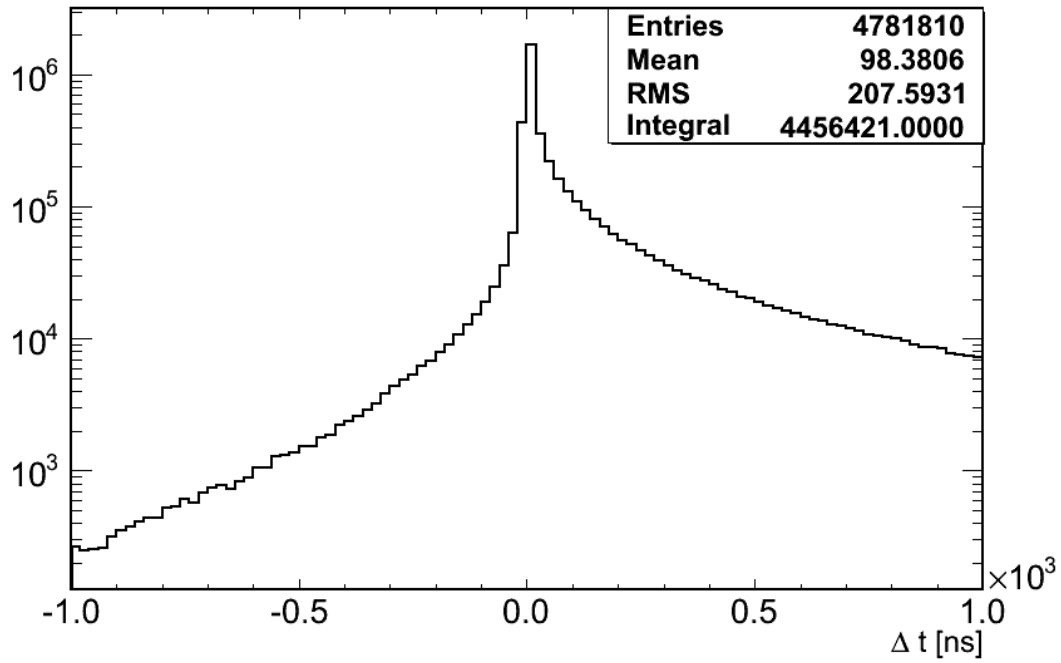

Figure 6.3: Time difference between photons from two subsequent cascades to a nearby DOM, ignoring scattering and absorption. The central peak of -100 ns $<\Delta t<$ 100 ns is where multiple pulses are indistinguishable and hence is cut out.

Among those 493 events, there are 655 DOMs (and hence 655 ATWD waveforms) which fulfill the geometrical cuts. More than 50% of the 493 candidate double pulse events have only one DOM passing the geometrical cuts. For those events with more than one DOM satisfying the geometrical requirements, all of them turn out to be on one string. The number of hit DOMs passing the double pulse requirement per event, or "NChannel", is shown in Figure 6.4.

About 270 out of these 655 waveforms have a visible double pulse feature. A double pulse algorithm was developed to automatically identify waveforms with a double pulse feature based on the 270 hand-selected double pulse waveforms.

6.1.2 Background

High energy muons from cosmic ray air showers and ν_μ CC events can also make a double pulse signature in the waveforms. For muons, the first pulse is from the Cherenkov light emission

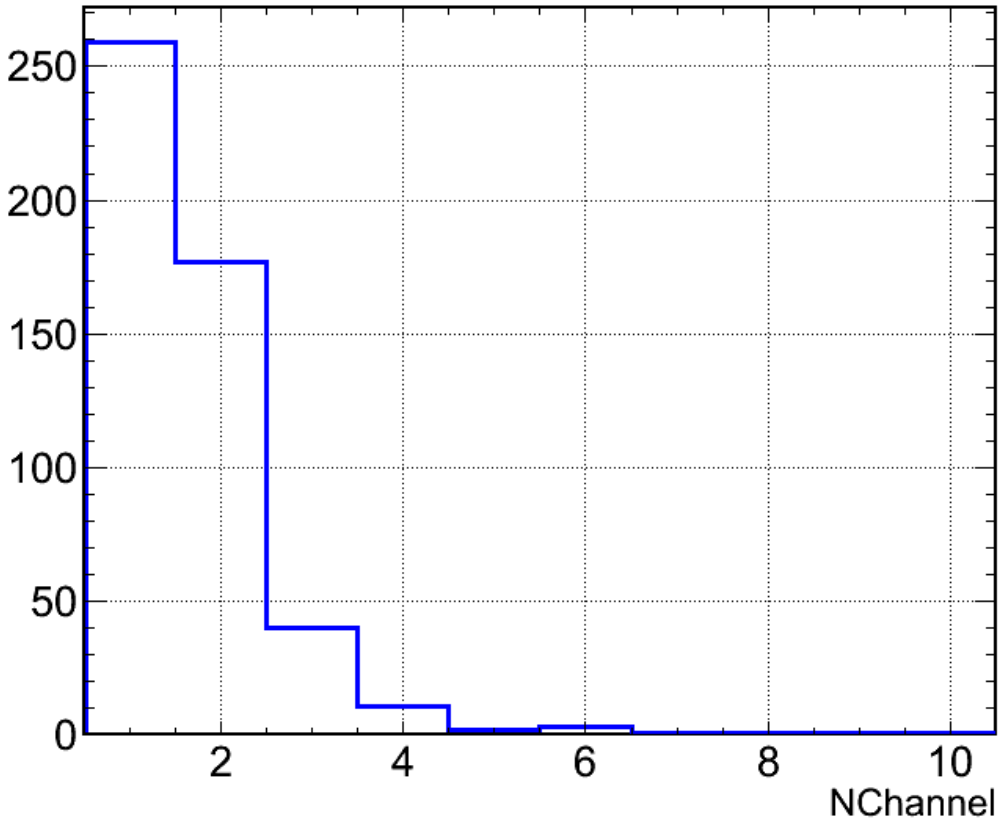

Figure 6.4: Distribution of number of hit DOMs (NChannel) per event that satisfying geometrical selection criteria. More than half of all double pulse events contain only one DOM that satisfies the selection criteria.

from the muon(s), while the second pulse usually is caused by TeV-scale stochastic energy loss (bremsstrahlung, pair production, nuclear interaction, etc) from the muon(s) within tens of meters of the DOM. A detailed study on the causes of double pulse waveforms from atmospheric muons is summarized in Appendix B.

For ν_μ CC interaction, the first pulse is from the CC interaction vertex, while the second pulse is also from the stochastic energy loss from the energetic outgoing muon.

Fig. 6.5 and Fig. 6.6 show double pulse waveforms from an atmospheric muon bundle event and a ν_μ CC event respectively.

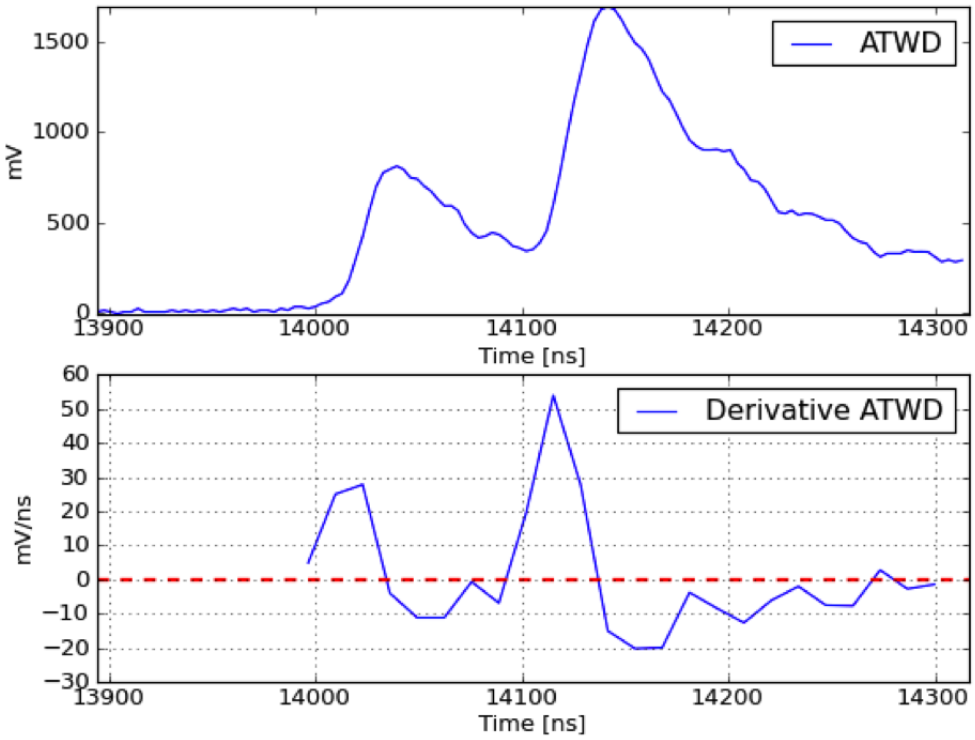

Figure 6.5: Top: a double pulse waveform made by a CORSIKA event (simulated atmospheric muon). Bottom: first derivative of the ATWD waveform from the top.

6.2 Double Pulse Waveform Identification Algorithm

The goal of the double pulse algorithm (DPA) is to identify waveforms with double pulse features that are consistent with a ν_τ double pulse waveform while rejecting waveforms with features that are consistent with late scattered photons from a single cascade event such as a NC or ν_e CC interaction. Since double pulse waveforms from atmospheric muon background events are very similar to those from a ν_τ, such events are eliminated at a later stage discussed in Section 6.3.2.

The DPA identifies events with at least one hit DOM that has a substantial double pulse feature which is consistent with two consecutive energy depositions near the DOM.

6.2.1 The Algorithm

The double pulse algorithm uses 7 parameters to characterize a waveform that has substantial double pulse features:

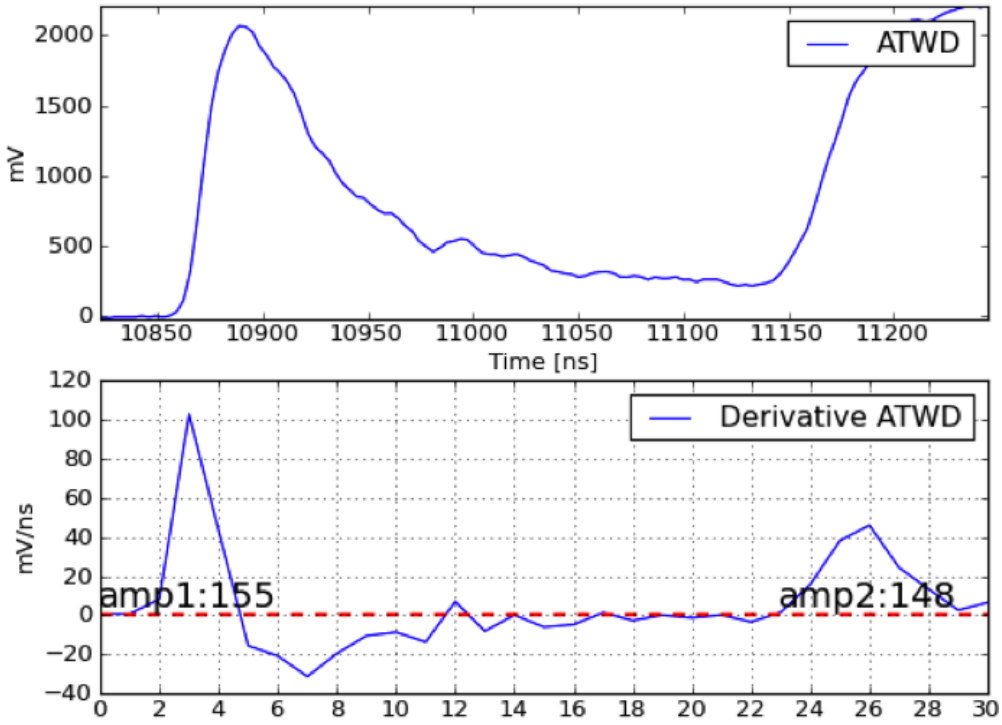

Figure 6.6: Top: a double pulse waveform made by a simulated ν_μ CC event. Bottom: first derivative of the ATWD waveform from the top.

- Waveforms from the ATWD digitizer in the lowest gain channel available are used, since higher gain channels are generally clipped for high-amplitude waveforms. The integrated amplitude is called **wf_qtot**. Waveforms with integrated amplitude less than 10000 mV·ns are rejected. With base impedance of 47 ohms and nominal gain of 10^7 [185], this translates to $\sim$ 432 PE. FADC waveforms are not used since they do not have multiple gain channels available and since they have coarser timing, causing double pulse features to be blended together or clipped.

- The beginning of the waveform is detected by a sliding time window of 3.3 ns equal to one ATWD bin size which searches for a monotonic increase in the waveform amplitude within a time span of 19.8 ns (6 ATWD bins).

- Once the beginning of the waveform is found, the waveform is divided into 13.2 ns segments (4 ATWD bins) and the first time derivative is calculated for each segment . The bottom panel

of Fig. 6.2 shows an example of an ATWD waveform derivative vector. The segment size is chosen to smooth the waveform.

- If the derivative is positive in at least two consecutive segments, this is considered the rising edge of the first pulse. The number of consecutive segments with a positive derivative for the first pulse is called **BinsToT1**. It is required that BinsToT1 ≥ 2. When the subsequent derivative is negative for two consecutive segments, this is considered the trailing edge of the first pulse. The rising edge of the first pulse is required to have an integrated charge, called **Amp1**, of at least 3.5 PE. The integrated charge sums up all the charge corresponding to the entire rising edge, which usually lasts longer than two segments (26.4 ns) for a big pulse.

- The second pulse rising edge is defined when the derivative after the trailing edge of the first pulse is positive again for three consecutive segments. The number of consecutive segments with a positive derivative for the second pulse is called **BinsToT2**. It is required that BinsToT2 ≥ 3. This requirement is due to the fact that the photons that make the second pulse are often more scattered and therefore the second pulse usually has a less steep rising edge than the first pulse. The second pulse trailing edge is often outside the ATWD time window, and is therefore not calculated. The rising edge of the second pulse is required to have an integrated charge, called **Amp2**, of at least 6.3 PE.

The development and optimization of the DPA took place in two stages. With the originally rather loose model-independent settings, the DPA is designed to pick up as many signal events as possible. At this signal-driven stage, the DPA is able to pick up 287 waveforms from the 665 waveforms from the hand-selected event sample. More than 90% of the 288 waveforms show substantial double peak features. A few percent of the selected waveforms have a weak second pulse with parameters near the setting thresholds. The DPA with these settings was presented in the 33rd International Cosmic Ray Conference (ICRC) held in Rio de Janeiro, Brazil in July 2013 [151].

So far only 6 parameters are used in the double pulse waveform identification. Another parameter was calculated but not used: integrated charge of the trailing edge, called **AmpTrailing**.

After the ICRC, the algorithm was further run on various data samples for performance tests and re-optimized (tightening the configurable parameters) to further eliminate the weak double pulse waveforms that are usually caused by late scattering from energetic single cascades typically from ν_e CC events and NC events of all three flavors. This re-optimization stage is purely 'background-driven'. A cut on **AmpTrailing** of at least 6.0 PE was added. The performance tests and optimization of DPA are summarized in the next section.

6.2.2 Performance Tests and Optimization

DPA performance tests were done on both neutrino Monte Carlo samples and data from an in-ice laser module with absolutely calibrated light output, the 'Standard Candle' (SC).

Neutrino Monte Carlo Samples

As mentioned in the previous sections, we know that track-like backgrounds (atmospheric muons and ν_μ CC events) can make double pulse waveforms similar to those from ν_τ CC events. However, those track-like backgrounds have distinctive event topologies from ν_τ CC events. Therefore, we aim to eliminate weak double pulse waveforms from cascade-like events (ν_e CC and NC events of all flavors) at waveform level, and remove track-like backgrounds at event level.

Data samples used in the tests include ν_τ, ν_e and ν_μ Monte Carlo samples from IceCube standard simulation productions. The ν_τ sample was simulated with primary neutrino energies ranging from 1 TeV to 10 PeV, and the sampling energy spectrum is E^{-1}. A total of 10^6 ν_τ events were generated, with a few percent of them triggering the detector. The background samples of ν_μ and ν_e were with primary neutrino energies ranging from 10 GeV to 10^9 GeV, with an energy spectrum of E^{-2}. There are 2×10^9 events generated for each sample. Ideally, the background samples and signal sample should have the same energy spectrum. An E^{-1} energy spectrum evidently samples more high energy events than a E^{-2} spectrum, given the same number of events generated at the same energy range. At the time the DPA was being developed and optimized, there were no E^{-1} ν_μ or ν_e simulations available. However, the ν_τ sample has a neutral current (NC) component which could give some guideline on the DPA performance on cascade-like events at higher energies. The

DPA settings are tightened to eliminate waveforms from the cascade-like events, and those settings are summarized in Table 6.1:

Parameters	Published in ICRC	Currently Employed
wf_qtot	>10,000 mV	>10,000 mV
BinsToT1	2	2
BinsTbT	2	2
BinsToT2	3	3
Amp1	> 10 mV/s	>10 mV/s
AmpTrailing	–	<-17 mV/s
Amp2	>10 mV/s	>18 mV/s
Comments	'Signal-driven'	'Background-driven'

Table 6.1: DPA setting parameters published in the 2013 ICRC proceedings [151] and settings used in the final analysis.

DPA performance on cascade-like events from the aforementioned Monte Carlo samples are summarized in Table 6.2.

Event Types	No. of Double Pulse Waveforms (DPA settings published in ICRC)	No. of Double Pulse Waveforms (DPA settings currently employed)
ν_τ CC	288	220
ν_τ NC	26	4
ν_μ NC	7	0
ν_e	309	$2 \rightarrow 0$

Table 6.2: DPA performance on waveforms from ν_τ CC events (signal) and cascade-like background events

Among the 220 double pulse waveforms from the ν_τ CC sample, 80% are double pulse waveforms clearly visible by eye as shown in Fig. 6.2. About 20% have a relatively weaker second pulse by eye, mostly due to overlapping with a very energetic first pulse, as shown in Fig. 6.7.

There is no physical process to produce substantial double pulse waveforms in single cascade events such as ν_e CC events and NC events of all flavors. Two of the 4 double pulse waveforms from the ν_τ NC sample are extremely energetic single pulse waveforms with long bumpy trailing edges due to late photon scattering. The other two are double pulse waveforms where the second

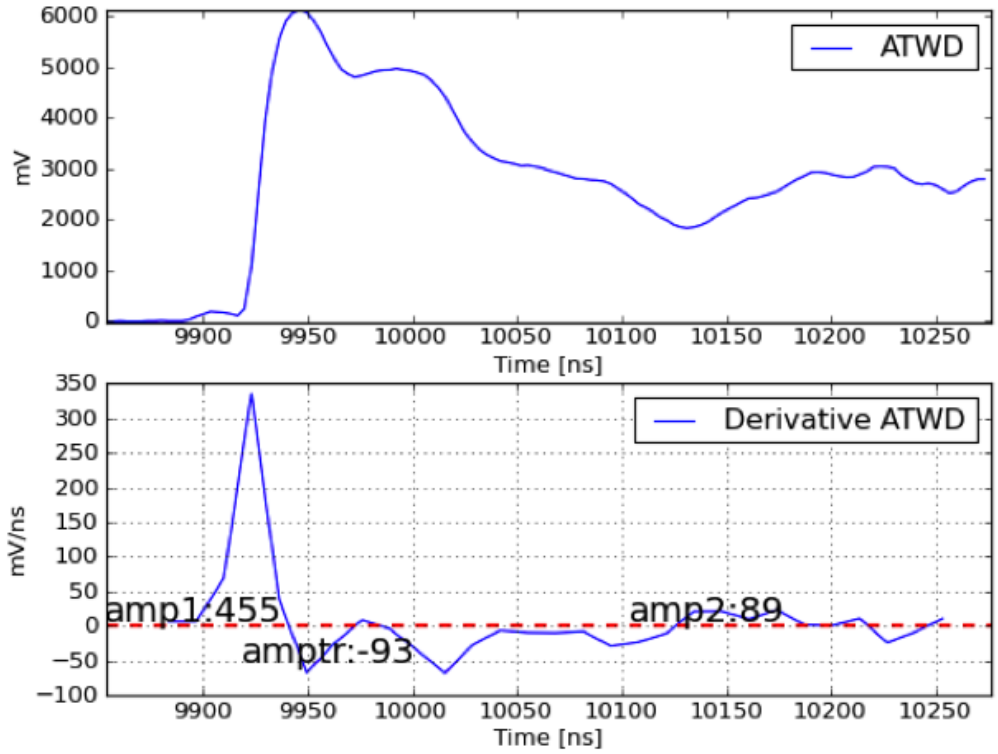

Figure 6.7: Top: a double pulse waveform made by a simulated ν_τ CC event. Bottom: first derivative of the ATWD waveform from the top.

pulse is a simulated late pulse from the PMT (more details on these waveforms in Chapter 4). IceCube simulation of late pulse shape does not match the data well, so events where a late pulse trigger the DPA are only seen in simulation. Fig. 6.8 shows examples of these two categories of waveforms.

With the current DPA settings, misidentified double pulse waveforms in the ν_e samples drop from 309 to 2. These two waveforms are from one Glashow resonance event $\bar{\nu}_e e \rightarrow \bar{\nu}_\mu \mu$, with the energetic outgoing muon causing two double pulse waveforms in two adjacent DOMs. Fig. 6.9 shows the two double pulse waveforms from a Glashow resonance event. The maximum primary neutrino energy in the electron neutrino simulation is 100 PeV, therefore cascade elongation due to the LPM effect is not expected to be a significant factor in event rate estimation. Therefore, essentially no double pulse waveforms from ν_e single cascade events survived the new DPA settings.

The DPA was re-tested with new ν_e and ν_μ Monte Carlo samples with E^{-1} energy spectrum

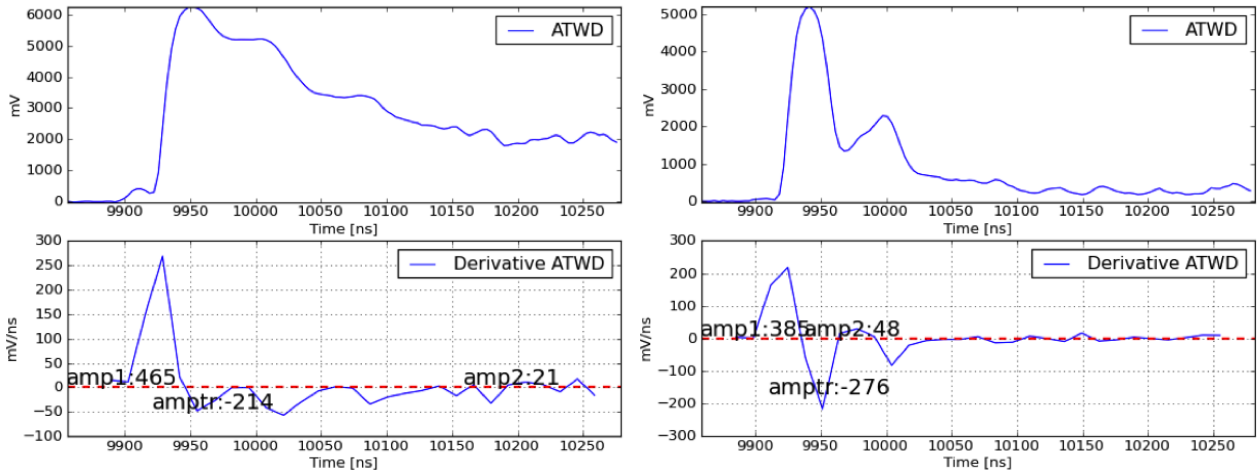

Figure 6.8: Left: single energetic waveform from a simulated ν_τ NC event with long bumpy trailing edge that was identified as double pulse by DPA. Right: single energetic waveform from a simulated ν_τ NC event with second pulse being late pulse responding to the saturated first main pulse. Late pulses in data have a different (smoother) shape and do not trigger the DPA.

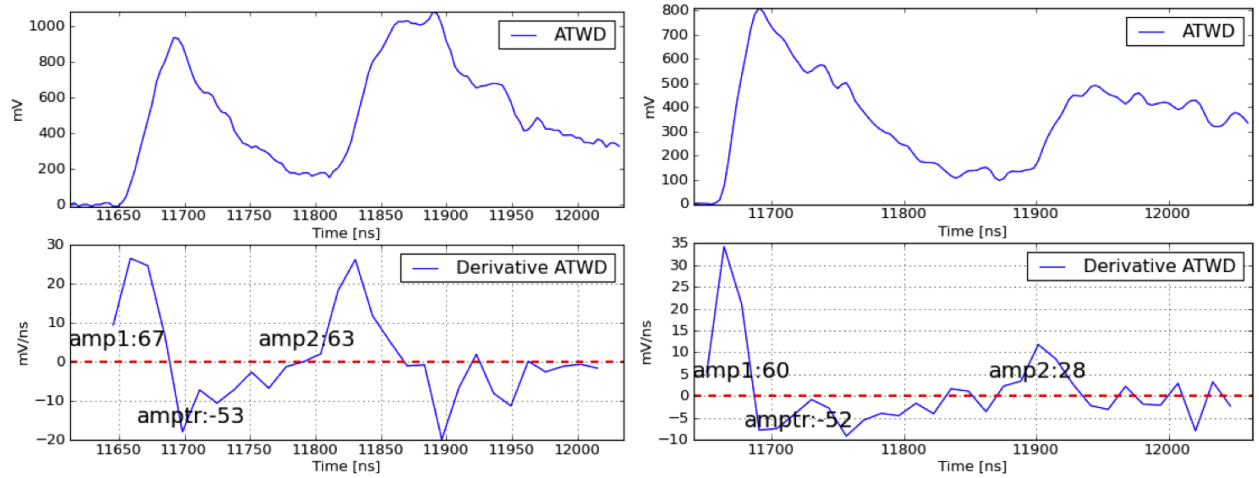

Figure 6.9: Left: double pulse waveform from a Glashow resonance event simulated $\bar{\nu}_e e \rightarrow \bar{\nu}_\mu \mu$ from OM (39, 51). Right: double pulse waveform from the same Glashow resonance event $\bar{\nu}_e e \rightarrow \bar{\nu}_\mu \mu$ from OM (39, 52).

when they became available months later. The E^{-1} samples have many more high energy events simulated than the E^{-2} samples, and hence more double pulse waveforms are identified from those newer samples. However, the total (misidentified) double pulse event rates from these cascade-like backgrounds are nearly two orders of magnitude lower than the event rates from signal. This indicates that the optimization of DPA settings are extremely efficient in cascade-like background

control. Detailed event rates are discussed in Section 6.5.

Standard Candle Data

The response of IceCube at high energies is calibrated using an in-ice light source called the 'Standard Candle' (SC). The SC is an nitrogen laser module with a wavelength of 337 nm. The output photon numbers of the SCs can range from 10^{11} to 10^{13} which is equivalent to the energy of ν_e from 1 to 100 PeV. The SC is useful in estimating energy scale uncertainties at extremely-high-energy (EHE) range, including detector response to bright light and the ice properties. In comparison with Monte Carlo, the energy scale uncertainty of the detector is estimated to be $\sim$20%.

There are currently two Standard Candles deployed within the IceCube detector PMT array. Fig. 6.10 shows the relative locations of the two SCs: SC1 points upward at the depth of 1800m, while SC2 points downward at the depth of 2000 m which is just below the big dust layer. The light intensity of the SCs can be varied with different filters with transparencies ranging from 0.5% to 100%. The recorded total number of photoelectrons (NPEs) is on the order of 10^5 to 10^6. Table 6.3 summarizes some filter settings and the associated measured intensities of data.

Table 6.3: Standard Candles filter settings and associated measured intensities of data.

SC Settings	Nominal Photon Input	Total NPE
SC2: 100%	2.5×10^{13}	$10^{5.8}$
SC2: 10%	2.1×10^{12}	$10^{5.2}$
SC2: 1%	3.5×10^{11}	$10^{4.7}$
SC1: 50%	2.2×10^{12}	$10^{5.1}$

Further tests on the optimized DPA settings were carried out on some bright Standard Candle II (SC2) data samples with various brightness outputs. The DPA with optimized settings was run on a total of 7369 SC2 events with various SC2 filter settings. All these events pass the IceCube EHE filter. About 35% (2551 events) passed the DPA ICRC settings, while only $\sim$0.4% (32 events with one double pulse waveform per event) passed the optimized settings. Table. 6.4 summarizes DPA performance on SC2 data samples with various filter settings.

Waveforms from the SC2 data samples that passed the DPA can be categorized into two groups.

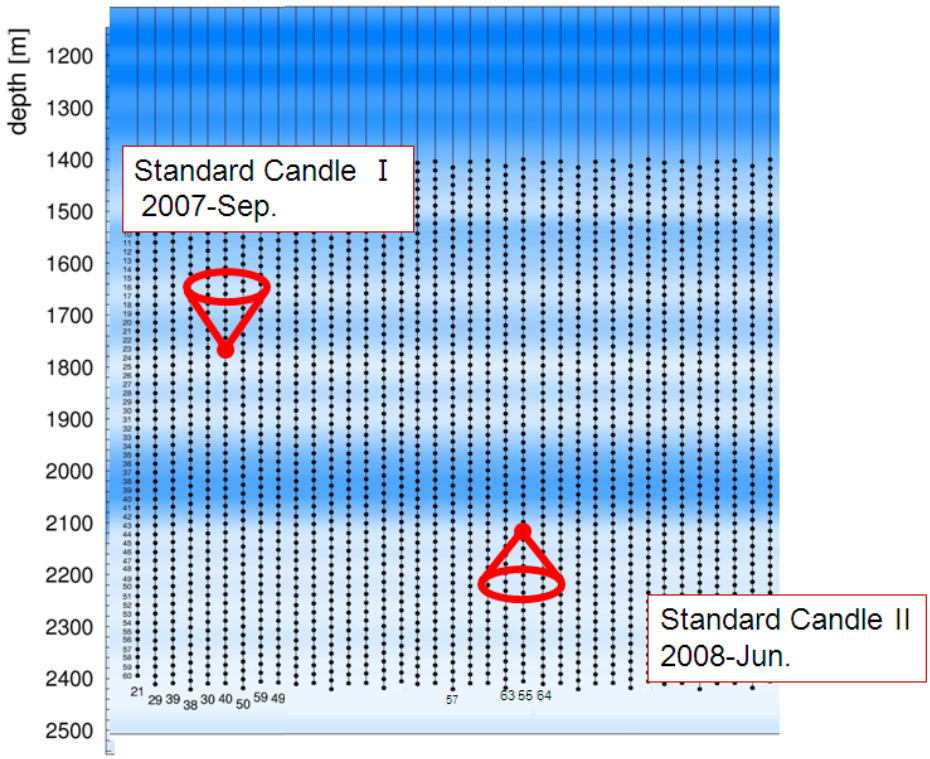

Figure 6.10: Standard Candle locations in IceCube.

The first group are waveforms from DOM 42 on String 55 which is located right above SC2. Five out of 20 double pulse waveforms with 100% intensity and 2 out 5 of the double pulse waveforms with 51% intensity fall into this group. The other group are double pulse waveforms from nearby DOMs, which could be on the same string as SC2 but with DOMs well above/below SC2, or DOMs from different strings. The two groups of waveforms have very distinctive shapes, as demonstrated in Fig. 6.11. Waveforms from the first group exhibit substantial rapid fluctuations while waveforms from the second group are smoother. The reason for these behaviors is largely due to the pointing direction of SC2 which is located between DOMs 42 and 43 on String 55 and facing downwards. In the case where there is one DOM above, the light can take two extreme paths to get from SC2 to the DOM: 1) immediately be scattered upwards and detected by the DOM 2) Undergoing multiple scatters until it comes around 180 degrees and is detected by the DOM. The variations between these two extremes introduces multiple pulses in the waveform. This would also be true for DOMs more than one DOM above but to a lesser extent due to longer distance for scattering.

Intensity[1]	No. of EHE events	No. of events (ICRC settings)	No. of events (current settings)	No. of DP waveforms (current settings)
1%	1162	48	0	0
3%	1467	118	0	0
10%	1219	138	7	7
30%	1349	567	0	0
51%	1261	783	5	5
100%	941	897	20	20

Table 6.4: DPA performance on Standard Candle II data samples with various nominal intensities.

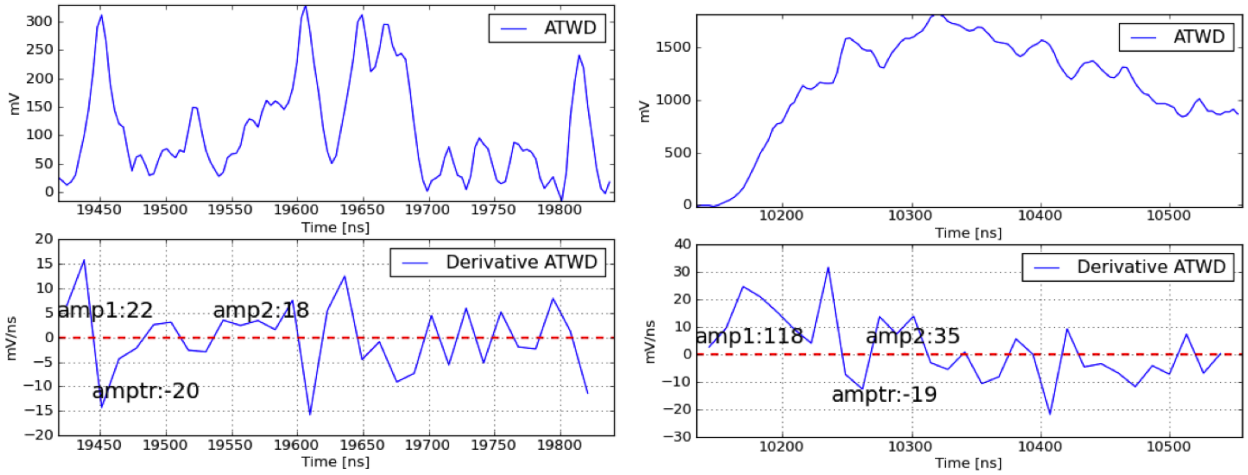

Figure 6.11: Left: an example double pulse waveform from a SC2 event from OM(55, 42) which is located right above SC2. Right: an example double pulse waveform from nearby DOMs other than OM(55, 42).

I decided that no further optimization on DPA should be done based on the SC2 data for the following reasons:

- The current DPA settings optimization is driven by single energetic cascades (ν_e and NC events of all three flavors) and they are quite efficient in filtering out bright SC events (single cascades) already.
- More importantly, SC light is monochromatic (337 nm), while Cherenkov light from neutrino interactions is multi-chromatic.

[1]Nominal intensity

6.3 Double Pulse Event Selection

Event selections begin with the IceCube offline data stream, following the EHE filter. The final event selection was done through three levels of cuts, each of which was dedicated to achieve specific background rejection goals.

6.3.1 Data Samples

Data samples processed during cut development (before unblinding) include three flavors of neutrino simulation, atmospheric muon simulation and 10% of real data (the "burn sample"). Once the event selection criteria are finalized, they are applied intact to the remaining 90% of data (the "blind sample").

ν_τ simulation - Two samples of ν_τ simulations are employed in this analysis, sample 12345 introduced in Section 6.1.1 and sample 10099 with higher statistics and covering a larger energy range. Set 10099 was simulated with a E^{-1} energy spectrum from 1 TeV to 10^9 GeV. A total of 5×10^6 events were generated with $\sim$10% triggering the detector. Figure 6.12 shows the τ length distribution which is the distance a τ lepton travels before it decays. In the dominant τ hadronic decay mode, some approximation has been made during the simulation implementation [159], see approximation details discussed in Section 5.3.1. Figure 6.13 plots the ratio of the hadronic decay energy over the τ lepton energy.

ν_μ simulation - The ν_μ Monte Carlo sample used in the event selection stage was simulated with the primary neutrino energies ranging from 100 GeV to 10^8 GeV, and with an energy spectrum of E^{-1}. A total of 9.95×10^6 events were generated with $\sim$4% triggering the detector.

ν_e simulation - The ν_e Monte Carlo sample used in the event selection stage was simulated with the primary neutrino energies ranging from 100 GeV to 10^8 GeV, and with an energy spectrum of E^{-1}. A total of 2.5×10^6 events were generated with $\sim$7% triggering the detector.

CORSIKA simulation - CORSIKA Monte Carlo samples used in this analysis are all 5-component CORSIKA (see Section 5.3.2 for more details). The physics parameters of these samples are summarized in Table 6.5. All samples are combined following the weighting scheme introduced in

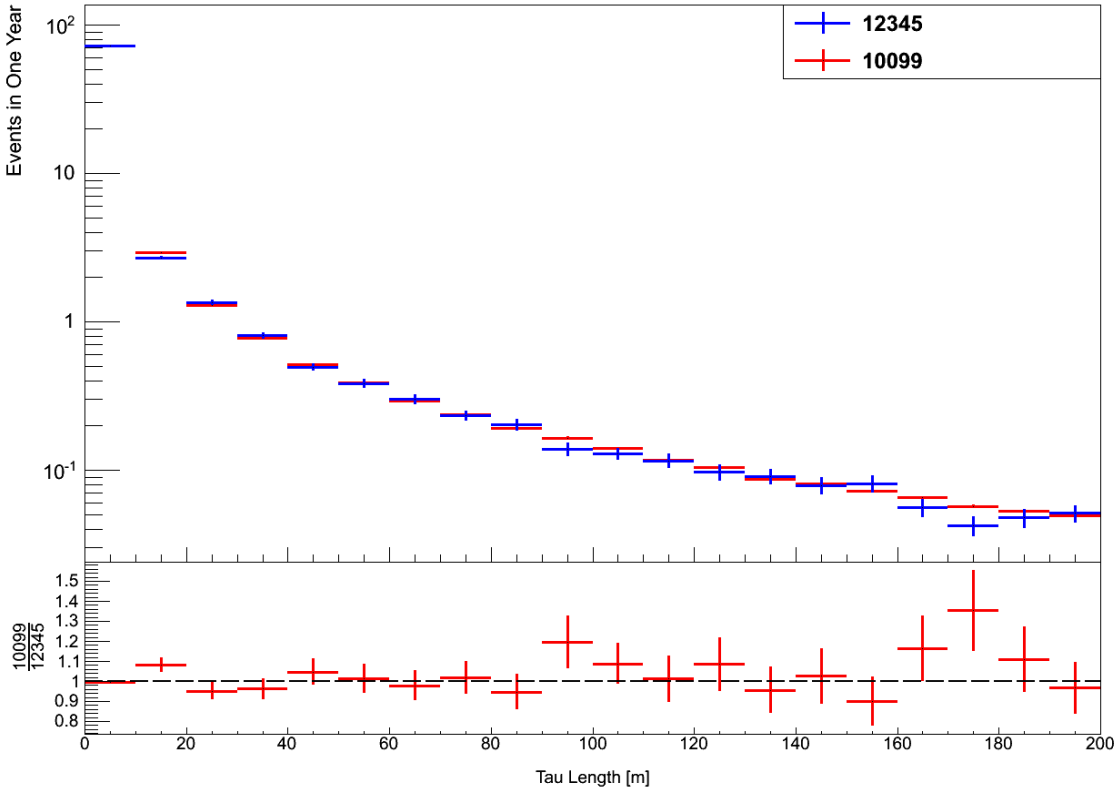

Figure 6.12: The distance a τ lepton has traveled before it decays in simulated IceCube ν_τ events.

Section 5.3.2.

Burn sample and blind sample - This analysis uses three years of data from IceCube instrumented with 86 strings. Data was collected from May 13, 2011 to May 6, 2014. IceCube divides data taking into runs with 8 hours per run. About 10% of the data is used for cut development along with the aforementioned Monte Carlo samples, the remaining 90% of the data is kept blind to minimize bias. The burn sample consists of every 10th run. This selection rule ensures that the burn sample spans the whole data period considered. Both the burn and blind data samples used in this analysis exclude partial runs where not all strings were collecting data, usually during short detector maintenance periods. This results in a total livetime of 97.9 days for the burn sample, and 914.1 days for the blind sample. The total good uptime (excluding partial runs) for the blind sample in three years is 92.3%. Figure 6.14 shows average event rates per run versus run numbers for the first year of the burn sample.

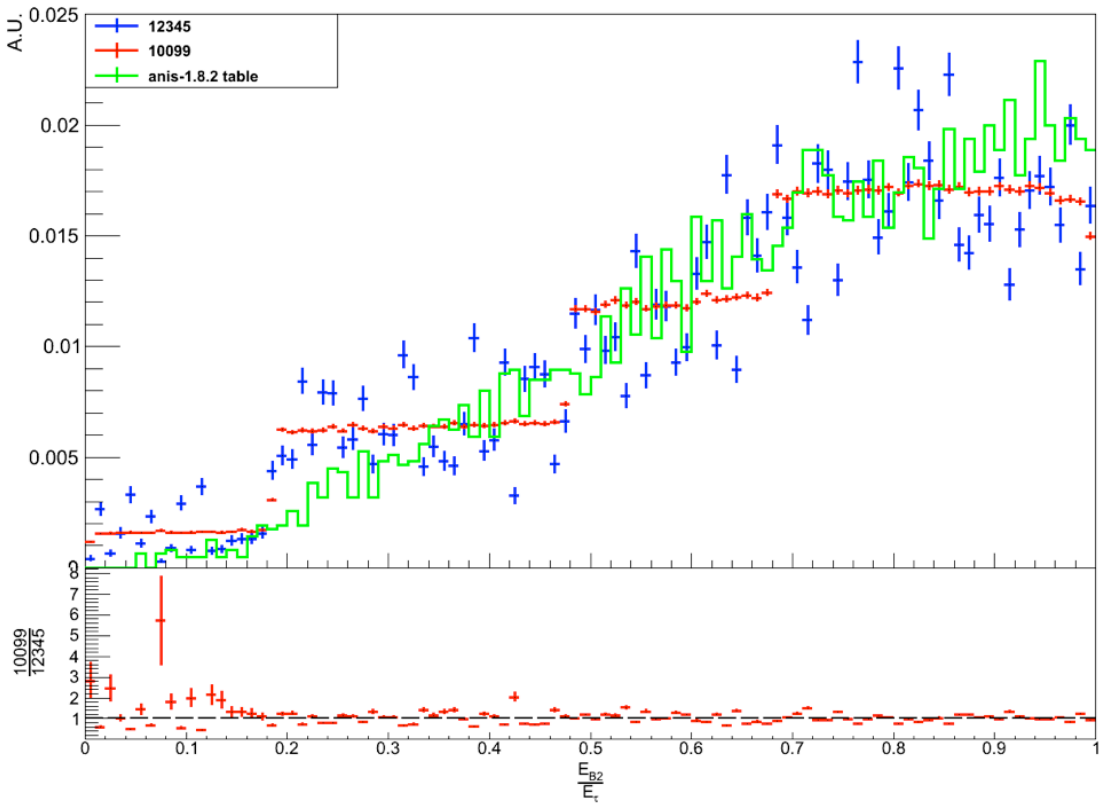

Figure 6.13: Ratio of tau lepton decay vertex energy (sum of hadrons) over tau lepton energy with arbitrary unit.The ANIS data points plotted in green are from the TAUOLA tau decay library [186]. The stepwise feature is due to tau lepton decay approximation implemented in the lepton propagator MMC [159].

6.3.2 Cut Variables

Before deciding which filter stream to use, the DPA was run on the aforementioned ν_τ set 12345 and selected a sample of ν_τ CC double pulse events. These ν_τ CC double pulse events all turned out to have event-wise charge QTot>1000 PE, and hence the EHE filter was chosen. The QTot distribution is shown in Figure 6.15, and the three level of cuts are summarized as follows:

Level4: Identifying Events with Double Pulse Waveforms

Level4[3] is the first cut level, it includes three cut parameters:

[2]IceCube internal Monte Carlo naming scheme, usually larger numbers indicate newer datasets.

[3]Data stream naming convention in IceCube usually follows the following scheme: level1 refers to online data stream at the South Pole; level2 is offline data stream after filtering and with minimum low level reconstructions;

Datasets[2]	Geometry	Energy Spectrum	E_{min}	E_{max}	No. of Simulated Showers
9255	IC86	E^{-2}	100 TeV	10^{11} GeV	3×10^{9}
10309	IC86	E^{-2}	100 TeV	10^{11} GeV	4.3×10^{8}
9036	IC86	$E^{-2.6}$	600 GeV	100 TeV	1.0×10^{12}
9507	IC86	$E^{-2.6}$	600 GeV	100 TeV	1.0×10^{10}
9622	IC86	$E^{-2.6}$	600 GeV	100 TeV	1.0×10^{12}
6514	IC79	E^{-2}	600 GeV	10^{11} GeV	2.5×10^{12}
7017	IC79	E^{-2}	600 GeV	10^{11} GeV	2.5×10^{12}

Table 6.5: CORSIKA datasets used in the analysis.

- EHE filter (equivalent to log10(QTot)>3.0)
- log10(QTot)> 3.3. An increase in the event-wise charge cut is chosen because it retains more than 99.9% of signal events while moving away from the larger atmospheric muon background at lower energies. Figure 6.16 shows event-wise total charge distributions for data and MC samples at level4.
- Double pulse algorithm. This requires that at least one DOM in the event must pass the DPA.

Since atmospheric muon events with double pulse waveforms do not occur very often ($\sim$ 6 per day), about three orders of magnitude data reduction is achieved at this level compared to EHE filter level.

Figure 6.18 and 6.19 summarize the CORSIKA rates and effective livetime as a function of primary energy at level4.

Level5: Removing Track-like Backgrounds

Level4 selects events with double pulse waveforms called double pulse events, the majority of which are very bright cosmic ray induced track-like muons. However, the ν_τ double pulse events

level3 refers to the lowest physics analysis level which is related to some specific physics group such as the cascade working group. The first cut level of this analysis is named level4 to avoid confusion with the IceCube conventional data stream naming.

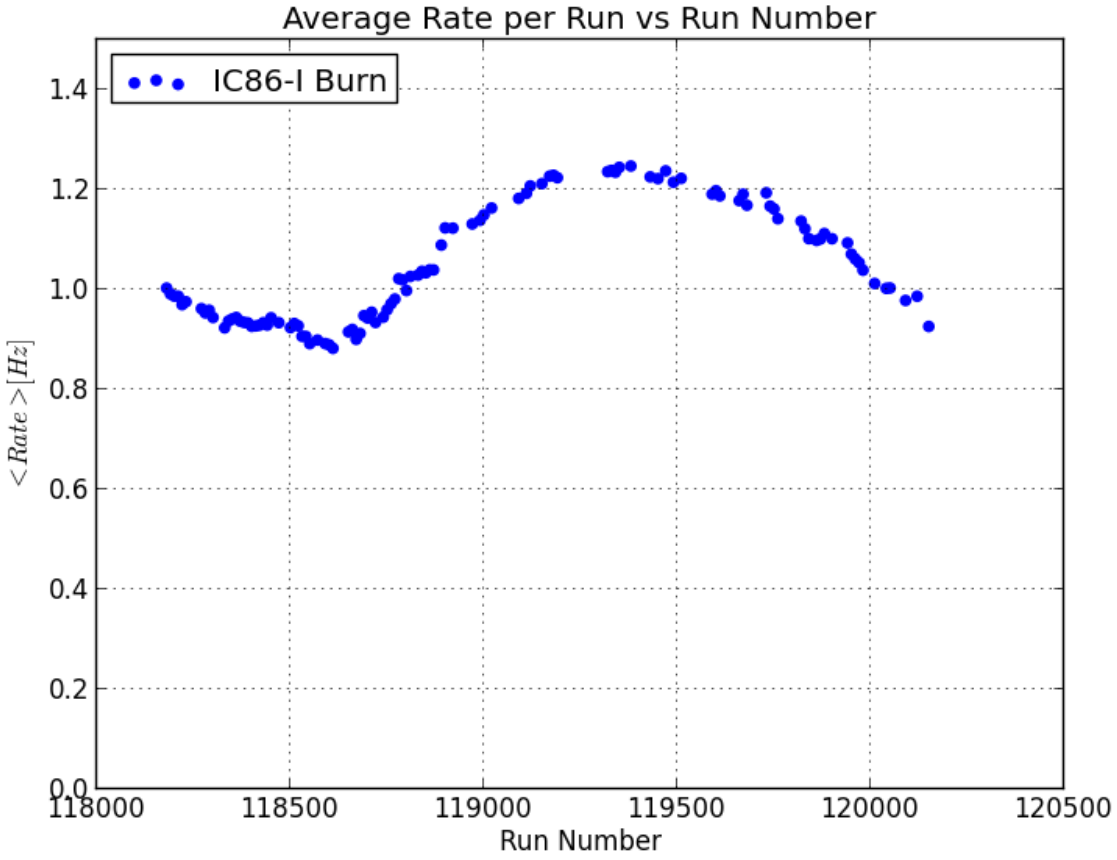

Figure 6.14: Average rates versus run numbers for the first year of burn sample in the EHE filter stream (without any analysis cuts). The increment of run numbers corresponds to time increment from May 13, 2011 to May 15, 2012. The modulation of the rates is due to seasonal variation of the atmosphere.

are mainly cascade-like. Therefore, the cuts at this level focus on removing track-like backgrounds.

Level5 cuts include:

- rllhratio<0. The rllhratio is defined as the ratio of reduced log-likelihood of a simple cascade reconstruction (**CascadeLLH**, discussed in Section 5.4.3) over the reduced log-likelihood of a simple track reconstruction (**SPE32**, discussed in Section 5.4.2). Events with rllhratio<0 are more cascade-like.

- firstHitZ<460 m. This cut requires the first hit in time of an event must begin at least 40

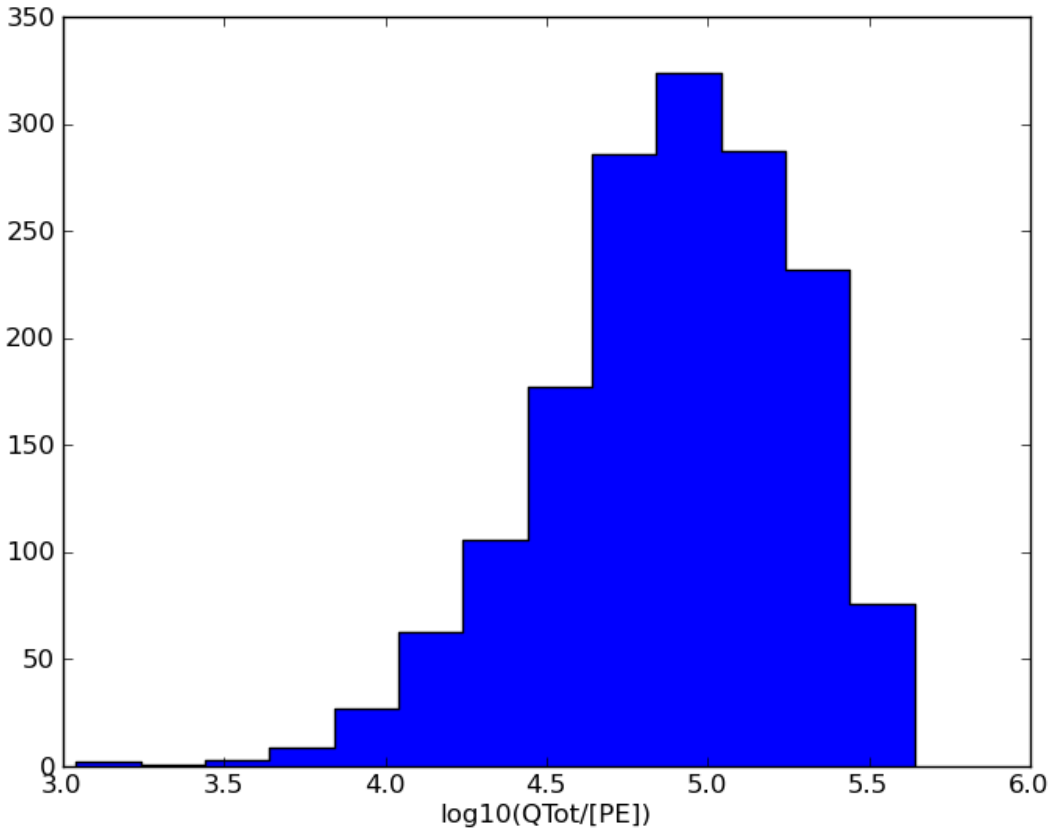

Figure 6.15: Event-wise charge for ν_τ CC double pulse events at all filters. Y-axis is event counts without weighting.

meters below the very top layer of DOMs, z=500 in the IceCube coordinates. Down-going atmospheric muons are very likely to leave light in the top layers as they are streaming through the detector from above, hence this cut largely removes those bright down-going muons.

In summary, this set of cuts selects cascade-like double pulse events which occur at least 40 meters below the top layer of the detector. Figure 6.20 and Figure 6.21 show the distribution of cut variables rllhratio and firstHitZ.

A total of 6 raw (without weighting) CORSIKA events and 0 burn sample events survive after applying level5 cuts. Among the 6 CORSIKA double pulse events, four are from IC86 set 9255

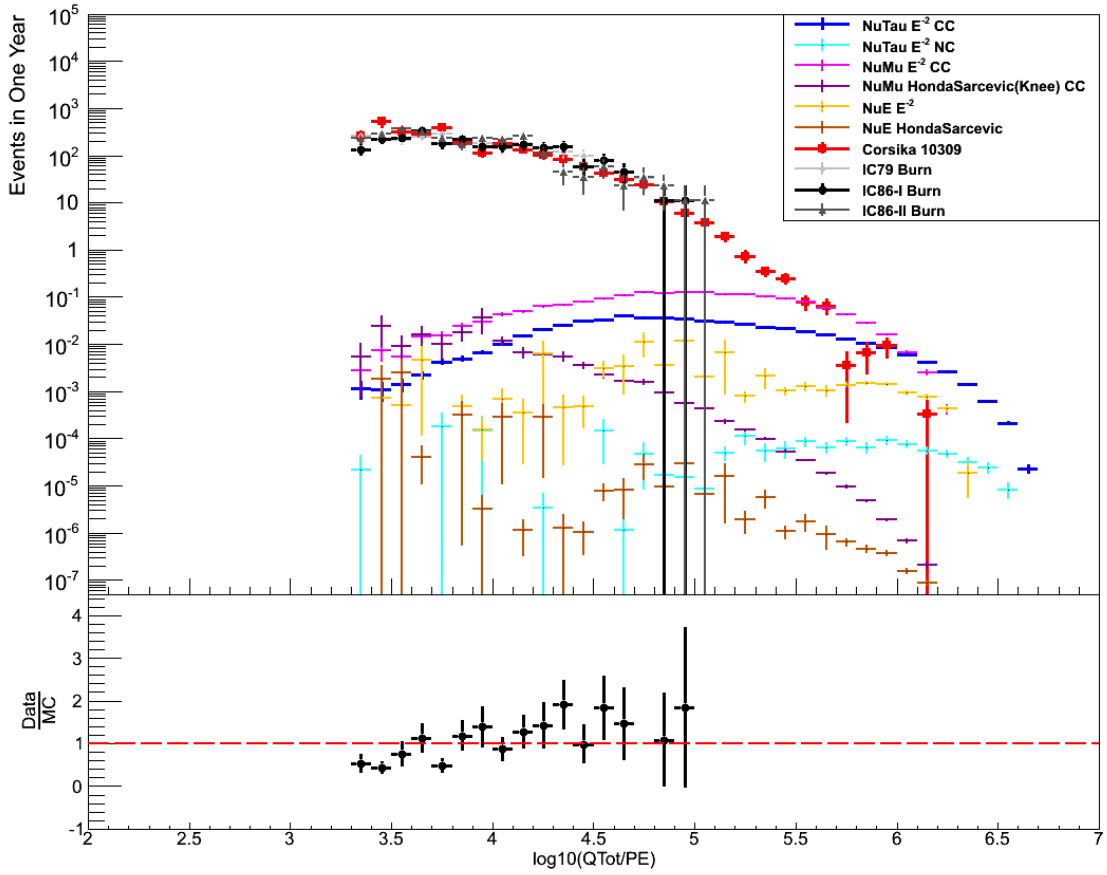

Figure 6.16: Event-wise charge for various data samples. Color codes are as follows: red: CORSIKA, dark/grey circles: burn samples, blue: ν_τ CC, magenta: astrophysical ν_μ CC, purple: atmospheric ν_μ CC, cyan: astrophysical ν_τ NC. Orange: astrophysical ν_e, brown: atmospheric ν_e. CORSIKA rates are weighted to a flux predicted by [187]. The bottom panel shows the ratio of burn sample rates from first year over rates from CORSIKA.

and two from IC79 set 6514. All 6 raw CORSIKA events are cascade-like down-going atmospheric muons clipping the top and botom corner of the detector, called "corner-clippers". Due to systematic concerns about the difference between 79-string and 86-string IceCube data, the two raw IC79 CORSIKA events are used only for further containment cut development, they are not included in CORSIKA rate estimation. Among these 6 double pulse corner-clippers, 5 of them have only one double pulse waveform (DP NCh equals to 1). One of the two IC79[4] DP corner-clippers has two double pulse waveforms (DP NCh equals to 2) from adjacent DOMs on the same string. Event-wise views and associated double pulse waveforms of these 6 events are shown in Appendix A.3.

[4]IC79: the 79-string data from IceCube construction phase 2010-2011.

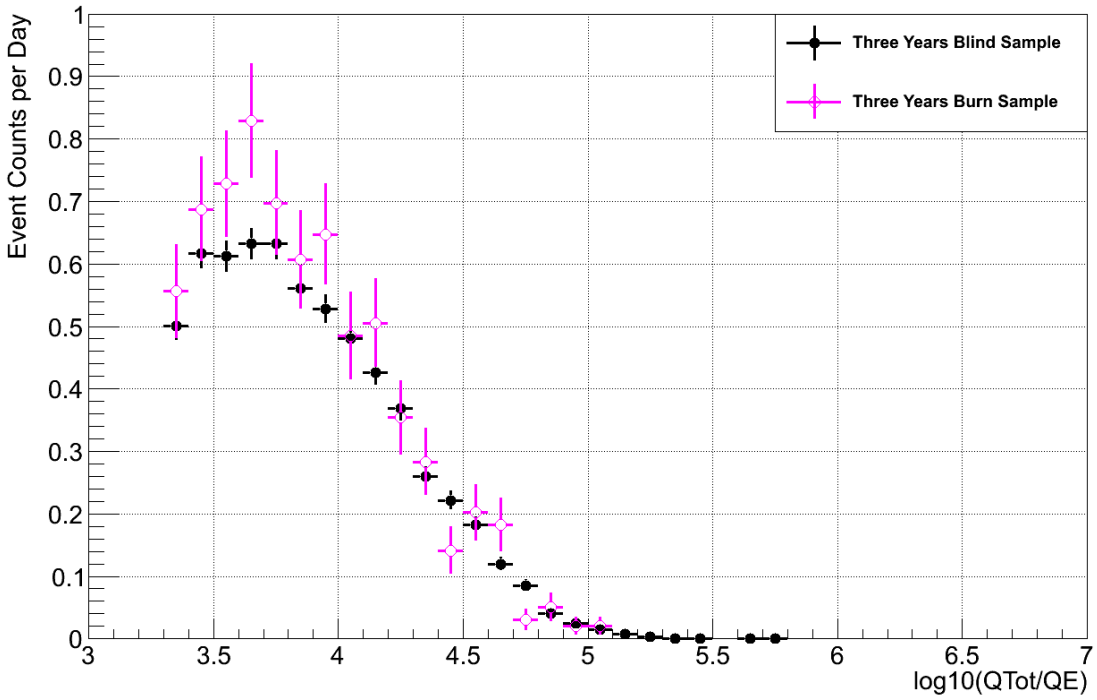

Figure 6.17: Event-wise charge QTot distribution for both burn sample and blind sample at level4.

A study on an event-by-event basis of the causes for atmospheric muon double pulse waveforms is summarized in Appendix B.

Level6: Eliminating Corner-clippers

After level5 cuts, the dominant surviving background events are corner-clippers. To eliminate the corner-clippers, a containment cut is necessary.

A more sophisticated cascade reconstruction algorithm (**Monopod**, discussed in Section 5.4.3) was run on all the remaining events to calculate their position with better precision. The detector boundary is defined as a polygon connecting the outermost strings. Before making the containment cut, a new variable named **least distance to polygon edges** is defined based on the reconstructed event vertices. Figure 6.22 shows the variable of least distance to polygon edges.

The containment cut is then made on a 2D plane of the reconstructed Z position versus the least

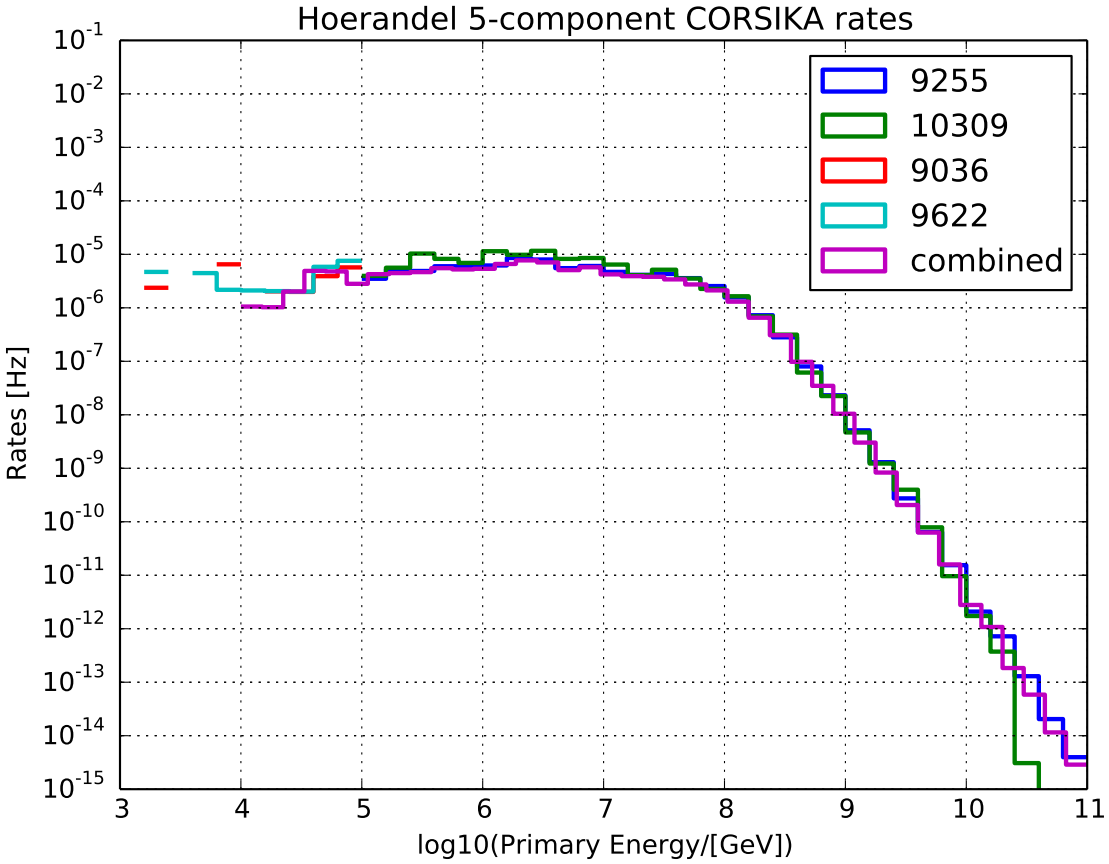

Figure 6.18: CORSIKA rates as a function of primary energy at level4. The combined rate from all the samples is calculated using the method introduced in Section 5.3.2.

distance from the reconstructed vertex a certain event has to the detector polygon edges. Denote y-coordinate as z and x-coordinate as ld and as illustrated in Figure 6.23, the containment is defined

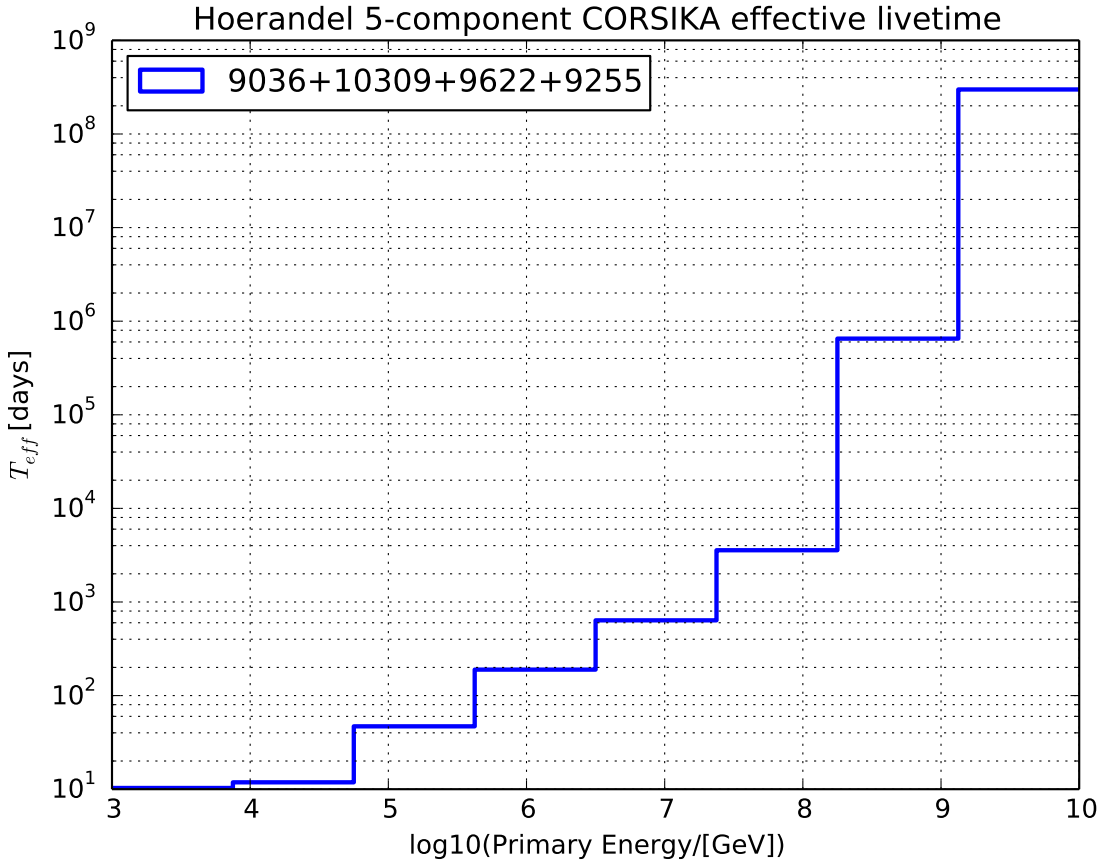

Figure 6.19: Combined CORSIKA effective livetime as a function of primary energy at level4. The effective livetime for the combined samples is calculated based on Equation 5.25. At the relevant energy of above 100 TeV, the effective livetime is over 400 days; and at energy above 1 PeV, the effective livetime is over 1000 days.

as the interior area confined by the 6 black lines defined as follows:

$$l1 : ld = 30 \text{ for } -280 < z < 348$$

$$l2 : z - 450 = \frac{(450 - 280)}{(75 - 0)} \cdot (ld - 75) \text{ for } 30 < ld < 75$$

$$l3 : z = 450 \text{ for } ld > 75$$

$$l4 : z = -470 \text{ for } ld > 50$$

$$l5 : ld = 50 \text{ for } -470 < z < -280$$

$$l6 : z = -280 \text{ for } 30 < ld < 50$$

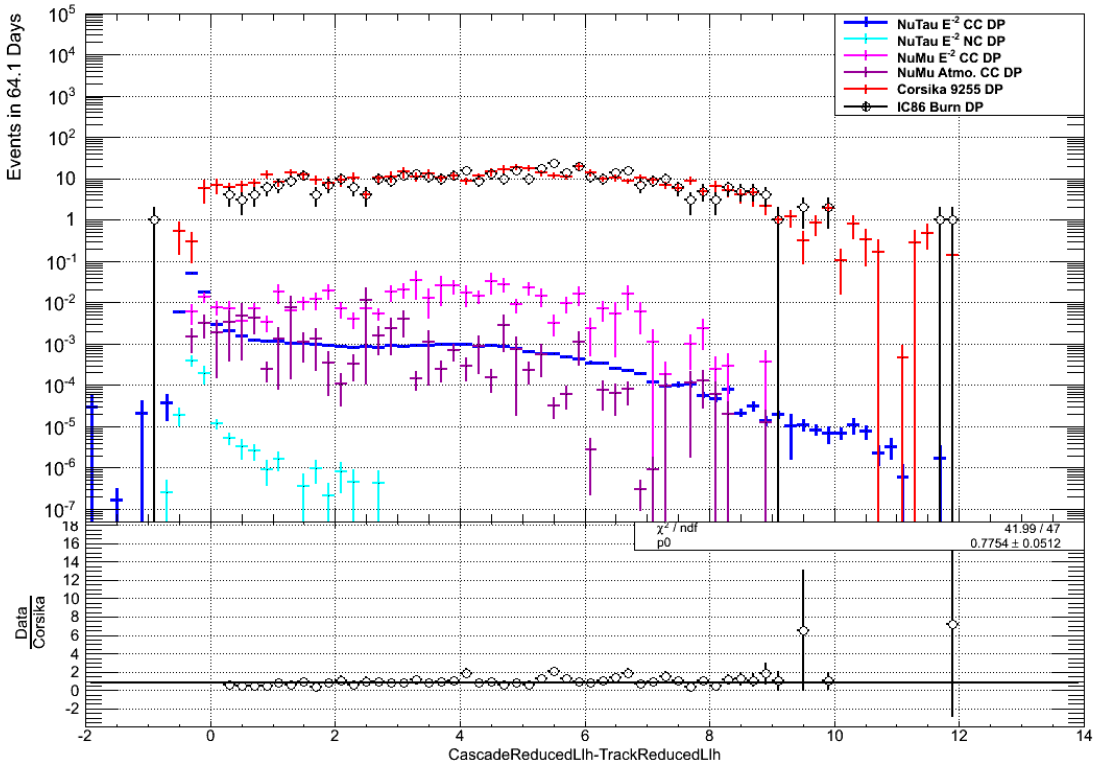

Figure 6.20: Difference between reduced log-likelihood from cascade reconstruction to that from track reconstruction. Color codes are as follows: red: CORSIKA, dark circle: burn sample, blue: ν_τ CC, magenta: ν_μ CC, cyan: ν_τ NC. The bottom panel shows the ratio of burn sample over CORSIKA, fitted with a zero order polynomial function. Signal tends to be negative and background tends to be positive.

Event locations on the reconstructed X-Y plane before and after applying the containment cut are shown in Figure 6.24 and Figure 6.25 respectively.

After the containment cut is applied, zero CORSIKA events survive. A method to estimate the atmospheric muon background rate will be introduced in Section 6.4.1. The highest remaining background contribution is from astrophysical ν_μ CC events.

6.3.3 Total Signal Rates

The total ν_τ CC event rate expectation at final cut level is 0.54±0.01 (stat.) in 914.1 days.

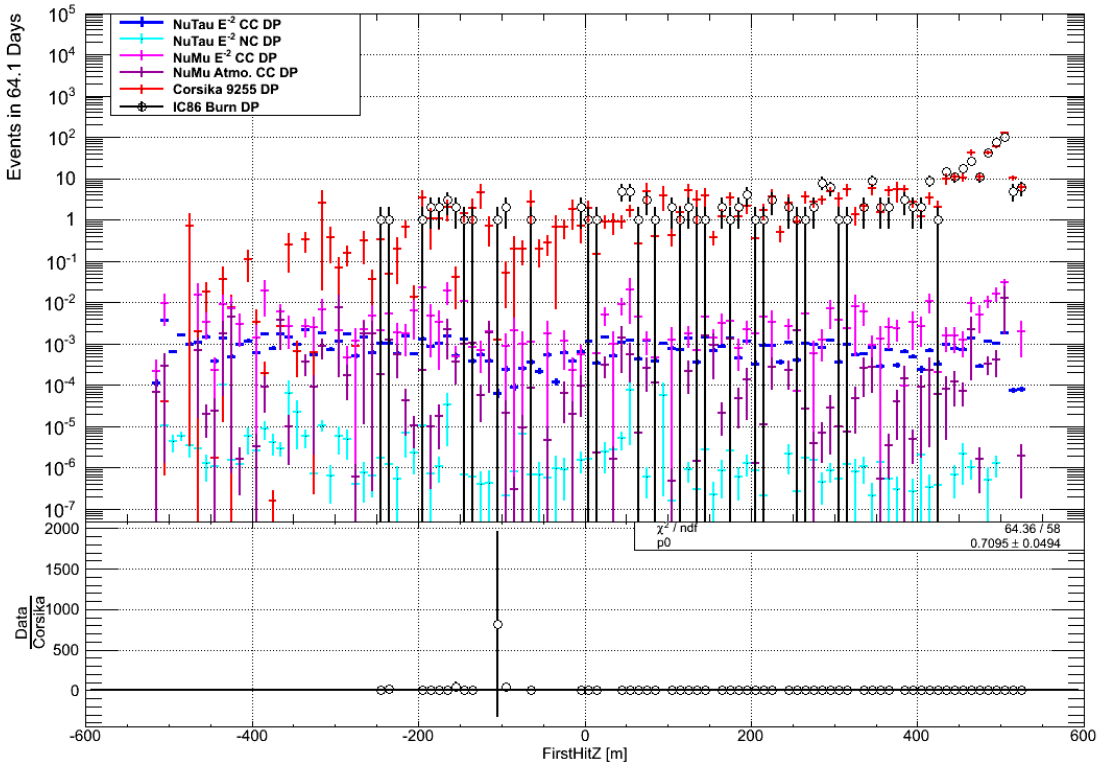

Figure 6.21: Depth of first hit. Color codes are as follows: red: CORSIKA, dark circle: burn sample, blue: ν_τ CC, magenta: ν_μ CC, cyan: ν_τ NC. The bottom panel shows the ratio of burn sample over CORSIKA, fitted with a zero order polynomial function.

6.4 Background Estimation

Both the atmospheric muon background and neutrino background estimations are based on Monte Carlo simulations.

6.4.1 Atmospheric Muon Background

The atmospheric muon background estimation was carried out using the standard IceCube CORSIKA simulation productions. At final containment cut level, no CORSIKA events survive due to limited CORSIKA statistics. Therefore, it is not possible to estimate atmospheric muon background at final cut level other than setting an upper limit of $2.3 \times \frac{T_{\text{Data}}}{T_{\text{MC}}}$, where T_{Data} and T_{MC} are total livetime of the full data sample to be unblinded and simulated CORSIKA livetime respectively.

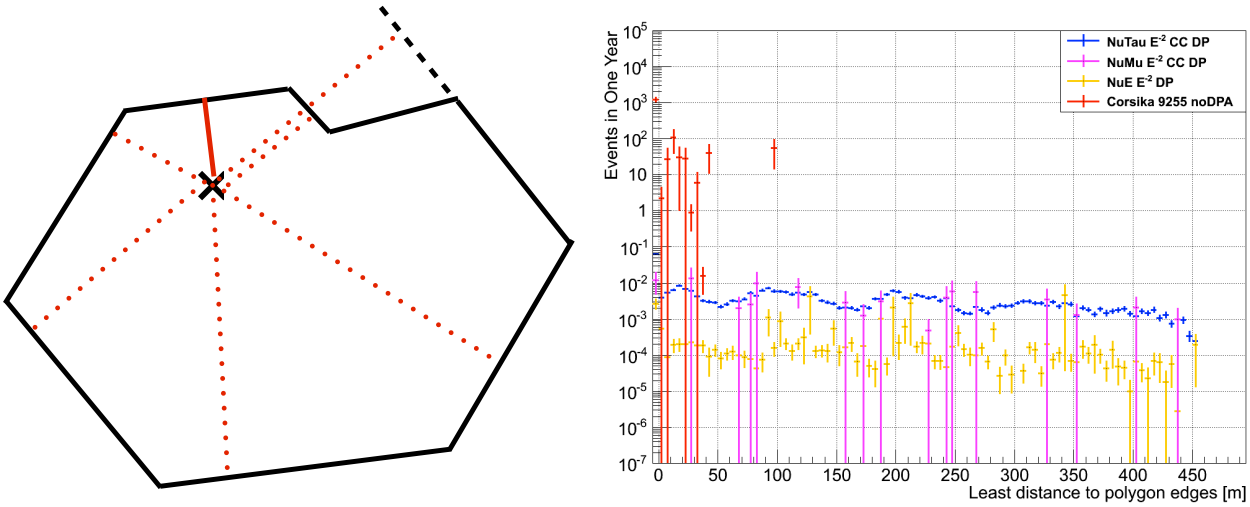

Figure 6.22: Left: sketch of least perpendicular distance from a reconstructed vertex to the detector polygon edges, the solid red line indicates the least distance. Right: distribution of least distance to polygon edges, less than zero indicates reconstructed vertices outside of the polygon.

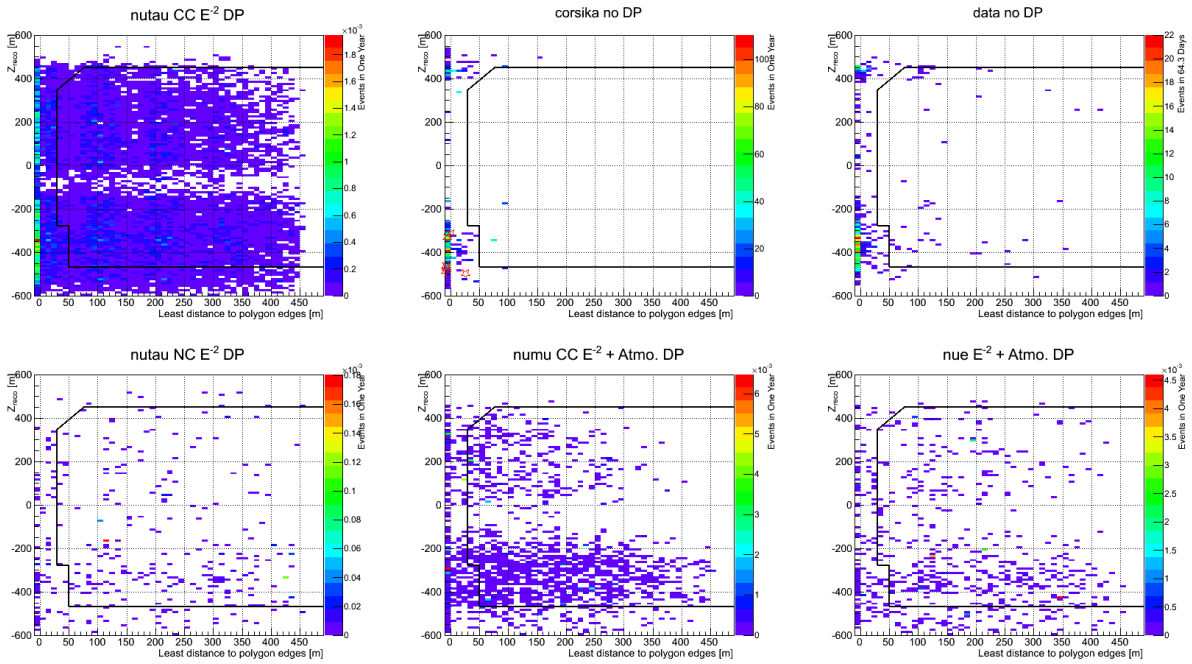

Figure 6.23: Reconstructed Z position versus least distance to polygon edges. Clockwise from top left: ν_τ CC, CORSIKA, burn sample, ν_e, ν_μ CC, ν_τ NC. For Monte Carlos, color scale indicates event rates per year; while for burn sample, color scale indicates event rates in 64.3 days.

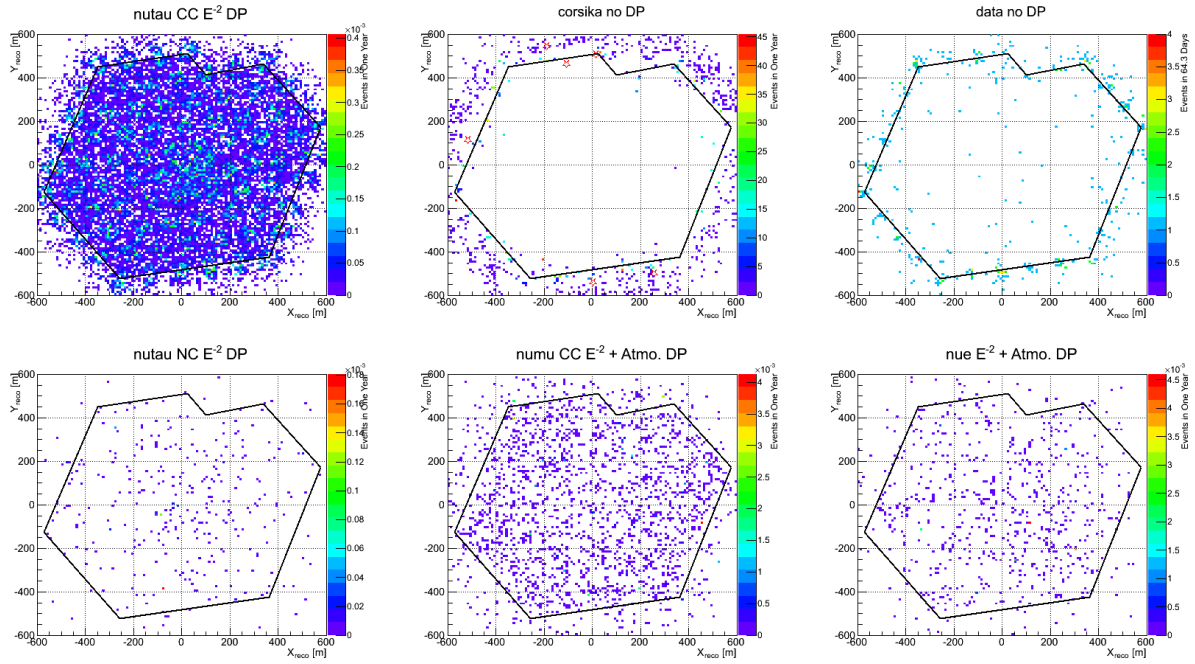

Figure 6.24: Reconstructed event X-Y vertices before containment cut. The polygon is defined by the IC86 outer layer strings. Color scale indicates event rates per year. Clockwise from top left: ν_τ CC, CORSIKA, burn sample, ν_e, ν_μ CC, ν_τ NC.

This upper limit would be large because of the limited CORSIKA livetime for IC86 simulation production.

One way to tackle this problem is to relax some of the cuts and let in a reasonable amount of CORSIKA events for muon background estimation. The double pulse cut (DPA) was removed, allowing around three orders of magnitude more events at level4. Here we denote those events without double pulse waveforms as "non-DP" events. Taking the ratio of the DP events over the non-DP events at level 2 and plot it versus QTot would give the probability of double pulse events occurring as a function of QTot at level 4. Further downstream cuts of particle identification (level5) and containment (level6) would largely reject those events without double pulse waveforms. After the track-cascade identification and containment cuts, 10 non-DP events survive. Those surviving non-DP events are corner-clippers with relatively lower energies than a DP event. Folding the non-DP rate with the probabilities of double pulse events as a function of QTot would

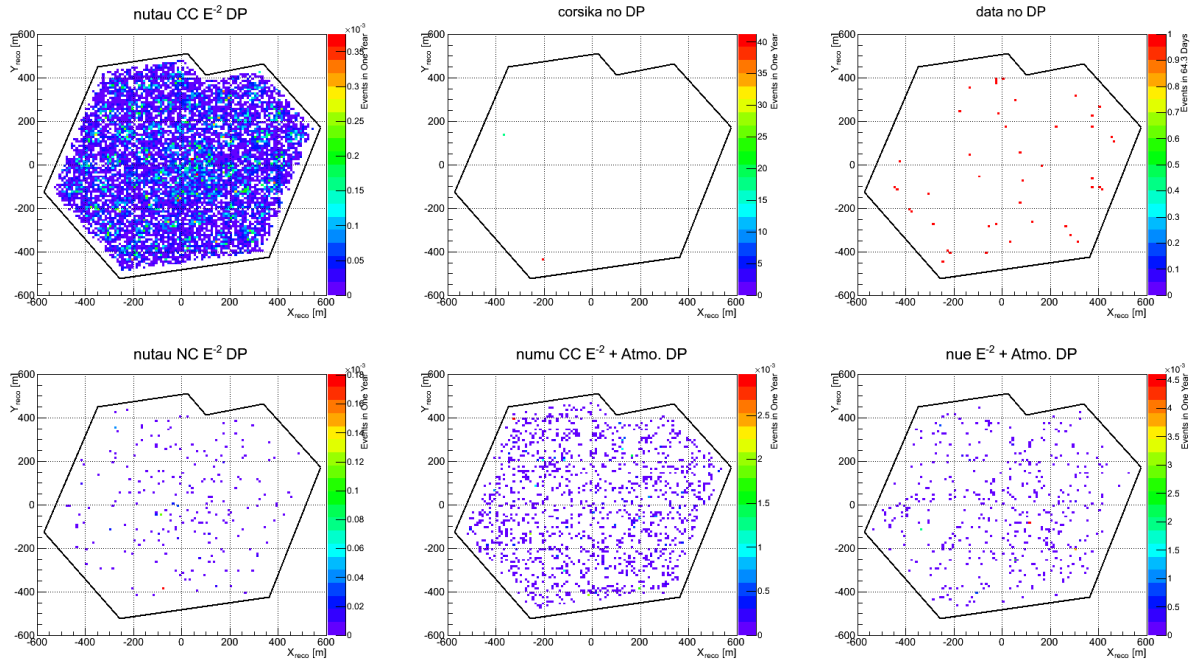

Figure 6.25: Reconstructed event X-Y vertices after containment cut. The polygon is defined by the IC86 outer layer strings. Color scale indicates event rates per year. Clockwise from top left: ν_τ CC, CORSIKA, burn sample, ν_e, ν_μ CC, ν_τ NC.

give a reasonable estimate of the muon background. The extraction of double pulse probabilities is based on burn sample data.

As shown in Figure 6.27, double pulse probabilities for CORSIKA and the burn sample are consistent with each other at log10(QTot)>3.5. At lower QTot, the burn sample seems less likely to have double pulse events than what CORSIKA predicts. This effect is due to IceCube incorrectly simulating the shape of the PMT late pulse responding to the saturated first main pulse. The right plot of Figure 6.8 shows an example of such a double pulse waveform. Therefore, it is more realistic to apply the double pulse probability based on the burn sample than CORSIKA, though the double pulse probability based on CORSIKA will give the highest atmospheric muon background estimation. The muon background estimation procedure is as follows:

Step 1: process all CORSIKA available through the same set of cuts except the double pulse cut (not running DPA). Some CORSIKA events will survive at final cut level.

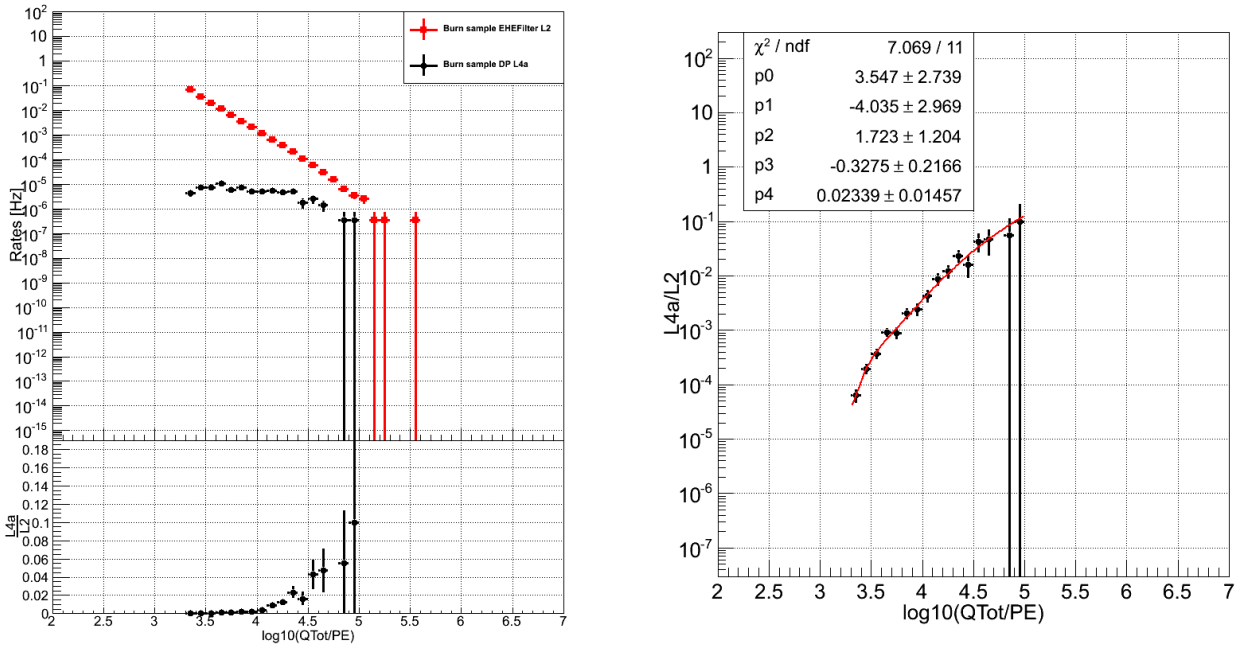

Figure 6.26: Left: rates of burn sample events as a function of event-wise QTot. L2 in red denotes EHE filter level, L4a in black is double pulse cut level which has both the filter and double pulse algorithm applied. Right: fraction of burn sample events with at least one double pulse waveform as a function of event-wise QTot, with 4th order polynomial fitted in red.

Step 2: apply the double pulse probability (as a function of QTot) as an additional weight factor to every surviving non-DP corsika event.

Step 3: sum the weights of the reweighted non-DP events to give the atmospheric muon background rate estimation.

The atmospheric muon background rates estimated following this procedure is summarized in Table 6.6.

Cut levels	Level5: rllhratio<0 && firstHitz<460m	Level6: Containment
With DP probability from burn sample	2.56 ±0.57	$(7.5 \pm 5.8)\cdot 10^{-2}$
With DP probability from CORSIKA	4.12 ±0.71	$(10.7 \pm 6.1)\cdot 10^{-2}$
With straight cuts	3.55 ±3.41	0 (<2.3· LivetimeFactor[5])

Table 6.6: Atmospheric muon rates based on DP probabilities with rates normalized to a total data livetime of 914.1 days. Errors are statistical only.

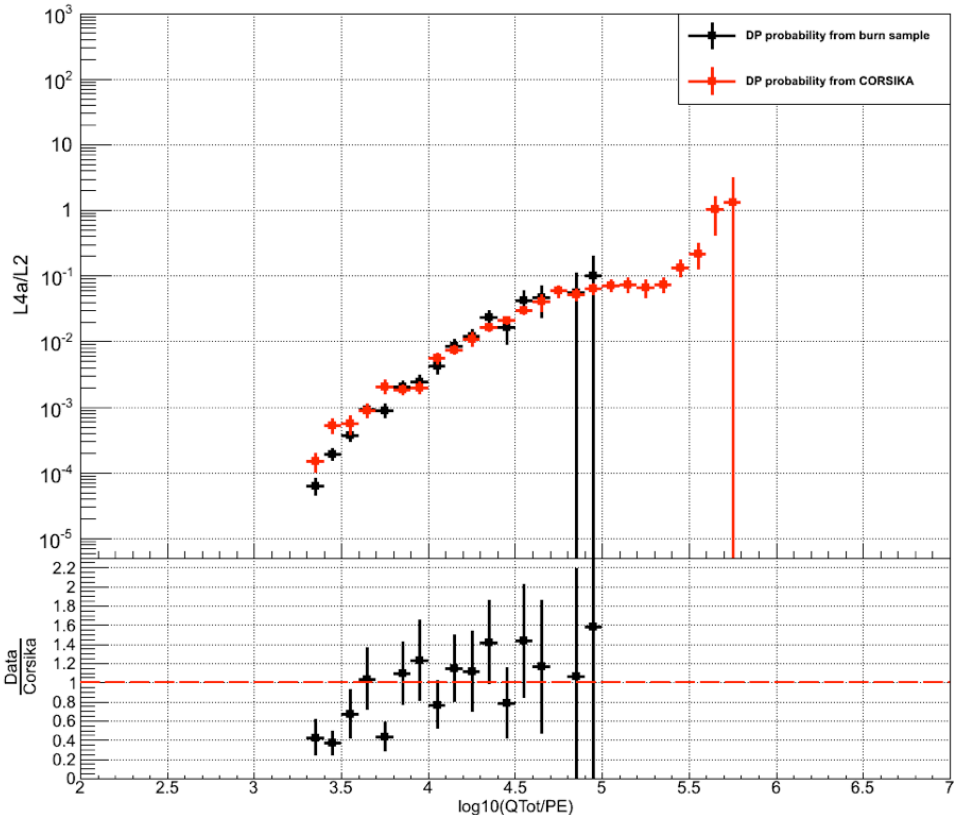

Figure 6.27: Top: fraction of events with at least one double pulse waveform from burn sample (black) and CORSIKA (red) as a function of event-wise QTot. L2 denotes EHE filter level, L4a is double pulse cut level which has both the filter and double pulse algorithm applied. Bottom: ratio of double pulse fraction in burn sample to CORSIKA as a function of event-wise QTot.

6.4.2 Neutrino Background

The neutrino backgrounds that are considered and accounted for in this analysis include:

- Astrophysical ν_μ CC and NC events
- Astrophysical ν_e CC and NC events
- Astrophysical ν_τ NC events
- Atmospheric ν_μ CC and NC events
- Atmospheric ν_e CC and NC events

[5]The effective livetime for the combined CORSIKA samples is $\sim$ 1000 days at the PeV regime, and the total livetime of data to be unblinded is 914.1 days. This gives a LivetimeFactor of $\frac{914.1}{1000} \sim 0.9$.

- Atmospheric ν_τ is negligible

Neutral current events of all neutrino interactions and all ν_e charged current events - both astrophysical and atmospheric - are negligible backgrounds to this analysis as there is no physical mechanism from those events to produce two consecutive substantial energy depositions which would create a double pulse. At final cut level, the major background contribution is from astrophysical ν_μ events which amounts to about one third of signal expectation. Background contributions from various types of neutrino events are summarized in Table 6.7. The total background expectation from neutrinos at final cut level is 0.27 ± 0.02 (stat.) in 914.1 days.

6.4.3 Total Background Rates

Summing up background contributions from both atmospheric muons and neutrinos yields a total of 0.35 ± 0.06 (stat.) events in 914.1 days.

6.5 Expected Rates and Cut Efficiency

Table 6.7 summarizes event rates from various samples at the three cut levels. The cut efficiency for different data samples at various cut levels is demonstrated in Figure 6.28.

6.6 Sensitivity

6.6.1 Model Rejection Factor

During the event selection process, decisions have to be made to maximise the signal to noise ratio at every cut level. All cuts are usually derived from Monte Carlo simulation instead of data to avoid artificially inducing bias to the data. So how to choose experiment cuts to place the most stringent upper limits on theoretical signal models? The concepts of "average upper limit" and "model rejection factor" introduced in [188] will serve to answer this question.

Data samples	Level4	Level5	Level6
ν_τ CC E^{-2}	$(1.39 \pm 0.12) \cdot 10^{-1}$	$(9.37 \pm 0.11) \cdot 10^{-2}$	$(5.80 \pm 0.09) \cdot 10^{-2}$
ν_τ NC E^{-2}	$(8.08 \pm 1.99) \cdot 10^{-4}$	$(7.69 \pm 1.99) \cdot 10^{-4}$	$(2.74 \pm 0.62) \cdot 10^{-4}$
ν_μ CC E^{-2}	$(6.14 \pm 0.90) \cdot 10^{-1}$	$(2.94 \pm 0.02) \cdot 10^{-2}$	$(1.90 \pm 0.02) \cdot 10^{-2}$
ν_e E^{-2}	$(1.92 \pm 3.76) \cdot 10^{-2}$	$(8.53 \pm 1.90) \cdot 10^{-3}$	$(6.44 \pm 1.87) \cdot 10^{-3}$
ν_e Atmospheric	$(6.94 \pm 4.02) \cdot 10^{-3}$	$(1.44 \pm 0.85) \cdot 10^{-3}$	$(6.87 \pm 5.10) \cdot 10^{-4}$
ν_μ Atmospheric	$(9.15 \pm 2.38) \cdot 10^{-2}$	$(9.47 \pm 4.64) \cdot 10^{-3}$	$(2.77 \pm 1.03) \cdot 10^{-3}$
CORSIKA (weighted to Hörandel5 [175])	(715.6 ± 39.9)	0.29 ± 0.29	0 (<2.3)
CORSIKA (weighted to GaisserH3a [187])	947.3 ± 47.2	0.38 ± 0.37	0 (<2.3)
Burn Sample	695±26	0	0
Sum of ν Background	-	-	$(2.92 \pm 0.23) \cdot 10^{-2}$

Table 6.7: Expected event counts at different cut levels in the three year burn sample livetime of 97.9 days. For astrophysical neutrinos, rates are normalized to a E^{-2} energy spectrum with flux limit of 1.0×10^{-8} GeV^{-1} cm^{-1} sr^{-1} s^{-1} [1]. Errors are statistical only.

If an expected flux predicted by some theoretical model is not detected in an experiment, an upper limit on that flux can be derived based on the non-observation. That means we don't know the actual upper limit until looking at the real data. However, we can utilize the Monte Carlo to simulate an ensemble of experiments to derive an average upper limit by summing up all the expected upper limits weighted by their Poisson probability of occurrence based on zero true signal hypothesis. Hence, the average upper limit with 90% confidence level $\bar{\mu}_{90}$ is

$$\bar{\mu}_{90}(n_b) = \sum_{n_{obs}=0}^{\infty} \mu_{90}(n_{obs}, n_b) \, \frac{(n_b)^{n_{obs}}}{(n_{obs})!} \exp(-n_b) \tag{6.1}$$

Where n_b and n_{obs} denote the numbers of expected background and observed events respectively, and μ_{90} represents the upper limit for a specific set of n_b and n_{obs} at 90% confidence level. The most stringent upper limit can be set by an experiment following cuts which minimise the model rejection factor defined as the ratio of the average upper limit $\bar{\mu}_{90}$ and the expected signal

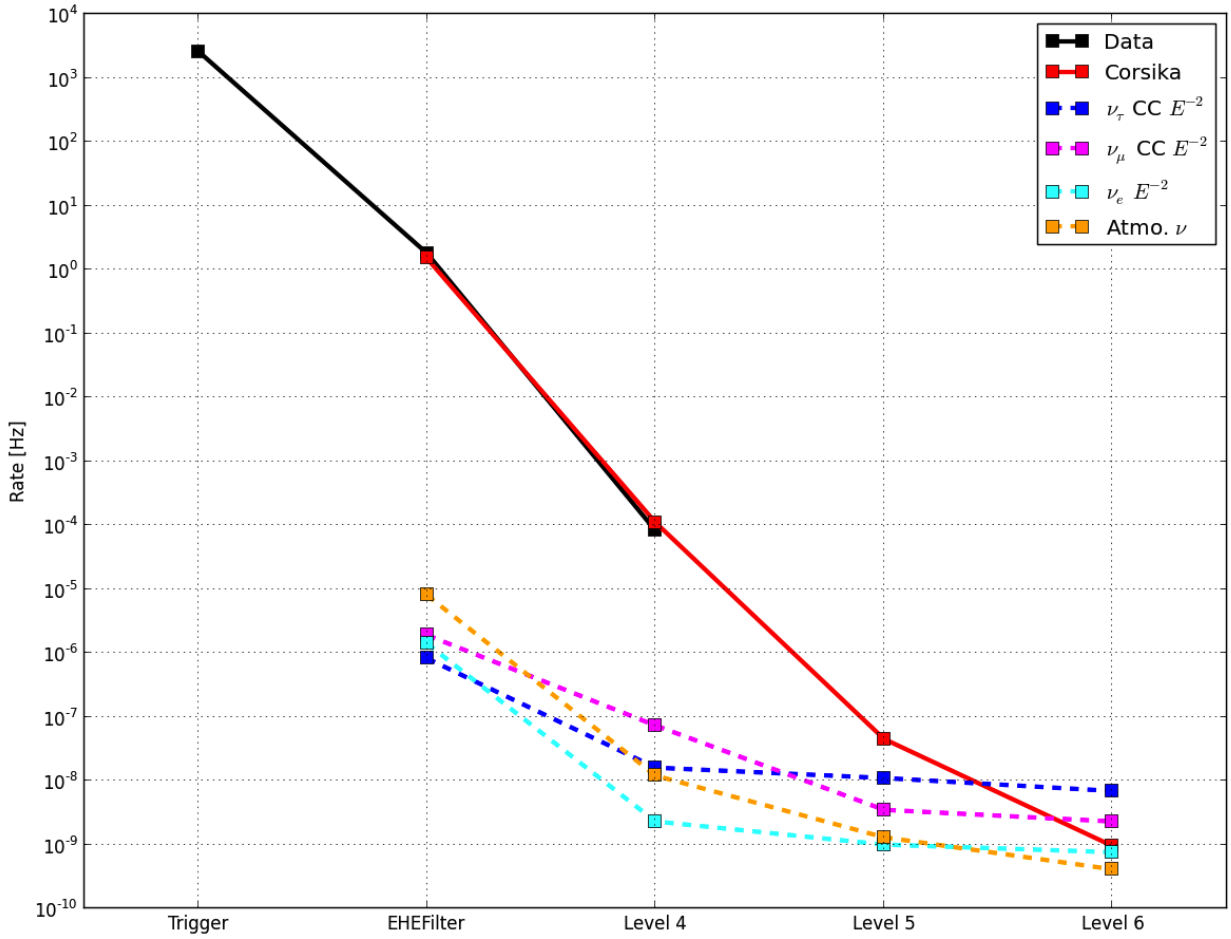

Figure 6.28: Cut efficiency as a function of cut levels. Black: burn sample. Red: CORSIKA. Blue: astrophysical ν_τ CC. Pink: astrophysical ν_μ CC. Cyan: astrophysical nu_e. Yellow: atmospheric neutrinos.

n_s

$$\text{MRF} = \frac{\bar{\mu}_{90}}{n_s} \tag{6.2}$$

The most restrictive constraint on the expected signal flux $\Phi(E, \theta)$ or sensitivity of the experiment is therefore

$$\bar{\Phi}(E, \theta)_{90} = \Phi(E, \theta) \cdot \text{MRF} \tag{6.3}$$

In 914.1 days, a total of 0.54±0.01 signal events and 0.35±0.06 background events are expected. The MRF based on these numbers is computed to be 5.1. The computation procedure is as follows:

- Calculate the average upper limit which is purely background dependent following Equation 6.1. The average upper limit is calculated to be 2.74.
- According to Equation 6.2, MRF = $\frac{\text{Average Upper Limit}}{N_{\text{signal}}} = \frac{2.74}{0.54} \simeq 5.1$.

Therefore, based on a flux limit of $E^2\Phi_{\nu_\tau}$=1.0×10^{-8} GeV cm^{-2} s^{-1} sr^{-1}, the sensitivity of this analysis is 5.1×10^{-8} GeV cm^{-2} s^{-1} sr^{-1}.

Upon unblinding, if no events are found, the ν_τ flux upper limit set by this analysis is simply the predicted sensitivity.

6.6.2 Effective Areas

The effective areas describe the efficiency of the IceCube detector for detecting neutrinos through the double pulse method. This detection efficiency is derived from Monte Carlo (NuGen) simulations which are fully propagated through the detector instrumentation and event analysis. The weights of simulated events surviving certain cut level can be used to describe detection efficiency related to that specific cut level as a function of primary neutrino energy in units of area:

$$A_{eff} = \frac{\frac{\pi r_{gen}^2 \Omega}{4\pi} \sum_i \frac{p_{int,i}}{N p_{gen,i}}}{\Delta E} \tag{6.4}$$

with ΔE being the energy interval where event weights are summed over. Figure 6.29 is the effective areas for ν_τ CC, ν_μ CC and ν_e events at final cut level following Equation 6.4.

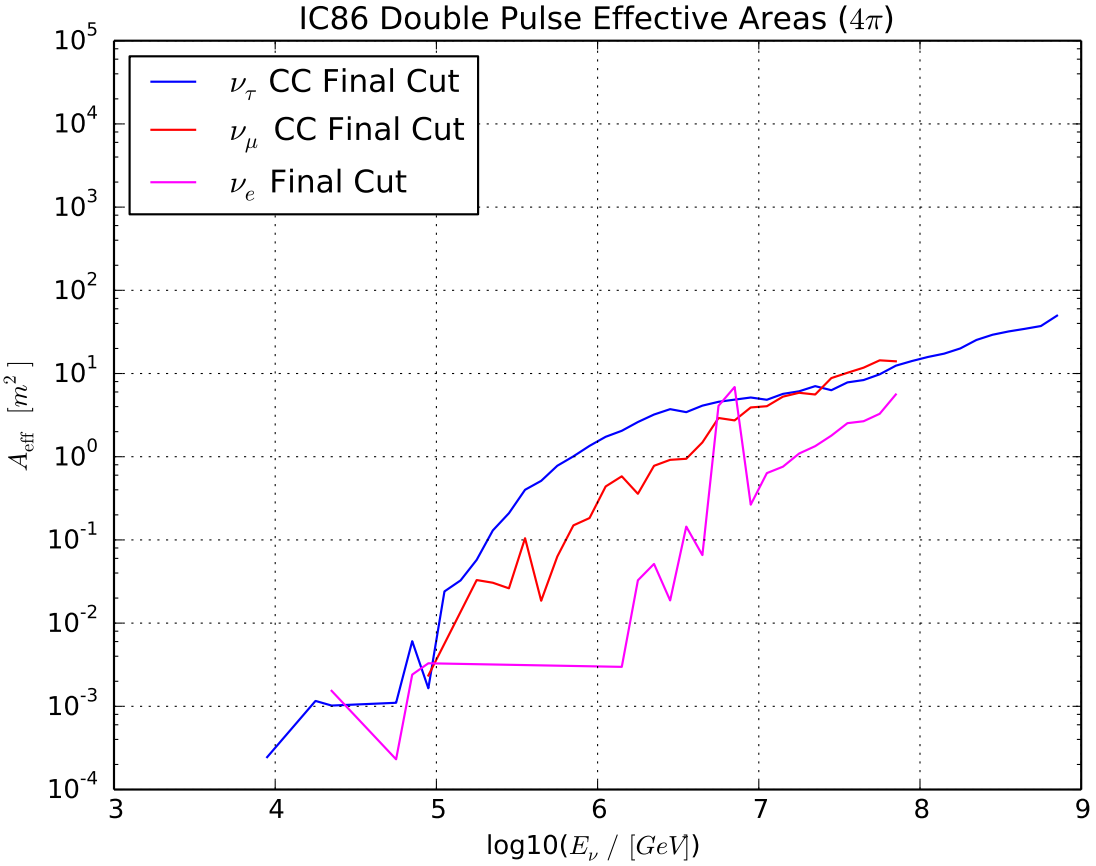

Figure 6.29: Effective areas at final cut level as a function of primary neutrino energy. Blue: ν_τ. Red: ν_μ. Pink: ν_e. The bumpy feature from both ν_μ CC and ν_e events is caused by lack of Monte Carlo statistics, and the big bump from ν_e at about 6.3 PeV indicates Glashow resonance [156].

Chapter 7

Results

7.1 Unblinding Results

Three years of IceCube data with 86 strings and a total livetime of 914.1 days were unblinded. Zero events were found at the final cut level. However, three events are found before the final containment cut, and they are consistent with the atmospheric muon background prediction. Each of the three events has only one double pulse waveform. Figure 7.1 to Figure 7.3 are displays of the three events and their corresponding double pulse waveforms. The events occur at different times of the year and different detector locations.

The event rate from the blind sample agrees well with Monte Carlo prediction, which indicates that the developed analysis methods are valid. Detailed comparison of event rates between the blind sample and CORSIKA is summarized in Table 7.1.

Event counts in 914.1 Days	Level5	Level6
CORSIKA	3.5 $\pm$3.4	0.08$\pm$0.06
Blind Sample	3$\pm$2	0

Table 7.1: Number of atmospheric muon event expectation normalized to the blind sample livetime of 914.1 days, in comparison to the blind sample rate. Errors are statistical only.

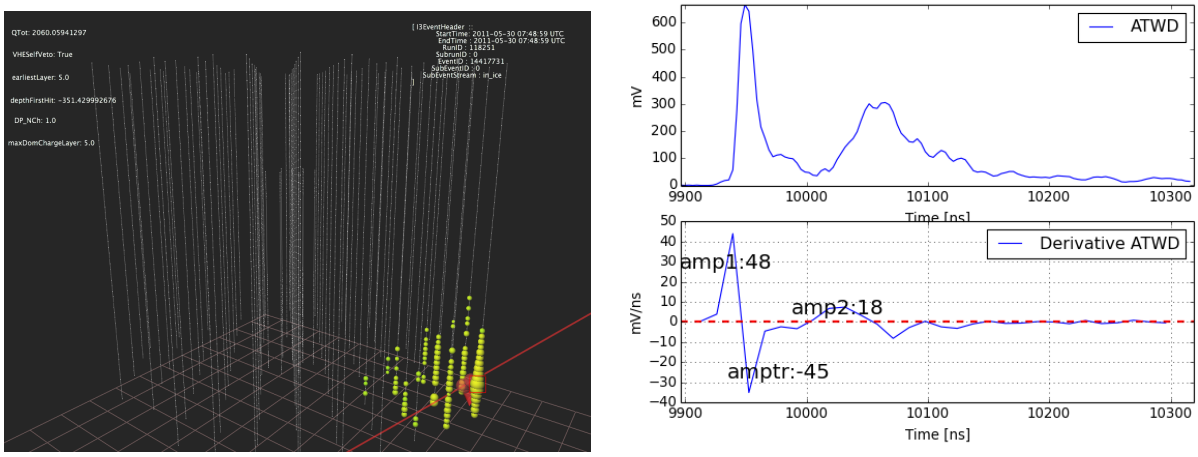

Figure 7.1: Left: event display for event 1 from blind sample at level5 which is before the final containment cut. This event occurred on May 30, 2011 with event-wise charge QTot of 2060 PE. Right: the double pulse waveform corresponding to this event. The double pulse waveform is from OM(31, 54) [2]which is circled by the red square from the event display.

7.2 Differential Upper Limits

Based on the zero findings, the ν_τ flux upper limit (integrated over all energies) is simply the sensitivity which is computed in Section 6.6.

A ν_τ flux differential upper limit can be extracted based on the ν_τ Monte Carlo sample at final cut level. Over some observation time T, dN events are observed in the energy interval of $dlogE_{\nu_\tau}$ and solid angle interval of $d\Omega$:

$$dN = dJ_{\nu_\tau}\ A_{\nu_\tau}(E_{\nu_\tau})\ T = \frac{dJ_{\nu_\tau}}{dlogE_{\nu_\tau} d\Omega} A_{\nu_\tau}(E_{\nu_\tau})\ T\ dlogE_{\nu_\tau}\ d\Omega \tag{7.1}$$

where $A_{\nu_\tau}(E_{\nu_\tau})$ is the ν_τ effective area at energy interval of $dlogE_{\nu_\tau}$. Then the differential flux can be written as

$$\frac{dJ_{\nu_\tau}}{dE_{\nu_\tau}\ d\Omega} = \frac{dN}{\ln 10\ E_{\nu_\tau}\ A_{\nu_\tau}(E_{\nu_\tau})\ T\ dlogE_{\nu_\tau}\ d\Omega} \leq \frac{N_{90}}{4\pi\ \ln 10\ E_{\nu_\tau}\ A_{\nu_\tau}(E_{\nu_\tau})\ T} \tag{7.2}$$

[2]An OM key is a pair of integer numbers with the first one indicating the String number and the second indicating the DOM number.

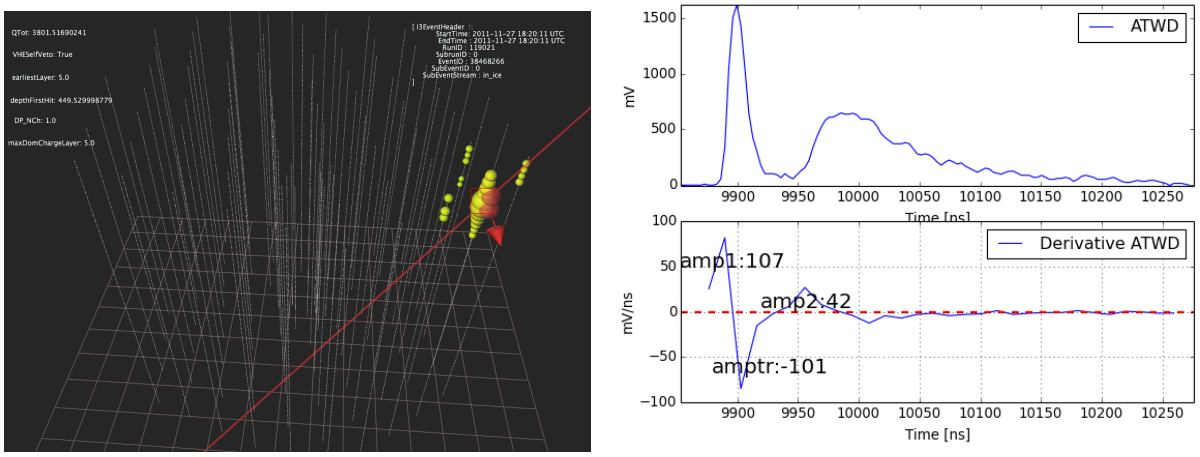

Figure 7.2: Left: event display for event 2 from blind sample at level5 which is before the final containment cut. This event occurred on November 27, 2011 with event-wise charge QTot of 3820 PE. Right: the double pulse waveform corresponding to this event. The double pulse waveform is from OM(7, 5) which is circled by the red square from the event display.

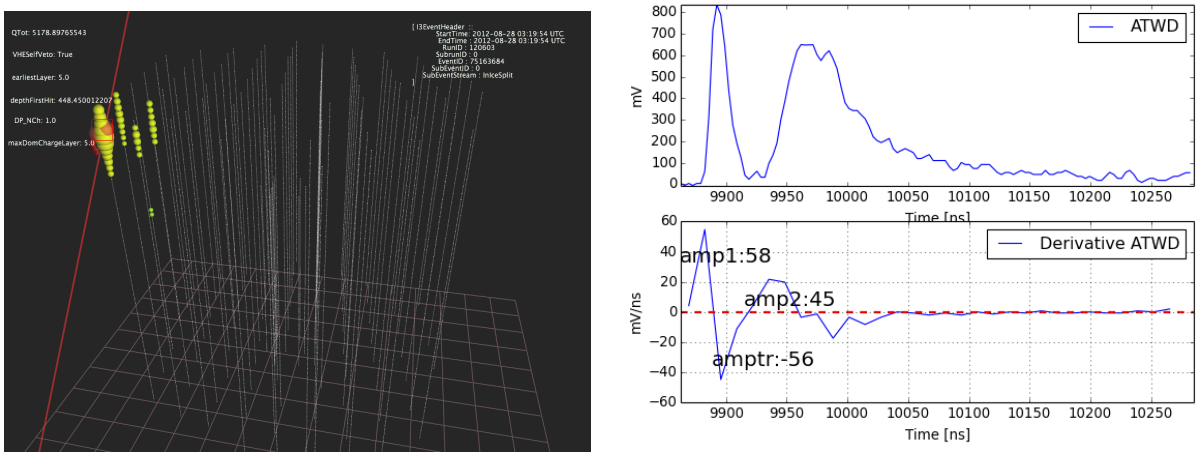

Figure 7.3: Left: event display for event 3 from blind sample at level5 which is before the final containment cut. This event occurred on August 28, 2012 with event-wise charge QTot of 5179 PE. Right: the double pulse waveform corresponding to this event. The double pulse waveform is from OM(6, 4) which is circled by the red square from the event display.

where N_{90} is the 90% C.L. upper limit of number of events in the energy interval of $dlogE_{\nu_\tau}$. In this context, the $A_{\nu_\tau}(E_{\nu_\tau})$ was calculated by averaging over one decade with a sliding step of $log10(E_{\nu_\tau}) = 0.1$. With zero events observed over all energies, the N_{90} for each energy interval

is simply 2.4 based on the Feldman-Cousins approach [189]. Therefore, the ν_τ differential upper limits can be computed as:

$$E^2_{\nu_\tau} \frac{dJ_{\nu_\tau}}{dE_{\nu_\tau}\, d\Omega} \leq \frac{2.4\ E_{\nu_\tau}}{4\pi\ \ln 10\ A_{\nu_\tau}(E_{\nu_\tau})\ T} \tag{7.3}$$

The red thick line in Figure 7.4 is the ν_τ differential upper limit calculated following Equation 7.3.

7.3 Systematics

7.3.1 Ice Anisotropy

An earlier study attempting to reconstruct the double deposition of energy from a ν_τ CC event has found that the recently identified ice anisotropy (detailed discussion in Section 4.1.4) would modify the number of expected photons at some DOMs and hence could mimic a double pulse feature in the reconstructed energy segments [193]. Possible impacts from ice anisotropy on the ν_τ double pulse event search are that the angular dependent ice optical properties might distort the photons traveling in ice in a way such that, either an artificial double pulse waveform is induced, or a real double pulse waveform is washed out. To investigate these possible impacts, simulations for ice models with (SpiceLea) and without (SpiceMie) ice anisotropy were generated and analyzed.

Both of the simulations were processed through the same selection criteria–the double pulse algorithm–which is optimized to pick up events with bright double pulse waveforms. Event rates with double pulse waveforms in terms of neutrino energy distributions are shown in Figure 7.5. The overall ν_τ double pulse event rate prediction for SpiceLea is $\sim 7\%$ lower than that of SpiceMie, which indicates that ice anisotropy is not a major systematic uncertainty source for this analysis.

7.3.2 Neutrino Cross Sections

The neutrino cross sections used in this analysis are from the CTEQ5 model [170]. Comparing to a simulated ν_τ sample with cross sections from the CSS model [194], yields $\sim$15% difference in

event rate at the EHE filtering level. Another cross section model commonly used in IceCube is the CSMS model [195], which is expected to be within 10% compared to the CTEQ5 model. Among these three neutrino cross section models, CTEQ5 predicts the highest event rate.

Other sources of systematic uncertainties are variation in the ice model coefficients, DOM efficiency and astrophysical neutrino flavor ratios at Earth. The double pulse events usually occur tens of meters near certain DOMs, which is within one scattering length in the ice. Therefore, the ice property uncertainties are expected to be not important for this analysis. Also, the ν_τ double pulse events are very bright, uncertainty of the DOM efficiency does not play an important role. Though the astrophysical neutrino flavor ratio at Earth is still consistent with the 1:1:1 assumption, the uncertainty on this ratio is large [90]. Studies to investigate the impact to this analysis from variation of neutrino flavor ratio at Earth is currently ongoing.

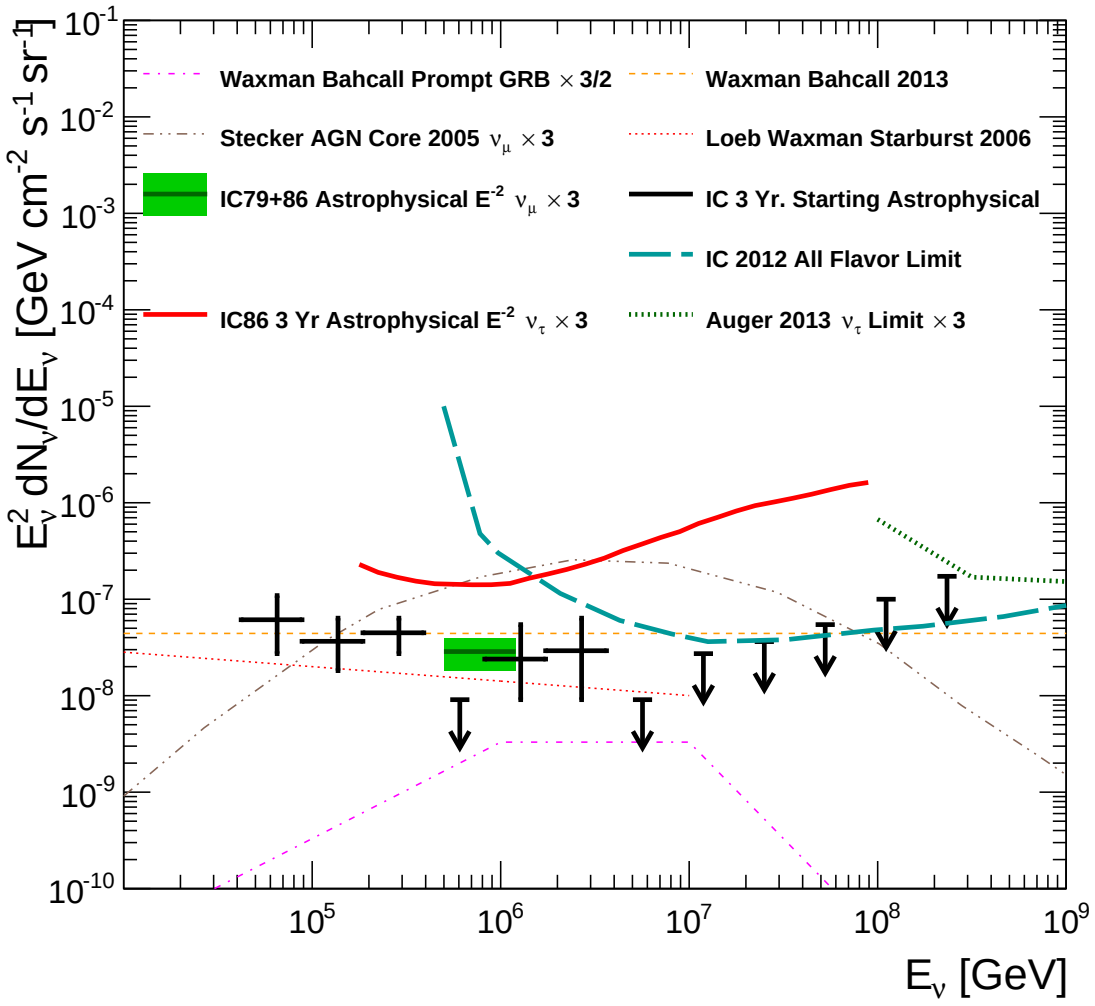

Figure 7.4: Neutrino flux upper limits and models as a function of the primary neutrino energy. The thick red curve is the ν_τ differential upper limit derived from this analysis. The black crosses depict the all flavor astrophysical neutrino flux observed by IceCube [1]. The short black line with green shade is an astrophysical ν_μ flux observed by a recent dedicated IceCube search (to be published soon). The thick dash line is the differential upper limit derived from a search for extremely high energy events which has found the first two PeV cascade events in IceCube [190, 191]. The thick dotted line is the Auger differential upper limit from ν_τ induced air showers [192]. The thin dash line (orange) is the Waxman-Bahcall upper bound which uses the UHECR flux to set a bound on astrophysical neutrino production [81]. The dash-dotted line (magenta) is prompt neutrino flux predicted from GRBs; prompt in this context means in time with the gamma rays [82]. The dash-dot-dot line (grey) is neutrino flux predicted from the cores of active galaxies [83]. The thin dotted line (red) is neutrino flux predicted from starburst galaxies, which are rich in supernovae [84].

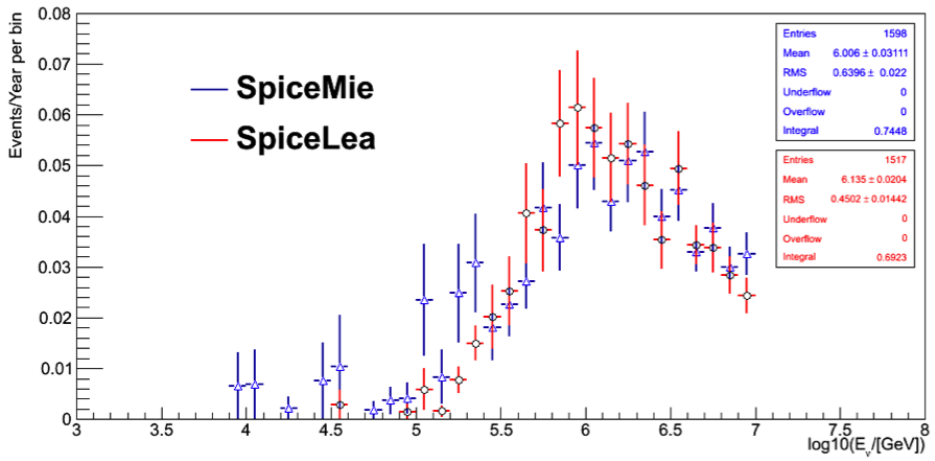

Figure 7.5: Event rates as a function of primary neutrino energy with ice anisotropy (SpiceLea, red) and without ice anisotropy (SpiceMie, blue).

Chapter 8

Conclusion and Outlook

This work has developed a new method to search for high energy tau neutrinos by identifying a double pulse signature in the IceCube waveforms. At final cut level, the signal expectation rate is 0.54 ± 0.01 (stat.) and the total background expectation is 0.35 ± 0.06 (stat.) in a livetime of 914.1 days collected between May 2011 and May 2014, assuming an E^{-2} astrophysical neutrino energy spectrum and a flux limit of $E^2\Phi_\nu < 1.0 \times 10^{-8}$ GeV cm^{-2} s^{-1} sr^{-1} set by the all-flavor IceCube neutrino measurement [1]. The sensitivity for this analysis is 5.1×10^{-8} GeV cm^{-2} s^{-1} sr^{-1} based on the same flux limit. This is the first IceCube analysis to be more sensitive to tau neutrinos than to any other flavor, and the lowest energy dedicated astrophysical tau neutrino analysis. Zero events were found upon unblinding. Based on this, for the first time a differential upper limit for astrophysical ν_τ flux is derived between 214 TeV to 72 PeV to cast generic constraint on the astrophysical neutrino flux models at these energies.

Other efforts to search for high-energy astrophysical ν_τ signatures in IceCube are ongoing within the collaboration. This includes a search for ν_τ CC double bang events and a search for ν_τ CC hybrid events with the τ lepton decaying muonically and producing a cascade plus a an outgoing track. Signal expectation from the double bang search is comparable to that of this work. With indication of possibly softer energy spectrum index (-2.3 instead of -2) from current IceCube results [1], both double pulse and double bang searches will be less sensitive. Due to the higher energy threshold and a steeply falling energy spectrum, double bang analyses will suffer more

signal loss from softer energy spectrum index than the double pulse analysis which has a lower energy threshold.

The IceCube collaboration is in the process of planning a second generation upgrade called IceCube-Gen2. IceCube-Gen2 will extend to a volume 10 times that of the current IceCube detector, yielding 10 cubic kilometers of instrumented volume. One hundred and twenty strings with 60 DOMs per string and 240 meters horizontal spacing will be deployed in ice pending funding approval, surrounding IceCube [196]. This additional array has about 2.4 times the current number IceCube DOMs. The ν_τ CC double pulse event rate increases by 2 to 3 times in IceCube-Gen2 compared to that in IceCube, because the double pulse events occur rather close to certain DOMs and hence the event rate scales as the total number of DOMs. While for the double bang search, the event topology relies on the total instrumented volume, so the double bang event rate increases about 10 times in IceCube-Gen2.

References

[1] M. Aartsen *et al.*, Phys. Rev. Lett. **113**, 101101 (2014).

[2] J. G. Learned and S. Pakvasa, Astroparticle Physics **3**, 267 (1995).

[3] S. L. Glashow, Nuclear Physics **22**, 579 (1961).

[4] S. Weinberg, Phys. Rev. Lett. **19**, 1264 (1967).

[5] D. Lincoln, Fermilab Today (2011), `http://www.fnal.gov/pub/today/archive/archive_2011/today11-11-18_NutshellStandardModelReadMore.html`.

[6] W. Pauli, Phys. Today **31N9**, 27 (1978).

[7] E. Fermi, Z. Phys. **88**, 161 (1934).

[8] J. Chadwick, Nature **129**, 312 (1932).

[9] K. C. Wang, Physical Review **61**, 97 (1942).

[10] F. Reines and C. L. Cowan, Phys. Rev. **92**, 830 (1953).

[11] C. L. Cowan, F. Reines, F. B. Harrison, H. W. Kruse, and A. D. McGuire, Science **124**, 103 (1956).

[12] J. T. Shipley, *Dictionary of Word Origins* (The Philosophical Library, 1945), p. 133.

[13] J. J. Thomson, Philosophical Magazine **44**, 293 (1897).

[14] S. H. Neddermeyer and C. D. Anderson, Physical Review **51**, 884 (1937).

[15] G. Danby *et al.*, Phys. Rev. Lett. **9**, 36 (1962).

[16] DONUT Collaboration, K. Kodama *et al.*, Physics Letters B **504**, 218 (2001), arXiv:hep-ex/0012035.

[17] M. L. Perl *et al.*, Phys. Rev. Lett. **35**, 1489 (1975).

[18] Particle Data Group, J. Beringer *et al.*, Phys. Rev. D **86**, 010001 (2012).

[19] R. Schwienhorst *et al.*, Physics Letters B **513**, 23 (2001).

[20] T. D. Lee and C. N. Yang, Phys. Rev. **104**, 254 (1956).

[21] Los Alamos Science (25) (1997), http://library.lanl.gov/cgi-bin/getfile?25-03.pdf.

[22] Y. Fukuda *et al.*, Phys. Rev. Lett. **81**, 1562 (1998).

[23] B. Pontecorvo, Sov.Phys.JETP **6**, 429 (1957).

[24] B. Pontecorvo, Sov. Phys. JETP **26**, 984 (1968).

[25] Z. Maki, M. Nakagawa, and S. Sakata, Progress of Theoretical Physics **28**, 870 (1962).

[26] J. Kopp, *Phenomenology of three-flavour neutrino oscillations*, PhD thesis, 2006.

[27] J. A. Wheeler, Phys. Rev. **52**, 1107 (1937).

[28] KamLAND Collaboration, A. Gando *et al.*, Phys. Rev. D **83**, 052002 (2011).

[29] K. Olive *et al.*, Chinese Physics C **38**, 090001 (2014).

[30] Double Chooz Collaboration, M. Apollonio *et al.*, Physics Letters B **466**, 415 (1999).

[31] Double Chooz Collaboration, Y. Abe *et al.*, Phys. Rev. Lett. **108**, 131801 (2012).

[32] Daya Bay Collaboration, F. An *et al.*, Phys. Rev. Lett. **108**, 171803 (2012).

[33] RENO Collaboration, J. Ahn *et al.*, Phys. Rev. Lett. **108**, 191802 (2012).

[34] K2K Collaboration, M. Ahn *et al.*, Phys. Rev. D **74**, 072003 (2006).

[35] MINOS Collaboration, P. Adamson *et al.*, Phys. Rev. Lett. **112**, 191801 (2014).

[36] T2K Collaboration, K. Abe *et al.*, Phys. Rev. Lett. **112**, 181801 (2014).

[37] K. Abe *et al.*, Phys. Rev. Lett. **110**, 181802 (2013).

[38] OPERA Collaboration, N. Agafonova *et al.*, Physics Letters B **691**, 138 (2010).

[39] OPERA Collaboration, N. Agafonova *et al.*, Opera observes the second tau neutrino, 2012.

[40] OPERA Collaboration, N. Agafonova *et al.*, Opera observed a third neutrino tau, 2013.

[41] L. Wolfenstein, Phys. Rev. D **17**, 2369 (1978).

[42] S. Nussinov, Phys. Lett. **B63**, 201 (1976).

[43] Y. Farzan and A. Y. Smirnov, Nuclear physics B **805**, 356 (2008).

[44] J. Ilmavirta, *Coherence in neutrino oscillations*, Bachelor thesis, 2011.

[45] C. Giunti, Journal of Physics G: Nuclear and Particle Physics **34**, R93 (2007).

[46] K. Kiers, S. Nussinov, and N. Weiss, Phys. Rev. D **53**, 537 (1996).

[47] F. R. Torres and M. M. Guzzo, Brazilian Journal of Physics **37**, 1273 (2007).

[48] P. Lipari, *INTRODUCTION TO NEUTRINO PHYSICS*, 2003.

[49] D. N. Schramm and M. S. Turner, Rev. Mod. Phys. **70**, 303 (1998).

[50] `http://wmap.gsfc.nasa.gov/universe/uni_matter.html`.

[51] N. W. Boggess *et al.*, The Astrophysical Journal **397**, 420 (1992).

[52] D. J. Fixsen *et al.*, The Astrophysical Journal **420**, 445 (1994).

[53] Planck Collaboration, R. Adam *et al.*, (2015), 1502.01582.

[54] A. A. Penzias and R. W. Wilson, The Astrophysical Journal **142**, 419 (1965).

[55] M. S. Turner and J. A. Tyson, Reviews of Modern Physics **71**, S145 (1999).

[56] J. N. Bahcall, M. Pinsonneault, and S. Basu, The Astrophysical Journal **555**, 990 (2001).

[57] R. S. Raghavan *et al.*, Phys. Rev. Lett. **80**, 635 (1998).

[58] C. Bemporad, G. Gratta, and P. Vogel, Rev. Mod. Phys. **74**, 297 (2002).

[59] S. E. Kopp, Physics reports **439**, 101 (2007).

[60] V. F. Hess, Physikalische Zeitschrift **13**, 1084 (1912).

[61] D. Pacini, arXiv preprint arXiv:1002.1810 (2010).

[62] R. A. Millikan, Scientific American **134**, 149 (1926).

[63] W. Bothe and W. Kolhörster, Zeitschrift für Physik **56**, 751 (1929).

[64] K. Greisen, Phys. Rev. Lett. **16**, 748 (1966).

[65] G. T. Zatsepin and V. A. Kuz'min, Soviet Journal of Experimental and Theoretical Physics Letters **4**, 78 (1966).

[66] J. K. Becker, Physics Reports **458**, 173 (2008).

[67] J. van Santen, *Neutrino Interactions in IceCube above 1 TeV*, PhD thesis, 2014.

[68] IceCube Collaboration, R. Abbasi *et al.*, The Astrophysical Journal **740**, 16 (2011).

[69] R. Abbasi *et al.*, Phys. Rev. Lett. **100**, 101101 (2008).

[70] P. L. Biermann and G. Sigl, Introduction to cosmic rays, in *Physics and Astrophysics of Ultra-High-Energy Cosmic Rays*, pp. 1–26, Springer, 2001.

[71] M. Ackermann *et al.*, Science **339**, 807 (2013).

[72] F. Stecker, C. Done, M. Salamon, and P. Sommers, Phys. Rev. Lett. **66**, 2697 (1991).

[73] K. Mannheim, Astroparticle Physics **3**, 295 (1995).

[74] E. Waxman, Nuclear Physics B-Proceedings Supplements **118**, 353 (2003).

[75] E. Fermi, Phys. Rev. **75**, 1169 (1949).

[76] M. S. Longair, *High Energy Astrophysics*, Third ed. (Cambridge University Press, 2011).

[77] A. Bell, Monthly Notices of the Royal Astronomical Society **182**, 147 (1978).

[78] A. Hillas, Annual Review of Astronomy and Astrophysics **22**, 425 (1984).

[79] V. Beresinsky and G. Zatsepin, Berezinsky, VS & Zatsepin, GT, Yad. Fiz **11**, 200 (1970).

[80] K. Schatto, *Stacked searches for high-energy neutrinos from blazars with IceCube*, PhD thesis, 2014.

[81] E. Waxman, (2013), arXiv:1312.0558.

[82] E. Waxman and J. N. Bahcall, Phys. Rev. Lett. **78**, 2292 (1997), astro-ph/9701231.

[83] F. W. Stecker, Phys. Rev. **D72**, 107301 (2005), astro-ph/0510537.

[84] A. Loeb and E. Waxman, JCAP **0605**, 003 (2006), astro-ph/0601695.

[85] T. Kashti and E. Waxman, Phys. Rev. Lett. **95**, 181101 (2005).

[86] L. A. Anchordoqui, H. Goldberg, F. Halzen, and T. J. Weiler, Physics Letters B **593**, 42 (2004).

[87] P. Lipari, M. Lusignoli, and D. Meloni, Phys. Rev. D **75**, 123005 (2007).

[88] S. Hmmer, M. Maltoni, W. Winter, and C. Yaguna, Astroparticle Physics **34**, 205 (2010).

[89] M. Gonzalez-Garcia, M. Maltoni, J. Salvado, and T. Schwetz, Journal of High Energy Physics **2012**, 1 (2012).

[90] IceCube Collaboration, M. Aartsen *et al.*, (2015), 1502.03376.

[91] P. Mészáros and E. Waxman, Phys. Rev. Lett. **87**, 171102 (2001).

[92] S. Razzaque, P. Mészáros, and E. Waxman, Phys. Rev. Lett. **93**, 181101 (2004).

[93] S. Ando, J. Beacom, and H. Yüksel, Phys. Rev. Lett. **95**, 171101 (2005).

[94] J. F. Beacom, N. F. Bell, D. Hooper, S. Pakvasa, and T. J. Weiler, Phys. Rev. Lett. **90**, 181301 (2003).

[95] H. Athar, M. Jeżabek, and O. Yasuda, Phys. Rev. D **62**, 103007 (2000).

[96] J. F. Beacom *et al.*, Phys. Rev. Lett. **92**, 011101 (2004).

[97] D. Hooper, D. Morgan, and E. Winstanley, Phys. Rev. D **72**, 065009 (2005).

[98] G. D. Barr, T. K. Gaisser, P. Lipari, S. Robbins, and T. Stanev, Phys. Rev. D **70**, 023006 (2004).

[99] M. Honda, T. Kajita, K. Kasahara, and S. Midorikawa, Phys. Rev. D **70**, 043008 (2004).

[100] M. Honda, T. Kajita, K. Kasahara, S. Midorikawa, and T. Sanuki, Phys. Rev. D **75**, 043006 (2007).

[101] R. M. Barnett *et al.*, Phys. Rev. **54**, 1 (1996).

[102] G. Battistoni, A. Ferrari, T. Montaruli, and P. Sala, Astroparticle Physics **19**, 269 (2003).

[103] M. G. Aartsen *et al.*, Phys. Rev. Lett. **110**, 151105 (2013).

[104] R. Enberg, M. H. Reno, and I. Sarcevic, Phys. Rev. D **78**, 043005 (2008).

[105] R. Davis, D. S. Harmer, and K. C. Hoffman, Phys. Rev. Lett. **20**, 1205 (1968).

[106] W. Hampel *et al.*, Physics Letters B **447**, 127 (1999).

[107] A. I. Abazov *et al.*, Phys. Rev. Lett. **67**, 3332 (1991).

[108] K. S. Hirata *et al.*, Phys. Rev. Lett. **65**, 1297 (1990).

[109] Super-Kamiokande Collaboration, Y. Fukuda *et al.*, Phys. Rev. Lett. **81**, 1158 (1998).

[110] Q. R. Ahmad *et al.*, Phys. Rev. Lett. **87**, 071301 (2001).

[111] G. Bellini *et al.*, Phys. Rev. Lett. **108**, 051302 (2012).

[112] K. Hirata *et al.*, Phys. Rev. Lett. **58**, 1490 (1987).

[113] IMB, R. M. Bionta *et al.*, Phys. Rev. Lett. **58**, 1494 (1987).

[114] E. N. Alekseev, L. N. Alekseeva, V. I. Volchenko, and I. V. Krivosheina, JETP Lett. **45**, 589 (1987), [Pisma Zh. Eksp. Teor. Fiz. 45, 461-464 (1987)].

[115] A. E. Chudakov, Y. S. Elensky, and S. P. Mikheev, JETP Lett. **46**, 373 (1987), [Pisma Zh. Eksp. Teor. Fiz. 46, 297 (1987)].

[116] DUMAND Collaboration, `http://www.phys.hawaii.edu/~dumand/`.

[117] I. Belolaptikov *et al.*, Astroparticle Physics **7**, 263 (1997).

[118] M. Ageron *et al.*, Astroparticle Physics **31**, 277 (2009).

[119] J. Aguilar *et al.*, Physics Letters B **696**, 16 (2011).

[120] G. Riccobene *et al.*, Astroparticle Physics **27**, 1 (2007).

[121] NESTOR Collaboration, P. A. Rapidis, Nucl.Instrum.Meth. **A602**, 54 (2009).

[122] KM3NeT Collaboration, http://www.km3net.org/home.php.

[123] T. DeYoung *et al.*, Results from seven years of amanda-ii, in *Journal of Physics: Conference Series* Vol. 136, p. 022046, IOP Publishing, 2008.

[124] S. Yoshida and M. Teshima, Progress of theoretical physics **89**, 833 (1993).

[125] O. E. Kalashev, V. A. Kuzmin, D. V. Semikoz, and G. Sigl, Phys. Rev. D **66**, 063004 (2002).

[126] R. Engel, D. Seckel, and T. Stanev, Phys. Rev. D **64**, 093010 (2001).

[127] M. Ahlers, L. Anchordoqui, M. GonzalezGarcia, F. Halzen, and S. Sarkar, Astroparticle Physics **34**, 106 (2010).

[128] G. A. Askaryan, Sov. Phys. JETP **14** (1962).

[129] G. A. Askaryan, Sov. Phys. JETP **21** (1965).

[130] D. Saltzberg *et al.*, Phys. Rev. Lett. **86**, 2802 (2001).

[131] P. W. Gorham *et al.*, Phys. Rev. D **72**, 023002 (2005).

[132] P. W. Gorham *et al.*, Phys. Rev. Lett. **99**, 171101 (2007).

[133] P. W. Gorham *et al.*, Phys. Rev. Lett. **93**, 041101 (2004).

[134] I. Kravchenko *et al.*, Phys. Rev. D **73**, 082002 (2006).

[135] P. W. Gorham *et al.*, Phys. Rev. D **82**, 022004 (2010).

[136] AURA Collaboration, K. D. Hoffman, J.Phys.Conf.Ser. **81**, 012022 (2007).

[137] L. Gerhardt *et al.*, Nuclear Instruments and Methods in Physics Research Section A: Accelerators, Spectrometers, Detectors and Associated Equipment **624**, 85 (2010).

[138] Z. Cao, M. Huang, P. Sokolsky, and Y. Hu, J.Phys. **G31**, 571 (2005), astro-ph/0411677.

[139] J. Abraham *et al.*, Phys. Rev. D **79**, 102001 (2009).

[140] http://psec.uchicago.edu/links/Photomultiplier_Handbook.pdf.

[141] IceCube Collaboration, R. Abbasi *et al.*, Nuclear Instruments and Methods in Physics Research Section A: Accelerators, Spectrometers, Detectors and Associated Equipment **618**, 139 (2010).

[142] https://wiki.icecube.wisc.edu/index.php/Prepulse_Data.

[143] https://wiki.icecube.wisc.edu/index.php/Late_Pulse_Data.

[144] https://wiki.icecube.wisc.edu/index.php/Afterpulse_Data.

[145] A. Achterberg *et al.*, Astroparticle Physics **26**, 155 (2006).

[146] M. Aartsen *et al.*, Journal of Glaciology , 1117 (2013).

[147] M. Aartsen *et al.*, Nuclear Instruments and Methods in Physics Research Section A: Accelerators, Spectrometers, Detectors and Associated Equipment **711**, 73 (2013).

[148] G. Mie, Annalen der Physik **330**, 377 (1908).

[149] M. Ackermann *et al.*, Journal of Geophysical Research: Atmospheres **111**, n/a (2006).

[150] D. Chirkin *et al.*, Nuclear Instruments and Methods in Physics Research Section A: Accelerators, Spectrometers, Detectors and Associated Equipment **725**, 141 (2013).

[151] M. Aartsen *et al.*, arXiv preprint arXiv:1309.7010 (2013).

[152] R. Abbasi *et al.*, Nuclear Instruments and Methods in Physics Research Section A: Accelerators, Spectrometers, Detectors and Associated Equipment **601**, 294 (2009).

[153] C. H. Ha, *Observation of Atmosperhic Neutrino-induced Cascades in IceCube with DeepCore.*, PhD thesis, 2011.

[154] R. Gandhi, C. Quigg, M. H. Reno, and I. Sarcevic, Astroparticle Physics **5**, 81 (1996).

[155] R. Gandhi, C. Quigg, M. H. Reno, and I. Sarcevic, Phys. Rev. D **58**, 093009 (1998).

[156] S. L. Glashow, Physical Review **118**, 316 (1960).

[157] V. Bernhard, *Sensitivity of the IceCube Detector for Ultra-High Energy Electron-Neutrino Events.*, PhD thesis, 2008.

[158] J. Jackson, *Classical Electrodynamics* (John Wiley & Sons, 1999), .

[159] D. Chirkin and W. Rhode, arXiv preprint hep-ph/0407075 (2004).

[160] J.-H. Koehne *et al.*, Computer Physics Communications **184**, 2070 (2013).

[161] D. E. Groom, N. V. Mokhov, and S. I. Striganov, Atomic Data and Nuclear Data Tables **78**, 183 (2001).

[162] E. Middell, *Reconstruction of Cascade-like Events in IceCube*, Diplomarbeit, 2008.

[163] C. Wiebusch, *The Detection of faint light in deep underwater neutrino telescopes*, PhD thesis, 1995.

[164] M. Kowalski, *Search for neutrino-induced cascades with the AMANDA-II detector*, PhD thesis, 2004.

[165] M. D'Agostino, *First Evidence for Atmospheric Neutrino-Induced Cascades with the IceCube Detector*, PhD thesis, 2009.

[166] D. Heck, G. Schatz, T. Thouw, J. Knapp, and J. Capdevielle, (1998).

[167] D. Heck, Nachr.Forsch.zentr.Karlsruhe **33**, 113 (2001).

[168] R. S. Fletcher, T. K. Gaisser, P. Lipari, and T. Stanev, Phys. Rev. D **50**, 5710 (1994).

[169] A. Gazizov and M. Kowalski, Computer Physics Communications **172**, 203 (2005).

[170] H. Lai *et al.*, The European Physical Journal C-Particles and Fields **12**, 375 (2000).

[171] GENIE Collaboration, C. Andreopoulos, Acta Phys.Polon. **B40**, 2461 (2009).

[172] M. Larson, *Simulation and Identification of Non-Poissonian Noise Triggers in the IceCube Neutrino Detector.*, Master thesis, 2013.

[173] D. A. Chirkin, *Cosmic ray energy spectrum measurement with the Antarctic Muon and Neutrino Detector Array (AMANDA)*, PhD thesis, UNIVERSITY of CALIFORNIA at BERKELEY, 2003.

[174] M. D'Agostino, *Effective Livetimes in Weighted CORSIKA*, 2009, IceCube internal note.

[175] J. R. Hrandel, Astroparticle Physics **19**, 193 (2003).

[176] M. Aartsen *et al.*, Journal of Instrumentation **9**, P03009 (2014).

[177] J. Ahrens *et al.*, Nuclear Instruments and Methods in Physics Research Section A: Accelerators, Spectrometers, Detectors and Associated Equipment **524**, 169 (2004).

[178] D. Pandel, *Bestimmung von Wasser und Detektorparametern und Rekonstruktion von Myonen bis 100 TeV mit dem Baikal-Neutrinoteleskop NT-72*, Diploma thesis, 1996.

[179] J. Lundberg *et al.*, Nuclear Instruments and Methods in Physics Research Section A: Accelerators, Spectrometers, Detectors and Associated Equipment **581**, 619 (2007).

[180] N. Whitehorn, J. van Santen, and S. Lafebre, Computer Physics Communications **184**, 2214 (2013).

[181] IceCube Collaboration, M. Aartsen *et al.*, Science **342**, 1242856 (2013).

[182] R. Abbasi *et al.*, Phys. Rev. D **86**, 022005 (2012).

[183] E. Waxman and J. Bahcall, Phys. Rev. D **59**, 023002 (1998).

[184] P. B. Price and K. Woschnagg, Astroparticle Physics **15**, 97 (2001).

[185] IceCube Collaboration, A. Achterberg *et al.*, Acta Materialia **54**, 155 (2006).

[186] S. Jadach, Z. Was, R. Decker, and J. Kühn, Computer Physics Communications **76**, 361 (1993).

[187] T. K. Gaisser, Astroparticle Physics **35**, 801 (2012).

[188] G. C. Hill and K. Rawlins, Astroparticle physics **19**, 393 (2003).

[189] G. J. Feldman and R. D. Cousins, Phys. Rev. D **57**, 3873 (1998).

[190] IceCube Collaboration, M. Aartsen *et al.*, Phys. Rev. Lett. **111**, 021103 (2013), 1304.5356.

[191] IceCube Collaboration, M. Aartsen *et al.*, Phys. Rev. **D88**, 112008 (2013), 1310.5477.

[192] P. Abreu *et al.*, Advances in High Energy Physics **2013** (2013).

[193] P. Hallen, *On the Measurement of High-Energy Tau Neutrinos with IceCube*, Master thesis, 2013.

[194] A. Cooper-Sarkar and S. Sarkar, JHEP **2008**, 075 (2008).

[195] A. Cooper-Sarkar, P. Mertsch, and S. Sarkar, JHEP **1108**, 042 (2011), 1106.3723.

[196] IceCube Collaboration, M. Aartsen *et al.*, (2014), 1412.5106.

Appendix A

Examples of Simulated Double Pulse Events

A.1 NuTau CC

Fig. A.1 shows a 2.4 PeV ν_τ undergoing CC interaction in IceCube. The CC interaction vertex energy deposition is 0.5 PeV and the τ lepton energy is 1.8 PeV with a length of 40 m. The τ decays into hadrons shortly depositing equivalent energy of 1.7 PeV.

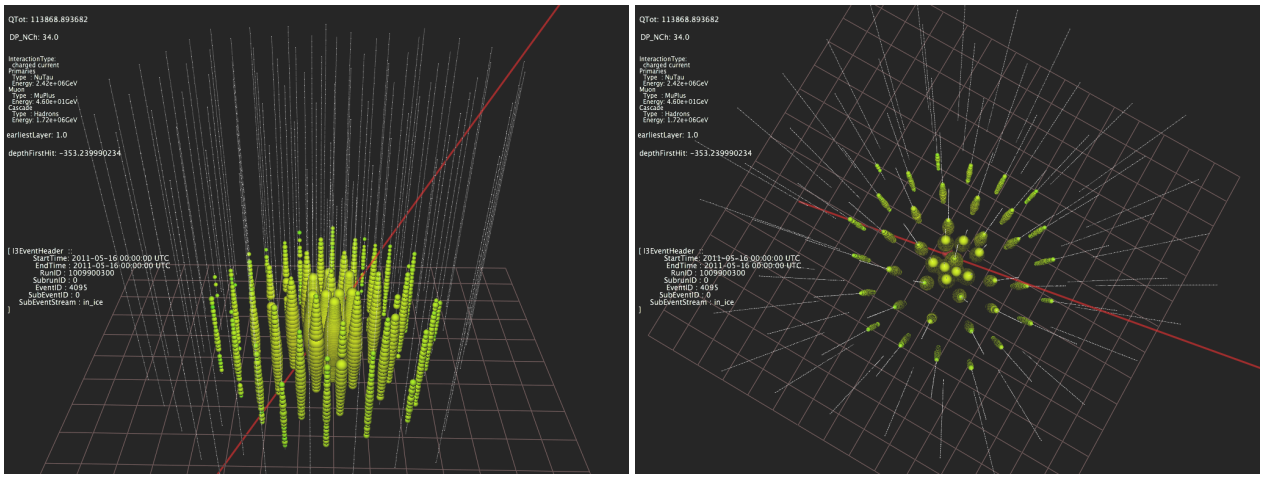

Figure A.1: An example of a simulated NuTau CC Double Pulse Event. Left: horizontal view. Right: Topdown view.

A total of 34 double pulse waveforms were identified for this event, with one double pulse waveform on one hit DOM. Among these 34 waveforms, 2 are on String 36 (IceCube central string) with adjacent DOMs 53 and 54; 1 on String 79 DOM 44; 12 on String 81 with adjacent

DOMs running from 30 to 41; 6 on String 85 with DOMs 37, 39, 41, 42, 43, and 44; and 13 on String 86 with adjacent DOMs running from 29 to 41. These kinds of events are ideal events for this analysis as they look entirely cascade-like visually, yet the ν_τ CC interaction chain leaves strong double pulse signature in multiple adjacent waveforms.

A.2 NuMu CC

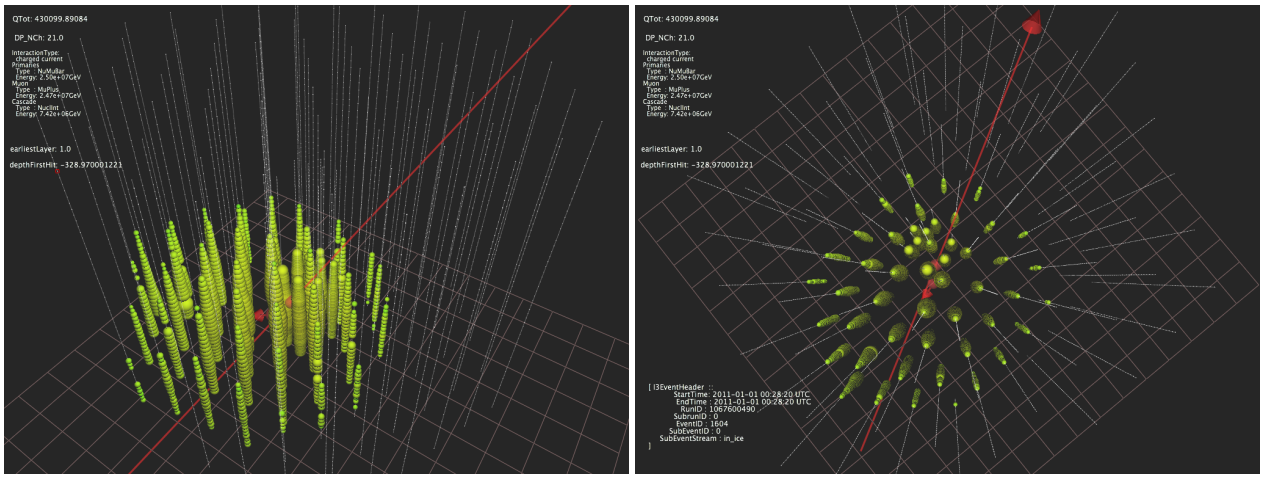

Figure A.2: An example of a simulated ν_μ CC Double Pulse Event. Left: horizontal view. Right: Topdown view.

Fig. A.2 shows a 25.0 PeV $\bar{\nu}_\mu$ CC event at final cut level. The outgoing μ has an energy of 24.7 PeV, and undergoes a stochastic energy loss of 7.4 PeV very close to the CC interaction vertex. The hadronic cascade from the CC interaction and the almost immediate stochastic energy loss provide a good chance for double pulse waveforms in the nearby DOMs. A total of 21 double pulse waveforms were identified in this event: 15 from String 82 with adjacent DOMs from 28 to 42; 4 on String 46 DOMs 46, 47, 51 and 53; and 2 on String 48 DOMs 52 and 53. This kind of event can not be resolved from the ν_τ CC event aforementioned. However, comparing the event rates integrating over all energies, the chance for this type of event to occur is about 3 times lower than the ν_τ CC event.

A.3 CORSIKA

A total of 6 raw CORSIKA events with double pulse waveforms survived before the final containment cut. Four of them are from the IC86 configuration and 2 from the IC79 configuration.

A.3.1 IC86

All 4 IC86 raw CORSIKA corner-clippers have only one double pulse waveform associated with them.

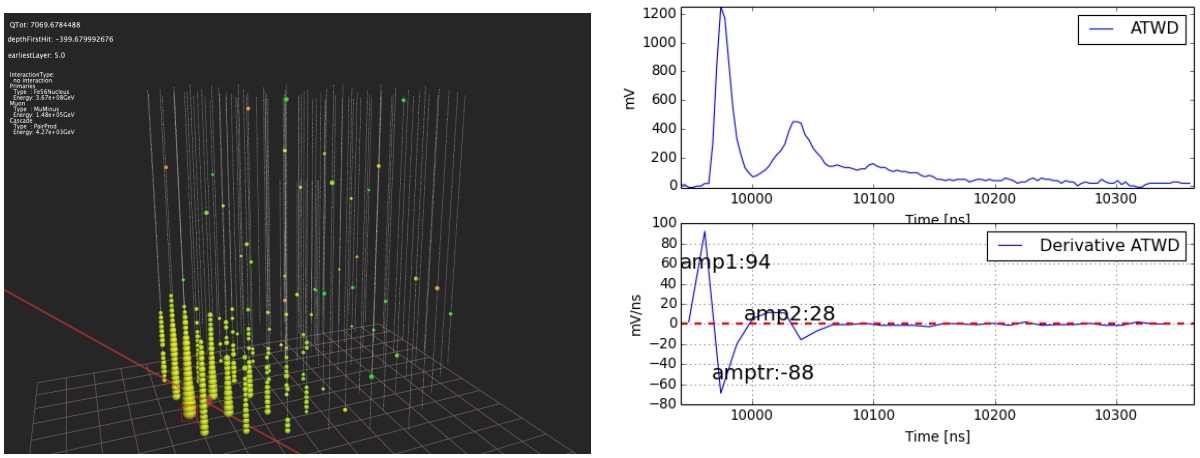

Figure A.3: Left: Display of IC86 CORSIKA double pulse event 1. Right: double pulse waveform from this event on OM(76, 60).

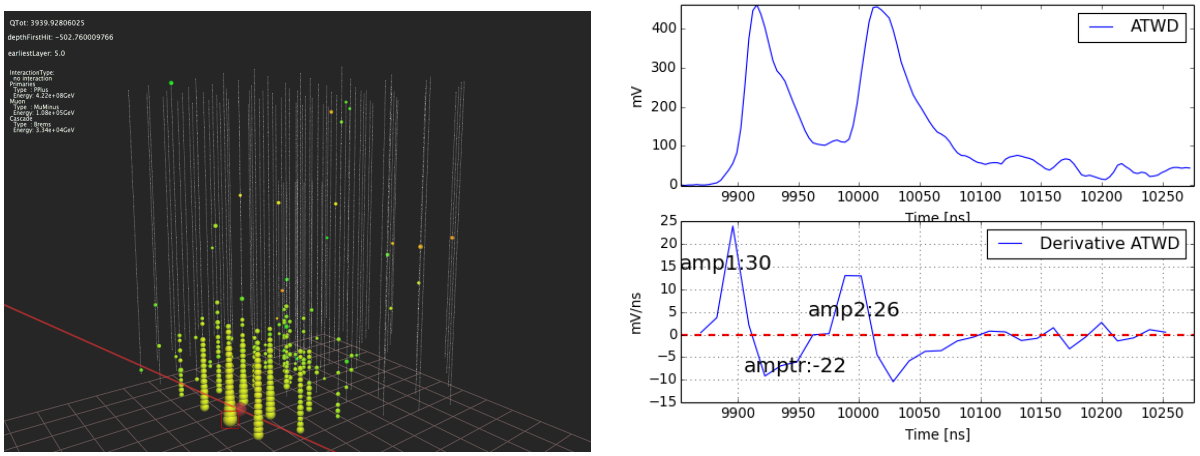

Figure A.4: Left: Display of IC86 CORSIKA double pulse event 2. Right: double pulse waveform from this event on OM(5, 60)

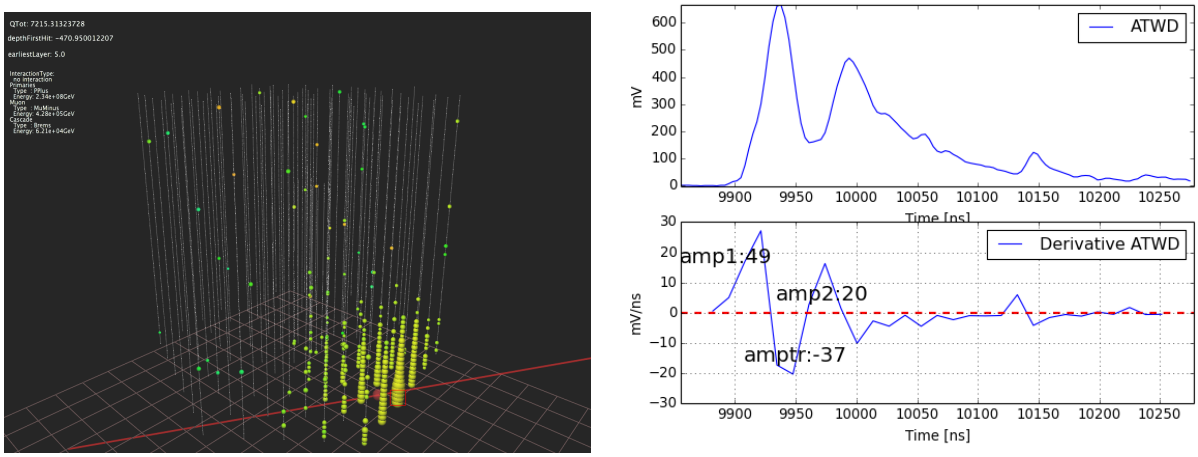

Figure A.5: Left: Display of IC86 CORSIKA double pulse event 3. Right: double pulse waveform from this event on OM(3, 59).

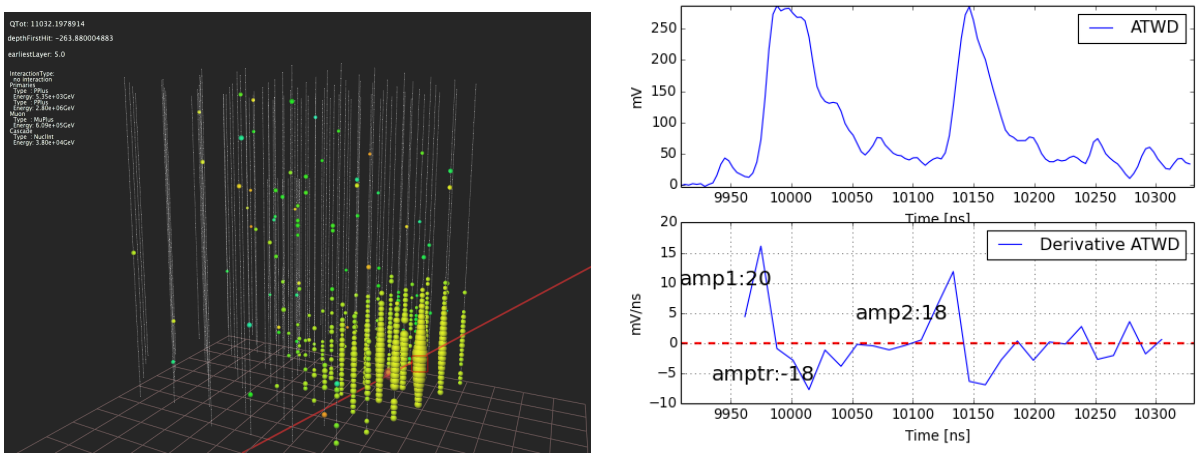

Figure A.6: Left: Display of IC86 CORSIKA double pulse event 4. Right: double pulse waveform from this event on OM(51, 52).

A.3.2 IC79

Two raw CORSIKA double pulse events from atmospheric muon simulation with IC79 configuration survived before final containment cut. One event has only one double pulse waveform, while the other has two.

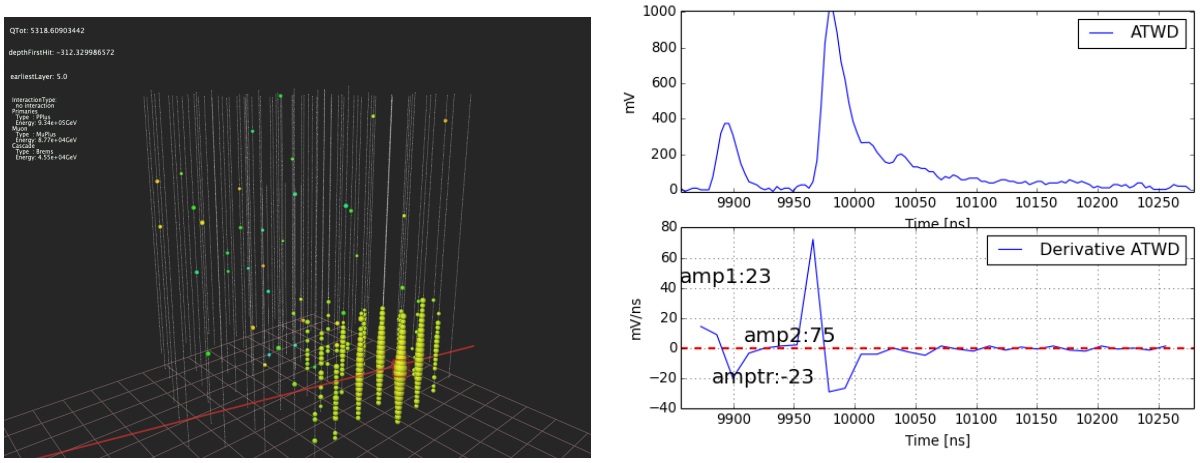

Figure A.7: Left: Display of IC79 CORSIKA double pulse event 1. Right: double pulse waveform from this event on OM(78, 49).

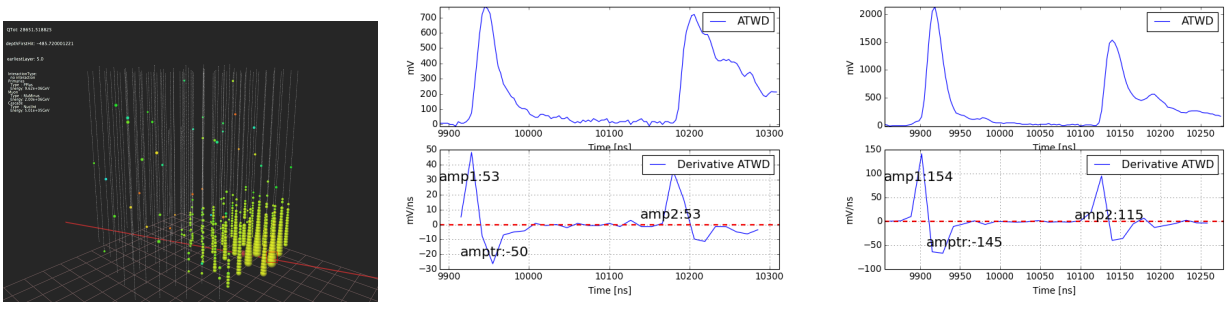

Figure A.8: Left: Display of IC79 CORSIKA double pulse event 2. Middle: double pulse waveform from this event on OM(77, 58). Right: double pulse waveform from this event on OM(77, 59).

Appendix B

Physical Cause of Double Pulse Waveforms from Atmospheric Muons

We see substantial double pulse waveforms from atmospheric muon events. We hypothesized that the first pulse is caused by Cherenkov light from the muon and its resulting cascades, and the second pulse is caused by stochastic energy loss such as bremsstrahlung and pair production.

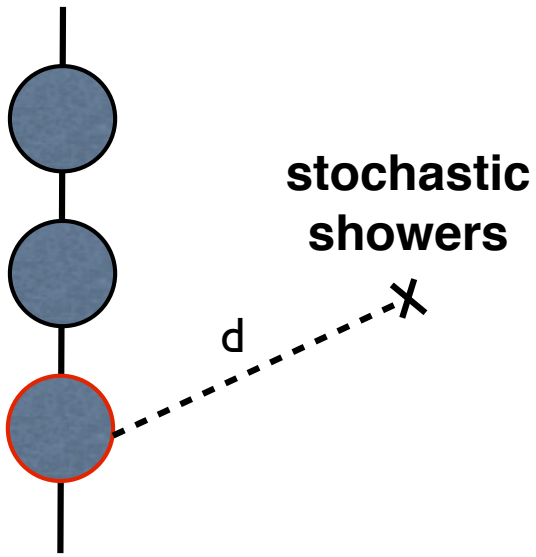

Figure B.1: Sketch of a stochastic shower occurring at distance d from a DOM which is indicated by the red circle.

This hypothesis can be tested on an event by event basis using the CORSIKA simulation in IceCube, which records the information of every air shower in an object named "MCTree". In every MCTree, the recorded information from the primary nucleus and its subsequent daughter particles includes the three position coordinates, the two directional coordinates, time, energy and track length. Figure B.2 demonstrates what is stored in a CORSIKA MCTree.

For a stochastic shower that occurs at distance d from a DOM (as demonstrated in Figure B.1), the expected energy seen by the DOM, called "arrival energy ", can be modeled in a simplified fashion (ignoring effects from propagation through ice)

$$E_{\text{arrival}} \propto \frac{E_{\text{stochastic}}}{4\pi d^2} \cdot e^{-d/l_\lambda} \tag{B.1}$$

where l_λ = 50 meters is an approximation of the average ice interaction length, which is the typical distance a photon being scattered or absorbed. The time it takes for the stochastic shower to propagate a distance d to arrive at the DOM is called "arrival time":

$$t_{\text{arrival}} \simeq t_{\text{stochastic}} + \frac{d}{v_{\text{ice}}} \tag{B.2}$$

where v_{ice}=0.22 nm/s is the phase velocity of light in ice.

```
*** TREE DUMP - BEGIN***
2559168 PPlus (-2322.85m ,904.168m ,1949.51m) (41.001deg ,156.509deg) -296.944ns 2.80425e+06GeV -1m
  2559166 PiMinus (nanm ,nanm ,nanm) (nandeg ,nandeg) nanns nanGeV nanm
    2559169 MuMinus (-2335.16m ,919.616m ,1949.51m) (40.9611deg ,156.57deg) -334.372ns 687.6GeV 2377.07m
    2559170 MuMinus (-2325.1m ,907.345m ,1949.51m) (40.9651deg ,156.511deg) -303.098ns 909.064GeV 2852.72m
      2559199 DeltaE (-723.537m ,211.331m ,-61.8121m) (40.9651deg ,156.511deg) 8581.83ns 2.43749GeV 0m
      2559200 DeltaE (-721.36m ,210.385m ,-64.5458m) (40.9651deg ,156.511deg) 8593.91ns 1.09849GeV 0m
      2559201 DeltaE (-700.82m ,201.458m ,-90.3412m) (40.9651deg ,156.511deg) 8707.86ns 0.684436GeV 0m
      2559202 EMinus (-609.835m ,161.917m ,-204.605m) (40.9651deg ,156.511deg) 10049.4ns 0.0511527GeV 0m
    2559171 MuMinus (-2309.7m ,911.493m ,1949.52m) (41.011deg ,156.552deg) -276.606ns 717.927GeV 2322.18m
    2559172 MuMinus (-2322.88m ,906.727m ,1949.51m) (41.0048deg ,156.541deg) -299.162ns 508.952GeV 1791.83m
    2559174 MuPlus (-2327.23m ,902.265m ,1949.51m) (40.9816deg ,156.471deg) -303.911ns 2084.89GeV 4053.05m
      2559206 PairProd (-729.048m ,206.393m ,-57.0081m) (40.9816deg ,156.471deg) 8561.92ns 1.40246GeV 0m
      2559207 DeltaE (-717.922m ,201.548m ,-70.9772m) (40.9816deg ,156.471deg) 8623.64ns 0.758196GeV 0m
      2559208 DeltaE (-716.92m ,201.112m ,-72.2353m) (40.9816deg ,156.471deg) 8629.2ns 1.07312GeV 0m
      2559209 PairProd (-676.035m ,183.31m ,-123.567m) (40.9816deg ,156.471deg) 8856.01ns 0.83256GeV 0m
      2559210 PairProd (-647.923m ,171.069m ,-158.861m) (40.9816deg ,156.471deg) 9011.96ns 0.829498GeV 0m
```

Figure B.2: Example of a partial CORSIKA MCTree. A full MCTree for a bright muon at the hundred TeV scale usually contains tens of thousands of lines. The x, y, z position in IceCube coordinates, zenith and azimuth, time, energy and track length are shown.

Figure B.3 to Figure B.6 demonstrate the arrival energy versus the arrival time for all stochastic showers to the double pulse DOMs corresponding to the 4 IC86 CORSIKA double pulse events summarized in Section A.3.1. For each of the DP DOMs, the arrival energy versus arrival time plot is compared to the recopulses[1] from that DOM as a function of pulse time. For all 4 events, the second pulse in the double pulse waveforms are coincident with their corresponding arrival energy from the stochastic showers. For the first pulse, Figures B.3, B.5 and B.6 show clear coincident arrival energy from stochastic showers, which indicate at least some part of the first pulse in the double pulse waveforms is from stochastic energy loss. For the case demonstrated in Figure B.4, the major contribution to the first pulse in the double pulse waveforms should be from direct Cherenkov photons from the muon as arrival energy from stochastic showers is very small. Therefore, the cause for double pulse feature from bright muons in the IceCube waveforms is that, the first pulse is from a combination of direct Cherenkov photons and stochastic showers and the second pulse is always from stochastic showers.

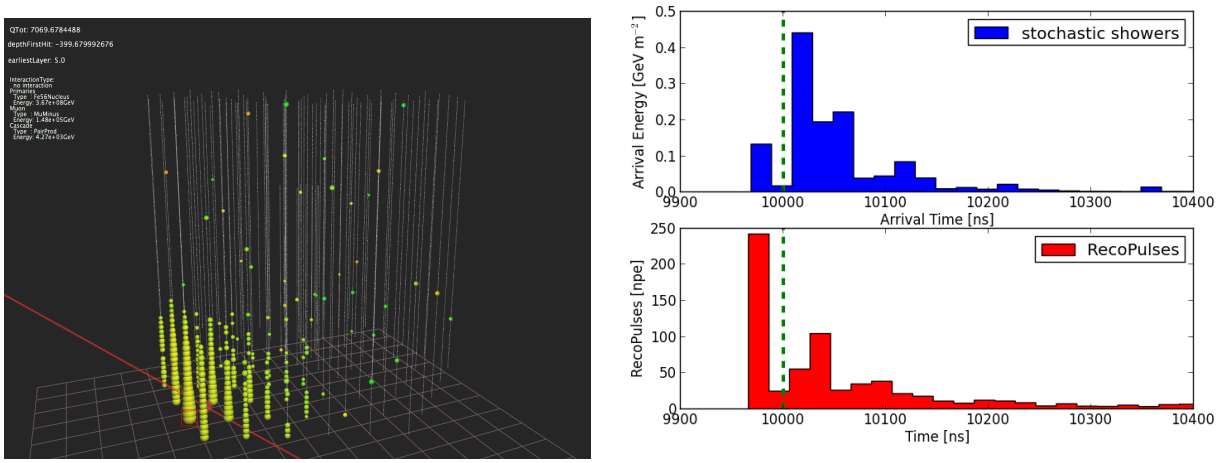

Figure B.3: Left: Display of IC86 CORSIKA double pulse event 1. Right: the arrival energy from all the stochastic showers versus their corresponding arrival times with respect to the DP DOM, in comparison to the recopulses versus pulse time from the DP DOM. The dotted lines are plotted at the same time to show the alignment between the stochastic showers in arrival time and recopulses in pulse time, which indicates the causal connection between them.

[1]The "recopulses" from a DOM are pulses extracted from that DOM's raw waveforms, so the recopulses versus pulse time is a direct representation of the raw waveform from that DOM.

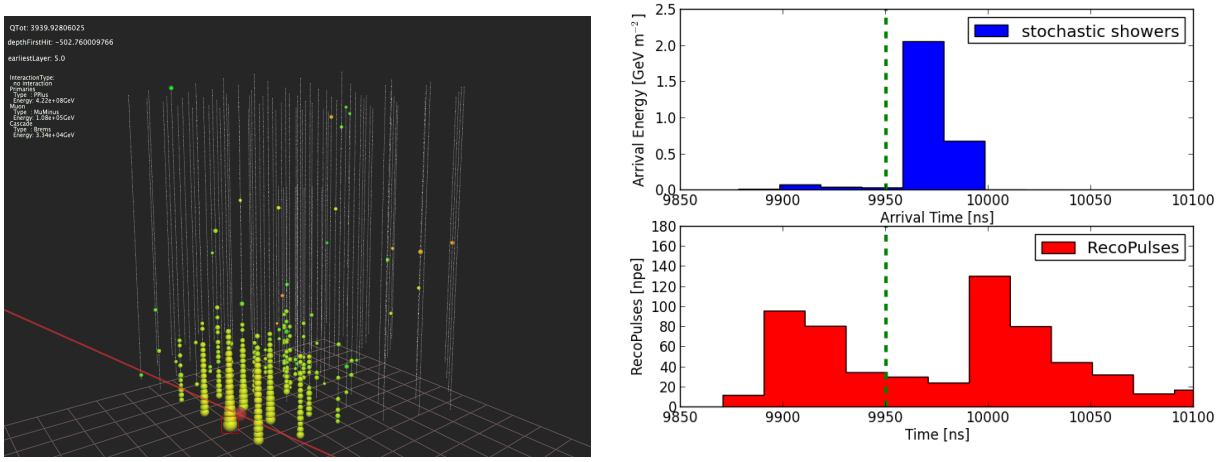

Figure B.4: Left: Display of IC86 CORSIKA double pulse event 2. Right: the arrival energy from all the stochastic showers versus their corresponding arrival times with respect to the DP DOM, in comparison to the recopulses versus pulse time from the DP DOM. The dotted lines are plotted at the same time to show the alignment between the stochastic showers in arrival time and recopulses in pulse time, which indicates the causal connection between them.

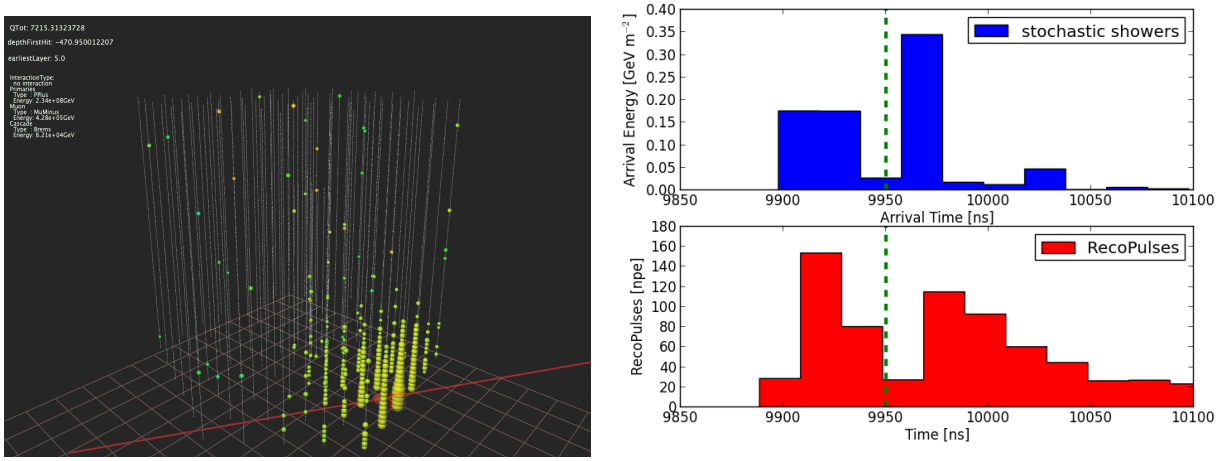

Figure B.5: Left: Display of IC86 CORSIKA double pulse event 3. Right: the arrival energy from all the stochastic showers versus their corresponding arrival times with respect to the DP DOM, in comparison to the recopulses versus pulse time from the DP DOM. The dotted lines are plotted at the same time to show the alignment between the stochastic showers in arrival time and recopulses in pulse time, which indicates the causal connection between them.

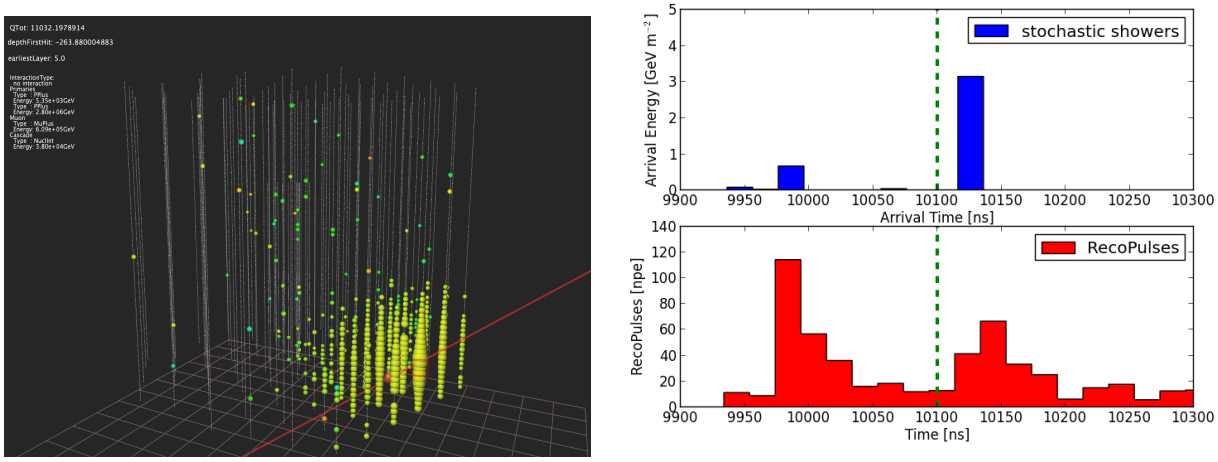

Figure B.6: Left: Display of IC86 CORSIKA double pulse event 4. Right: the arrival energy from all the stochastic showers versus their corresponding arrival times with respect to the DP DOM, in comparison to the recopulses versus pulse time from the DP DOM. The dotted lines are plotted at the same time to show the alignment between the stochastic showers in arrival time and recopulses in pulse time, which indicates the causal connection between them.